NUREG/CR-4667, Vol. 30
ANL-01/08

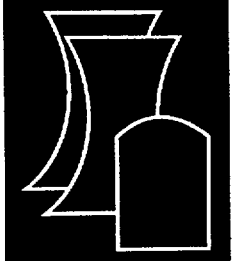

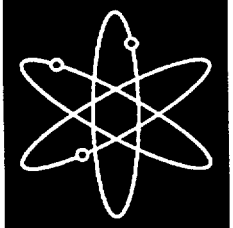

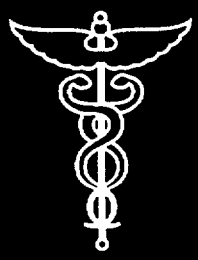

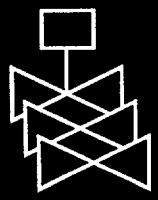

Environmentally Assisted Cracking in Light Water Reactors

Semiannual Report
January 2000—June 2000

Argonne National Laboratory

U.S. Nuclear Regulatory Commission
Office of Nuclear Regulatory Research
Washington, DC 20555-0001

AVAILABILITY OF REFERENCE MATERIALS IN NRC PUBLICATIONS

NRC Reference Material

As of November 1999, you may electronically access NUREG-series publications and other NRC records at NRC's Public Electronic Reading Room at www.nrc.gov/NRC/ADAMS/index.html.
Publicly released records include, to name a few, NUREG-series publications; *Federal Register* notices; applicant, licensee, and vendor documents and correspondence; NRC correspondence and internal memoranda; bulletins and information notices; inspection and investigative reports; licensee event reports; and Commission papers and their attachments.

NRC publications in the NUREG series, NRC regulations, and *Title 10, Energy*, in the Code of *Federal Regulations* may also be purchased from one of these two sources.

1. The Superintendent of Documents
   U.S. Government Printing Office
   Mail Stop SSOP
   Washington, DC 20402–0001
   Internet: bookstore.gpo.gov
   Telephone: 202-512-1800
   Fax: 202-512-2250
2. The National Technical Information Service
   Springfield, VA 22161–0002
   www.ntis.gov
   1–800–553–6847 or, locally, 703–605–6000

A single copy of each NRC draft report for comment is available free, to the extent of supply, upon written request as follows:

Address: Office of the Chief Information Officer,
Reproduction and Distribution
Services Section
U.S. Nuclear Regulatory Commission
Washington, DC 20555-0001
E-mail: DISTRIBUTION@nrc.gov
Facsimile: 301–415–2289

Some publications in the NUREG series that are posted at NRC's Web site address www.nrc.gov/NRC/NUREGS/indexnum.html are updated periodically and may differ from the last printed version. Although references to material found on a Web site bear the date the material was accessed, the material available on the date cited may subsequently be removed from the site.

Non-NRC Reference Material

Documents available from public and special technical libraries include all open literature items, such as books, journal articles, and transactions, *Federal Register* notices, Federal and State legislation, and congressional reports. Such documents as theses, dissertations, foreign reports and translations, and non-NRC conference proceedings may be purchased from their sponsoring organization.

Copies of industry codes and standards used in a substantive manner in the NRC regulatory process are maintained at—

The NRC Technical Library
Two White Flint North
11545 Rockville Pike
Rockville, MD 20852–2738

These standards are available in the library for reference use by the public. Codes and standards are usually copyrighted and may be purchased from the originating organization or, if they are American National Standards, from—

American National Standards Institute
11 West 42nd Street
New York, NY 10036–8002
www.ansi.org
212–642–4900

Legally binding regulatory requirements are stated only in laws; NRC regulations; licenses, including technical specifications; or orders, not in NUREG-series publications. The views expressed in contractor-prepared publications in this series are not necessarily those of the NRC.

The NUREG series comprises (1) technical and administrative reports and books prepared by the staff (NUREG–XXXX) or agency contractors (NUREG/CR–XXXX), (2) proceedings of conferences (NUREG/CP–XXXX), (3) reports resulting from international agreements (NUREG/IA–XXXX), (4) brochures (NUREG/BR–XXXX), and (5) compilations of legal decisions and orders of the Commission and Atomic and Safety Licensing Boards and of Directors' decisions under Section 2.206 of NRC's regulations (NUREG–0750).

DISCLAIMER: This report was prepared as an account of work sponsored by an agency of the U.S. Government. Neither the U.S. Government nor any agency thereof, nor any employee, makes any warranty, expressed or implied, or assumes any legal liability or responsibility for any third party's use, or the results of such use, of any information, apparatus, product, or process disclosed in this publication, or represents that its use by such third party would not infringe privately owned rights.

NUREG/CR-4667, Vol. 30
ANL-01/08

Environmentally Assisted Cracking in Light Water Reactors

Semiannual Report
January 2000–June 2000

Manuscript Completed: May 2001
Date Published: June 2001

Prepared by
O.K. Chopra, H.M. Chung, E.E. Gruber, D.R. Perkins,
W.J. Shack, W.K. Soppet, R.V. Strain

Argonne National Laboratory
9700 South Cass Avenue
Argonne, IL 60439

M.B. McNeil, NRC Project Manager

Division of Engineering Technology
Office of Nuclear Regulatory Research
U.S. Nuclear Regulatory Commission
Washington, DC 20555-0001
NRC Job Code W6610

Previous Documents in Series

Environmentally Assisted Cracking in Light Water Reactors Semiannual Report
April—September 1985, NUREG/CR–4667 Vol. I, ANL–86–31 (June 1986).
October 1985—March 1986, NUREG/CR–4667 Vol. II, ANL–86–37 (September 1987).
April—September 1986, NUREG/CR–4667 Vol. III, ANL–87–37 (September 1987).
October 1986—March 1987, NUREG/CR–4667 Vol. IV, ANL–87–41 (December 1987).
April—September 1987, NUREG/CR–4667 Vol. V, ANL–88–32 (June 1988).
October 1987—March 1988, NUREG/CR–4667 Vol. 6, ANL–89/10 (August 1989).
April—September 1988, NUREG/CR–4667 Vol. 7, ANL–89/40 (March 1990).
October 1988—March 1989, NUREG/CR–4667 Vol. 8, ANL–90/4 (June 1990).
April—September 1989, NUREG/CR–4667 Vol. 9, ANL–90/48 (March 1991).
October 1989—March 1990, NUREG/CR–4667 Vol. 10, ANL–91/5 (March 1991).
April—September 1990, NUREG/CR–4667 Vol. 11, ANL–91/9 (May 1991).
October 1990—March 1991, NUREG/CR–4667 Vol. 12, ANL–91/24 (August 1991).
April—September 1991, NUREG/CR–4667 Vol. 13, ANL–92/6 (March 1992).
October 1991—March 1992, NUREG/CR–4667 Vol. 14, ANL–92/30 (August 1992).
April—September 1992, NUREG/CR–4667 Vol. 15, ANL–93/2 (June 1993).
October 1992—March 1993, NUREG/CR–4667 Vol. 16, ANL–93/27 (September 1993).
April—September 1993, NUREG/CR–4667 Vol. 17, ANL–94/26 (June 1994).
October 1993—March 1994, NUREG/CR–4667 Vol. 18, ANL–95/2 (March 1995).
April—September 1994, NUREG/CR–4667 Vol. 19, ANL–95/25 (September 1995).
October 1994—March 1995, NUREG/CR–4667 Vol. 20, ANL–95/41 (January 1996).
April—December 1995, NUREG/CR–4667 Vol. 21, ANL–96/1 (July 1996).
January 1996—June 1996, NUREG/CR–4667 Vol. 22, ANL–97/9 (June 1997).
July 1996—December 1996, NUREG/CR–4667 Vol. 23, ANL–97/10 (October 1997).
January 1997—June 1997, NUREG/CR–4667 Vol. 24, ANL–98/6 (April 1998).
July 1997—December 1997, NUREG/CR–4667 Vol. 25, ANL–98/18 (September 1998).
January 1998—June 1998, NUREG/CR–4667 Vol. 26, ANL–98/30 (December 1998).
July 1998—December 1998, NUREG/CR–4667 Vol. 27, ANL–99/11 (October 1999).
January 1999—June 1999, NUREG/CR–4667 Vol. 28, ANL–00/7 (July 2000).
July 1999—December 1999, NUREG/CR–4667 Vol. 29, ANL–00/23 (November 2000).

Environmentally Assisted Cracking in Light Water Reactors Semiannual Report January 2000–July 2000

by

O. K. Chopra, H. M. Chung, E. E. Gruber, D. R. Perkins,
W. J. Shack, W. K. Soppet, and R. V. Strain

Abstract

This report summarizes work performed by Argonne National Laboratory on fatigue and environmentally assisted cracking (EAC) in light water reactors (LWRs) from January 2000 to June 2000. Topics that have been investigated include (a) environmental effects on fatigue S–N behavior of primary pressure boundary materials, (b) irradiation–assisted stress corrosion cracking (IASCC) of austenitic stainless steels (SSs), and (c) EAC of Alloys 600 and 690. Fatigue crack growth data and fracture mechanics analysis have been used to examine the fatigue S-N behavior of carbon and low-alloy steels in air and LWR environments. Fatigue life is considered to be composed of the growth of microstructurally small cracks and mechanically small cracks. The influence of reactor environments on the mechanism of fatigue crack initiation is discussed. Data from slow-strain-rate tensile tests and posttest fractographic analyses on several model SS alloys irradiated to $\approx 0.9 \times 10^{21}$ n·cm^{-2} (E >1 MeV) in He at 289°C in the Halden reactor have been summarized. The results have been used to determine the influence of alloying and impurity elements on the susceptibility of these steels to IASCC. Field–cracked boiling water reactor core shroud welds have been analyzed by advanced metallographic techniques to provide a better understanding of the cracking mechanism, failure behavior, and microstructural characteristics of the material. The list of test specimens shipped to the Halden Reactor for Phase–II irradiation experiments is presented. Fatigue crack growth tests were conducted on 1/4–T compact tension specimens of cast SSs in high–purity water at 289°C to establish the test procedure and conditions that will be used for performing crack growth tests on irradiated materials. The resistance of Alloys 600 and 690 to EAC in simulated LWR environments has been evaluated. The existing crack growth data for these alloys under cyclic loads have been analyzed to establish the effects of alloy chemistry, cold work, and water chemistry. The experimental crack growth rates have been compared with growth rates that would be expected in air under the same mechanical loading conditions to obtain a qualitative understanding of the degree and range of conditions that are necessary for significant environmental enhancement of growth rates.

Contents

Figures

Tables

Executive Summary

The ASME Boiler and Pressure Vessel Code provides rules for the construction of nuclear power plant components. Figure I-9.0 of Appendix I to Section III of the Code specifies fatigue design curves for structural materials. Although the effects of light water reactor (LWR) coolant environments are not explicitly addressed by the design curves, test data suggest that the Code fatigue curves may not be adequate in coolant environments. Two methods have been proposed for incorporating the effects of LWR coolant environments into the ASME Code fatigue evaluations: (a) develop new design fatigue curves for LWR applications, and (b) use a fatigue life correction factor to account for environmental effects. Both methods of evaluating fatigue lives are based on the statistical models for estimating fatigue lives of carbon and low–alloy steels and austenitic stainless steels (SSs) in LWR environments. Although estimates of fatigue lives based on the two methods may differ because of differences between the ASME mean curves used to develop the current design curves and the best–fit curves to the existing data used to develop the environmentally adjusted curves, either of these methods provides an acceptable approach to account for environmental effects. The mechanisms of fatigue crack initiation in carbon and low–alloy steels and austenitic SSs in LWR environments are discussed.

Hot-cell tests were conducted to determine the susceptibility to irradiation-assisted stress corrosion cracking (IASCC) of model austenitic SSs that were irradiated in the Halden boiling heavy water reactor to simulate irradiation-induced degradation of boiling water reactor (BWR) core internal components. Slow-strain-rate tensile (SSRT) tests in simulated BWR-like water were conducted on 23 model austenitic SS alloys that were irradiated at 288°C in helium in the Halden reactor to a fluence of $\approx 0.9 \times 10^{21}$ n·cm^{-2} (E >1 MeV). Fractographic analysis by scanning electron microscopy was conducted to determine the susceptibility to IASCC as manifested by the degree of intergranular and transgranular fracture surface morphology. These results were compared with similar test results obtained for 16 alloys that were irradiated to a fluence of $\approx 0.3 \times 10^{21}$ n·cm^{-2} (E >1 MeV).

In unirradiated state and at the relatively low fluence level of $\approx 0.3 \times 10^{21}$ n cm^{-2}, commercial and laboratory heats of Types 304, 304L, and 348 SS that contain relatively high concentrations of sulfur (>0.009 wt.% sulfur, 15-18.50 wt.% chromium) exhibited significant susceptibility to transgranular stress corrosion cracking (TGSCC), whereas alloys that contain a relatively low concentration of sulfur (<0.004 wt.%) exhibited good resistance to TGSCC At $\approx 0.9 \times 10^{21}$ n cm^{-2}, commercial heats of Types 304 and 316 SSs that contain low concentrations of S, exhibited good resistance to TGSCC and intergranular stress corrosion cracking (IGSCC) and high levels of uniform and total elongation, whereas a commercial heat of Type 304 SS that contained a relatively high concentration of sulfur exhibited poor resistance to TGSCC and IGSCC and low levels of uniform and total elongation. These observations indicate that for commercial heats of Types 304 and 304L SS, a high concentration of sulfur (>0.009 wt.%) is significantly detrimental and that a sufficiently low concentration of sulfur is a necessary condition to ensure good resistance to IASCC.

At $\approx 0.9 \times 10^{21}$ n cm^{-2}, a laboratory alloy that contains a high concentration of chromium (≈21 wt.%) exhibited excellent resistance to TGSCC and IGSCC in spite of high sulfur content (≈0.028 wt.% sulfur), whereas heats with <17.5 wt.% chromium exhibited significant susceptibility to TGSCC and IGSCC. This finding indicates that chromium atoms in high

concentration and low ferrite content <3 volume % play a beneficial role in suppressing susceptibility to IASCC under BWR conditions.

A total of 28 compact-tension (CT) and 32 SSRT specimens were fabricated, quality assurance (QA)-inspected, cleaned, and shipped to the Halden reactor to initiate the Phase-II Irradiation Experiment. The primary objectives of the Phase II Irradiation Experiment are to determine stress corrosion and crack growth behavior of core shroud welds, effects of post-welding annealing at 500 and 600°C on crack growth behavior of core shroud welds, effects of grain-boundary optimization on IASCC behavior of Types 304, 304L, 316 SS and Alloy 690, and effects of oxygen, molybdenum, titanium, and delta ferrite.

The heat-affected zone (HAZ) of BWR core shroud welds are contaminated with significant amounts of calcium, oxygen, and fluorine. These low-solubility impurities tend to concentrate on or near the grain boundaries of HAZs in core shroud welds, during either welding, in-reactor service, or both. Unusual microcavity structures were observed in the HAZs of field-cracked Type 304 and 304L SS core shroud welds and unirradiated mockup welds fabricated by the shielded-metal-arc procedure. The microcavities are formed preferentially on or near grain boundaries of HAZs. It appears that segregation of welding-related impurities calcium, oxygen, and fluorine produces a significantly modified composition at or near grain boundaries in the HAZ of a BWR core shroud weld, leading to a condition that is susceptible to formation of microcavities and fluorine–catalyzed stress corrosion at or near grain boundaries under irradiation.

Fatigue crack growth tests have been conducted on 1/4–T CT specimens of two heats of cast SS in high–purity water at 289°C to establish the test procedure and conditions that will be used to perform crack growth tests on irradiated materials. Tests were performed in accordance with ASTM E647 "Standard Test Method for Measurement of Fatigue Crack Growth Rates." The crack growth rates (CGRs) from 1/4–T CT specimens show good agreement with the results obtained on 1–T CT specimens in ≈0.3 ppm DO water

The resistance of Alloys 600 and 690 to environmentally assisted cracking in simulated LWR coolant environments is being evaluated. Fatigue CGR tests are being conducted in air and LWR coolant environments on CT specimens of several heats of Alloys 600 and 690 in annealed and annealed–and–thermally–treated conditions. During the current reporting period, the existing fatigue crack growth data on Alloys 600 and 690 have been analyzed to establish the effects of temperature, load ratio, frequency, and stress intensity range ΔK on CGRs in LWR environments. The experimental CGRs in high–temperature, high–purity water are compared with CGRs that would be expected in air under the same mechanical loading conditions to obtain a qualitative understanding of the degree and range of conditions that are necessary for significant environmental enhancement of growth rates. The fatigue CGRs of Alloy 600 are enhanced in high–dissolved oxygen (DO) water; the environmental enhancement of growth rates does not appear to depend on either the carbon content or heat treatment of the material. Also, in high–DO water, the CGRs at 320°C are comparable to those at 289°C. In contrast to the behavior in high–DO water, environmental enhancement of CGRs of Alloy 600 in low–DO water seems to depend on material conditions such as yield strength and grain boundary coverage of carbides. Material with high yield strength and/or low grain boundary coverage by carbides exhibit enhanced CGRs. Correlations have been developed for estimating the enhancement of CGRs of Alloy 600 in LWR environments relative to the CGRs in air under the same loading conditions.

For Alloy 690, the data suggest some enhancement of CGRs in high–DO water, i.e., ≈300 ppb DO. Limited data indicate no environmental effects on CGRs in low–DO water, i.e., water with <10 ppb DO. However, the existing database for Alloy 690 is small, and additional tests are needed to verify these results.

Acknowledgments

The authors thank T. M. Galvin, R. W. Clark, and J. Tezak for their contributions to the experimental effort. This work is sponsored by the Office of Nuclear Regulatory Research, U.S. Nuclear Regulatory Commission, under Job Code W6610; Program Manager: Dr. M. B. McNeil; Task 1 Manager: Dr. J. Muscara.

1 Introduction

The U.S. Nuclear Regulatory Commission (NRC) and its predecessor, the U.S. Atomic Energy Commission, have conducted research programs that address the aging of reactor components. The results of the research have been used to evaluate and establish regulatory guidelines to ensure acceptable levels of reliability for light water reactor (LWR) components. The products of this program have been technical reports, methodologies for evaluating licensee submittals, and other inputs to the regulatory process. Results have led to the resolution of regulatory issues, as well as to the development, validation, and improvement of regulations and regulatory guides. The present research on the effects of simulated reactor coolant environments on cracking of reactor components was initiated to resolve the remaining critical technical issues related to cracking phenomena in light water reactor (LWR) components. Initially, this project addressed cracking of boiling water reactor (BWR) pipes. Subsequently, in response to requests from the NRC Division of Nuclear Reactor Regulation (NRR) for assistance in dealing with developing cracking problems in aging reactors, the focus shifted to other problems in environmentally assisted cracking (EAC) of LWR components.

The overall objective of this program is to provide data and physical models to be used by the NRC staff in assessing environmentally assisted degradation of primary pressure boundary components in LWRs. The research is divided into five tasks:

(a) *Environmental effects on fatigue, crack growth, and stress corrosion cracking*
Fatigue and EAC of piping, pressure vessels, and core components in LWRs are important concerns during plant operation and extended reactor lifetimes. The degradation processes in U.S. reactors include fatigue, intergranular stress corrosion cracking (IGSCC), and propagation of fatigue or stress corrosion cracks that initiate in weld-sensitized heat-affected zones (HAZs) of stainless steel (SS) components. Occurrences of mechanical–vibration– and thermal-fluctuation-induced fatigue failures in LWR plants have also been documented. The objective of this task is to improve fatigue design curves and assess the additivity of fatigue damage in piping and vessel steels under load histories that are typical of LWR components. Results of this work will be used to assess industry fatigue evaluations that are related to license renewal.

(b) *Component vulnerability to irradiation-assisted stress corrosion cracking*
Irradiation–assisted stress corrosion cracking (IASCC) of in–core components in both BWRs and pressurized water reactors (PWRs) is becoming a more common problem as reactors age. The general pattern of the observed failures indicates that as nuclear plants age and neutron fluence increases, many apparently nonsensitized austenitic materials become susceptible to intergranular failure by IASCC. Some of these failures have been reported for components that are subjected to relatively low or negligible stress levels, e.g., control–blade sheaths and handles and instrument dry tubes of BWRs. Although most failed components can be replaced, it would be very difficult or impractical to replace some safety–significant structural components, such as the BWR top guide, core plate, and shroud. The objective of this task is to provide data and models that are needed to assess industry analyses of the likelihood of degradation and failure of

core internal components that are due to IASCC, and to evaluate licensee submissions related to inspection and remediation.

(c) *Cracking of nickel alloy components of LWR primary systems*
Internal components of reactor vessels are made of nickel-based alloys, e.g., Alloys 600, X750, and 182, which are susceptible to IGSCC. The causes and mechanisms of this cracking are not adequately understood, and the uncertainty is increased when licensee submissions are evaluated for factors such as damage accumulation and inspection intervals. The objective of this task is to provide technical data on the effects of cracks in nickel–alloy components on the residual life, inspection, and repair of the component. The results will be used to support NRR staff assessments of industry crack–growth models, and potential detection and mitigation measures.

(d) *Analysis of postweld heat treatment processes and validation of flaw acceptance criteria*
The objective of this task is to evaluate the effect of postweld heat treatment on long–term resistance to environmental cracking by assessing sensitization and other microstructural changes. This evaluation will provide the NRC with insights for use in reviewing licensee submittals.

(e) *Assessment of industry crack-growth models*
This task has two objectives. The first is to independently evaluate industry models that are used to establish inspection intervals and repair criteria. The second is to analyze in more detail the flaw acceptance criteria.

2 Environmental Effects on Fatigue Strain-versus-Life (S–N) Behavior of Primary Pressure Boundary Materials (O. K. Chopra)

Experience with operating nuclear power plants worldwide reveals that many failures may be attributed to fatigue; examples include piping components, nozzles, valves, and pumps.[1–3] In most cases, these failures have been associated with thermal loading due to thermal stratification and striping, or mechanical loading due to vibratory loading. Significant thermal loadings due to flow stratification were not included in the original design basis analysis. The effect of these loadings may also have been aggravated by corrosion effects due to a high–temperature aqueous environment. Fatigue cracks have been observed in pressurizer surge lines in PWRs (NRC Bulletin No. 88–11), and in feedwater lines connected to nozzles of pressure vessels in BWRs and steam generators in PWRs (NRC IE Bulletin, 79–13; NRC Information Notice 93–20). The cracking has been attributed to corrosion fatigue[4,5] or strain–induced corrosion cracking (SICC).[6] Case histories and identification of conditions that lead to SICC of low–alloy steels (LASs) in LWR systems have been summarized by Hickling and Blind.[7] A review of significant occurrences of corrosion fatigue damage and failures in various nuclear power plant systems has been presented in an Electric Power Research Institute (EPRI) report.[8]

2.1 Introduction

The formation of surface cracks and their growth as shear and tensile cracks to an engineering size (i.e., 3 mm deep) constitute the fatigue life of a material, which is represented by stress– or strain amplitude–vs.–fatigue life (S–N) curves. These curves define, for a given stress or strain amplitude, the number of cycles needed to form an engineering–size crack.

Cyclic loadings on a structural component occur because of changes in mechanical and thermal loadings as the system passes from one load set (e.g., pressure, temperature, moment, and force loading) to any other load set. For each load set, an individual fatigue usage factor is determined by the ratio of the number of cycles anticipated during the lifetime of the component to the allowable cycles. Figures I–9.1 through I–9.6 of Appendix I to Section III of the ASME Boiler and Pressure Vessel Code specify fatigue design curves that define the allowable number of cycles as a function of applied–stress amplitude. The cumulative usage factor (CUF) is the sum of the individual usage factors, and the ASME Code Section III requires that the CUF at each location must not exceed 1.

The current ASME Code design fatigue curves are based on strain–controlled fatigue tests of small polished specimens in air at room temperature. The design fatigue curves have been obtained by first adjusting the best-fit curves to the experimental data for mean stress effects and then decreasing the adjusted curves by a factor of 2 on stress or 20 on cycles, whichever was more conservative, at each point on the curve. These factors were intended to account for the differences and uncertainties in relating fatigue lives of laboratory test specimens to those of actual reactor components. The factors of 2 and 20 are not safety margins but rather conversion factors that must be applied to the experimental data to obtain reasonable estimates of the lives of actual reactor components.

The effects of LWR coolant environments on fatigue resistance of a material are not explicitly addressed in the Code design fatigue curves. Existing fatigue S–N data illustrate

potentially significant effects of LWR coolant environments on the fatigue life of carbon steels (CSs), LASs,[9–13] and austenitic SSs.[13–16] The key parameters that influence fatigue life in LWR environments are temperature, dissolved oxygen (DO) level in the water, loading or strain rate, and strain (or stress) amplitude; for carbon and low-alloy steels, the sulfur content of the steel is also important. Under certain environmental and loading conditions, the environmental effects alone substantially exceed the factor of 20 on life that is used to account for the differences between specimen tests and component behavior.

The objective of this paper is to use crack growth data and fracture mechanics analysis to examine the fatigue S-N behavior of carbon and low-alloy steels in air and LWR environments. The influence of reactor environments on the mechanism of fatigue crack initiation is discussed. Fatigue life is considered to be composed of the growth of microstructurally small cracks (MSCs) and mechanically small cracks. The growth of the latter has been characterized in terms of the J-integral range ΔJ and crack growth rate (CGR) data in air and LWR environments. The growth of MSCs in air is expressed by a modified version of the relationship presented by Hobson[17] and by the slip dissolution/oxidation process[18] in water.

2.2 Mechanism of Fatigue Crack Initiation

The formation of surface cracks and their growth as shear (Stage I) and tensile (Stage II) cracks to an engineering size (3 mm deep) constitute the fatigue life of a material, which is represented by the fatigue S–N curves. The curves specify, for a given stress or strain amplitude, the number of cycles needed to form an engineering crack. During fatigue loading of smooth test specimens, surface cracks 10 μm or longer form quite early in life (i.e., <10% of life) at surface irregularities or discontinuities either already in existence or produced by slip bands, grain boundaries, second-phase particles, etc.[10,19–23] Consequently, fatigue life may be considered to be composed entirely of crack propagation.[24]

Growth of these surface cracks may be divided into two regimes; an initial period, which involves growth of MSCs that is very sensitive to microstructure and is characterized by decelerating crack growth (Region AB, Stage I, in Fig. 1), and a propagation period, that involves growth of mechanically small cracks that can be predicted by fracture mechanics methodology and is characterized by accelerating crack growth (Region BC, Stage II, in Fig. 1). Mechanically small cracks, which correspond to Stage II, or tensile, cracks are characterized by striated crack growth and a fracture surface normal to the maximum principal stress. Conventionally, Stage 1 has been defined as the initiation stage and is considered sensitive to stress or strain amplitude, and Stage II has been defined as the propagation stage and is less sensitive to strain amplitude. The characterization and understanding of both the crack initiation and crack propagation stage are important for accurate estimates of the fatigue lives of structural materials.

Reduction of fatigue life in high-temperature water has often been attributed to easier crack initiation, because surface micropits that are present in high-temperature water act as stress raisers and provide preferred sites for the formation of fatigue cracks.[25] However, experimental data do not support this argument; the fatigue lives of carbon and low-alloy steel specimens that have been preoxidized at 288°C in high-DO water and then tested in air and those of unoxidized specimens (Fig. 2) are identical.[10] If the presence of micropits was responsible for the reduction in life, specimens preexposed to high-DO water and tested in air

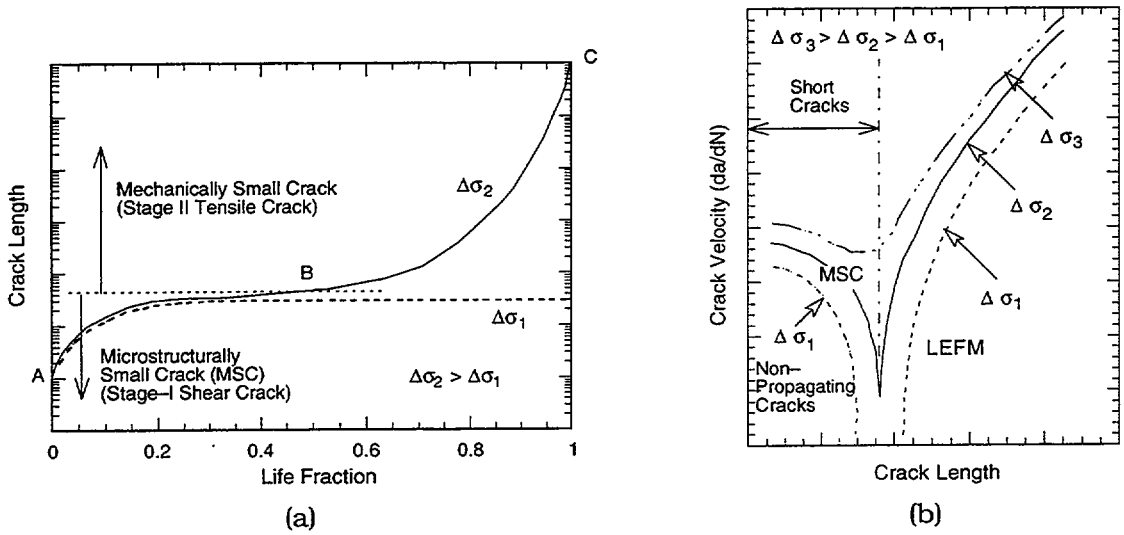

Figure 1. Schematic illustration of (a) growth of short cracks in smooth specimens as a function of fatigue life fraction and (b) crack velocity as a function of crack length

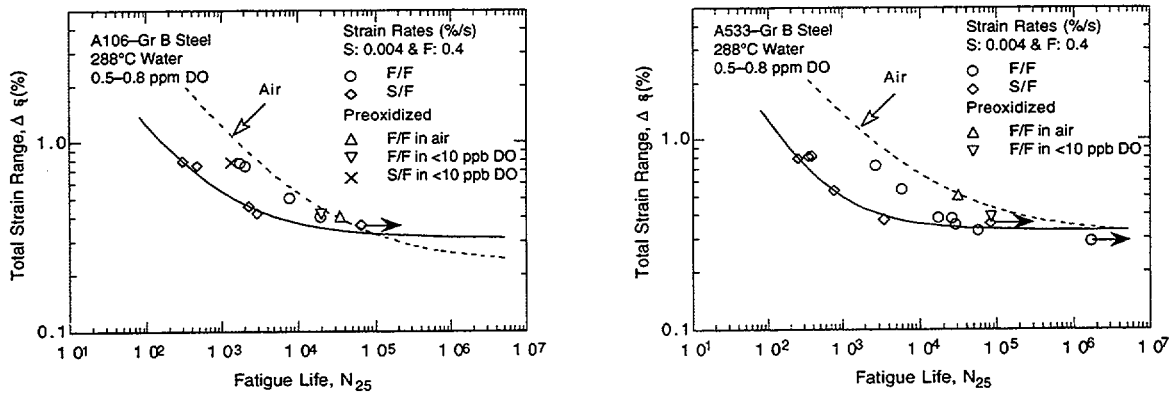

Figure 2. Effects of environment on formation of fatigue cracks in carbon and low–alloy steels. Preoxidized specimens were exposed at 288°C for 30–100 h in water with 06–0.8 ppm dissolved oxygen.

should show a decrease in life. Also, the fatigue limit of these steels should be lower in water than in air. Data obtained from specimens in high–DO water indicate that the fatigue limit is either the same as, or ≈20% higher in water than in air.[10,11]

Furthermore, if reduction in life is caused by easier formation of cracks, the specimens tested in high–DO water should show more cracks. Figure 3 shows plots of the number of cracks >10 μm long, along longitudinal sections of the gauge length of A106 Gr B and A533 Gr B specimens as a function of strain range in air, simulated PWR environment, and high–DO water at two strain rates. The results show that with the exception of the LAS tested in simulated PWR water, environment has no effect on the frequency (number per unit gauge length) of cracks. For similar loading conditions, the number of cracks in the test specimens in air and high–DO water is identical, although fatigue life is lower by a factor of ≈8 in water. Detailed metallographic evaluation of the fatigue test specimens indicates that the water environment has little or no effect on the formation of surface microcracks. Irrespective of

environment, cracks in carbon and low–alloy steels initiate along slip bands, carbide particles, or at the ferrite/pearlite phase boundaries.

The enhanced growth rates of long cracks in pressure vessel and piping steels in LWR environments have been attributed to either slip oxidation/dissolution[26] or hydrogen–induced cracking.[27] Both mechanisms depend on the rates of oxide rupture, passivation, and liquid diffusion. Therefore, it is often difficult to differentiate between the two processes or to establish their relative contributions to crack growth in LWR environments.

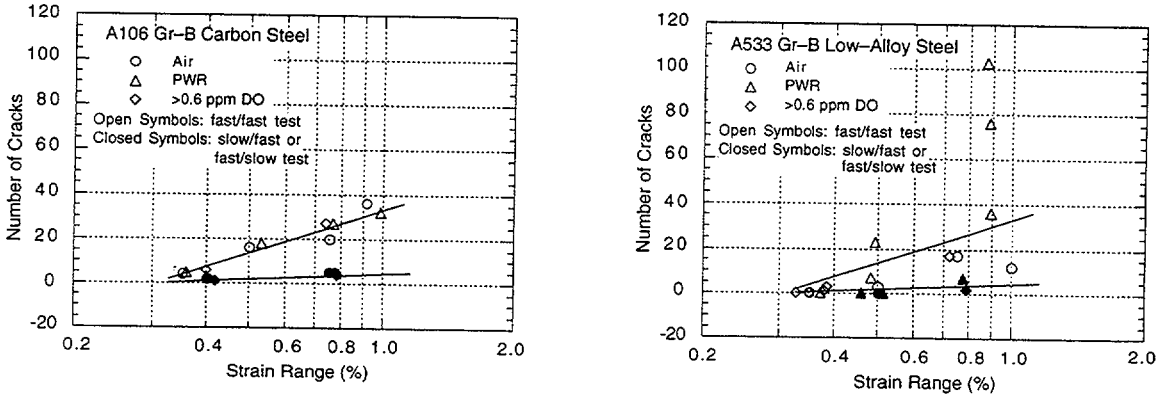

Figure 3. Number of >10–μm–long cracks along longitudinal section of fatigue specimens of (a) A106 Gr B carbon steel and (b) A533 Gr B low–alloy steel tested in LWR environments. Number of cracks represents average value along 7–mm gauge length.

Studies of crack initiation in smooth fatigue specimens[21] indicate that the decrease in fatigue life of CSs and LASs in LWR environments is caused primarily by the effects of environment on the growth of cracks <100 μm deep. When compared with CGRs in air, growth rates in high–DO water are nearly two orders of magnitude higher for cracks that are <100 μm deep and one order of magnitude higher for cracks that are >100 μm deep. Metallographic examination of test specimens indicates that in high–DO water, surface cracks <100 μm deep grow entirely as tensile cracks normal to the stress, whereas in air or simulated PWR environments, they are at an angle of 45° to the stress axis (Fig. 4).[21] Also, for CSs, cracks <100 μm deep propagate across both the soft ferrite and hard pearlite regions, whereas in air, they propagate only along soft ferrite regions. The crack morphology of the specimen surface also differs in air and water environments (Fig. 5); surface cracks in high–DO water are always straight and normal to the stress axis, whereas in air or simulated PWR environments, they are mostly at 45° to the stress axis. The differing crack morphology, absence of Stage I crack growth, and propagation of near–surface cracks across pearlite regions indicate that in high-DO water, growth of MSCs occurs predominantly by the slip oxidation/dissolution process.

In high–DO water, crack initiation in CSs and LASs may be explained as follows: surface MSCs form quite early in fatigue life. During cyclic loading, the protective oxide film is ruptured at strains greater than the fracture strain of surface oxides, and the MSCs grow by anodic dissolution of the freshly exposed surface to crack lengths greater than the critical length of MSCs. These now mechanically small cracks grow to engineering size, and their growth, which is characterized by accelerating rates, can be predicted by fracture mechanics methodology.

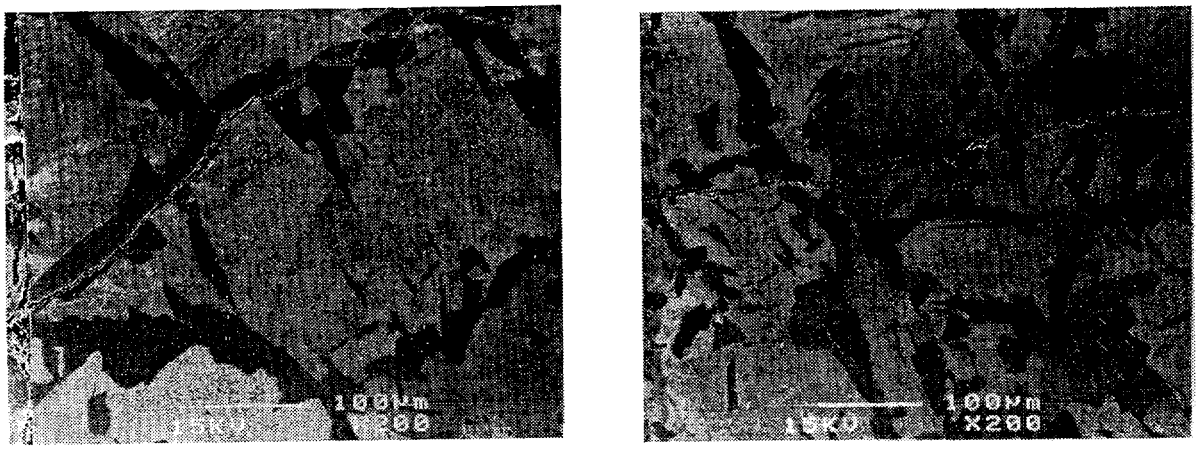

(a) (b)

Figure 4. Photomicrographs of fatigue cracks along gauge sections of A106 Gr. B carbon steel in (a) air and (b) high–DO water at 288°C

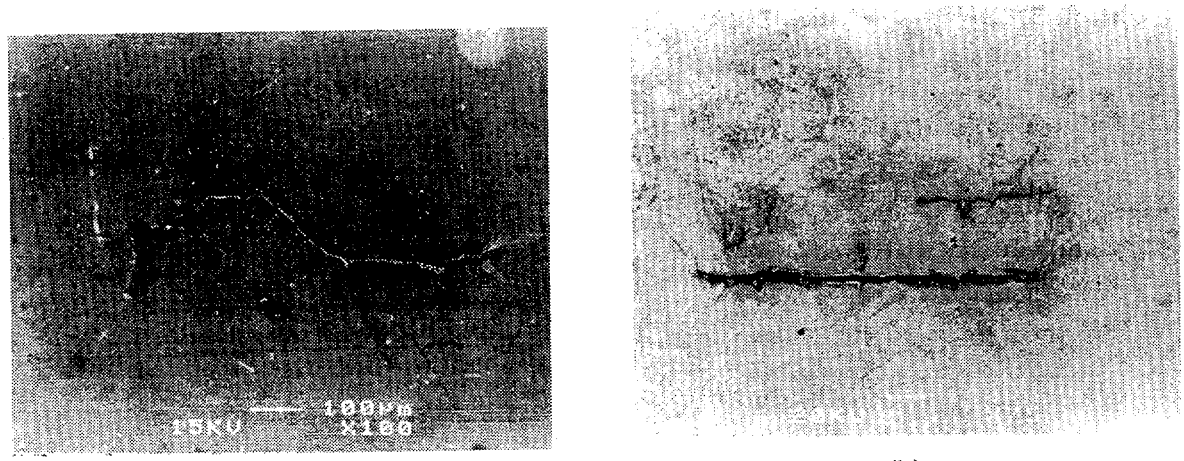

(a) (b)

Figure 5. Photomicrographs of fatigue cracks on gauge surfaces of A106 Gr. B low–alloy steel in (a) air and (b) high–DO water at 288°C

2.3 Fatigue S–N Data in LWR Environments

The fatigue lives of both carbon and low–alloy steels are decreased in LWR environments; the reduction in life depends on temperature, strain rate, dissolved oxygen (DO) level in water, and sulfur content of the steel.[9–13,28–30] Fatigue life is decreased significantly when four conditions are satisfied simultaneously, viz., strain amplitude, temperature, and DO in water are above a minimum level, and strain rate is below a threshold value. Although the microstructures and cyclic–hardening behavior of carbon and low–alloy steels differ significantly, environmental degradation of fatigue life of these steels is very similar. For both steels, only moderate decrease in life (by a factor of <2) is observed when any one of the threshold conditions is not satisfied, e.g., temperature <150°C, strain rate >1%/s, DO levels <0.05 ppm, or applied strain range is below a critical value. The effects of the critical parameters on fatigue life and their threshold values are summarized below.

(a) *Strain:* A minimum threshold strain is required for environmental effects to occur; limited data suggest that the threshold value is ≈20% higher than the fatigue limit for the steel.

(b) *Strain Rate*: Environmental effects occur primarily during the tensile–loading cycle, and at strain levels greater than the threshold value required to rupture the surface oxide film. When all other threshold conditions are satisfied, fatigue life decreases logarithmically with decreasing strain rate below 1%/s; the effect saturates at ≈0.001%/s.

(c) *Temperature*: When other threshold conditions are satisfied, fatigue life decreases linearly with temperature above 150°C and up to 320°C.

(d) *Dissolved Oxygen in Water*: When other threshold conditions are satisfied, fatigue life decreases logarithmically with DO above 0.05 ppm; the effect saturates at ≈0.5 ppm DO.

(e) *Sulfur Content of Steel*: The effect of sulfur content on fatigue life depends on the DO content of the water. When all threshold conditions are satisfied and DO level is between 0.05–0.2 ppm, fatigue life decreases with increasing sulfur content. Environmental effects saturate at an sulfur content of ≈0.015 wt.%. At high DO levels, e.g., >1.0 ppm, fatigue life seems to be insensitive to sulfur content in the range of 0.002–0.015 wt.%.[31]

(f) *Flow Rate*: It has long been recognized that the flow rate may have a strong effect on the fatigue life of materials because it may cause changes in the local environmental conditions at the crack tip. However, information about the effects of flow rate has been very limited. Recent results indicate that under the environmental conditions typical of operating BWRs, e.g., high–purity water at 289°C with ≈0.2 ppm DO, environmental effects on the fatigue life of carbon and low–alloy steels are a factor of ≈2 lower at high flow rates than those under semistagnant conditions or at very low flow rates. Data on A333–Gr. 6 CS indicate that at 289°C, relatively slow strain rate (0.01%/s), and under all DO conditions, a high flow rate has an appreciable effect on the fatigue lives of the steel.[32] In high–DO water (i.e., 0.2 ppm or higher) at 289°C, environmental effects on the fatigue life are a factor of ≈2 lower at a flow rate of 7 m/s than those at 0.3 m/s. The results also indicate that flow rate has little or no effect at high strain rates (0.4%/s). Similar effects have also been observed in another study at Kraftwerk Union (KWU) laboratories on A508 carbon steel pipe; environmental effects on fatigue life were a factor of ≈2 lower at a flow rate of 0.6 m/s than those at very low flow rate.[33]

Statistical models based on the existing fatigue S–N data have been developed for estimating the fatigue lives of pressure vessel and piping steels in air and LWR environments.[10,13] In air at room temperature, the fatigue life N of CSs is represented by

$$\ln(N) = 6.564 - 1.975 \ln(\varepsilon_a - 0.113) \quad (1)$$

and of LASs, by

$$\ln(N) = 6.627 - 1.808 \ln(\varepsilon_a - 0.151), \quad (2)$$

where ε_a is applied strain amplitude (%). In LWR environments, the fatigue life of CSs is represented by

$$\ln(N) = 6.010 - 1.975 \ln(\varepsilon_a - 0.113) + 0.101\, S^* T^* O^* \dot{\varepsilon}^* \quad (3)$$

and of LASs, by

$$\ln(N) = 5.729 - 1.808 \ln(\varepsilon_a - 0.151) + 0.101\, S^* T^* O^* \dot{\varepsilon}^*, \quad (4)$$

where S^*, T^*, O^*, and $\dot{\varepsilon}^*$ are transformed sulfur content, temperature, DO, and strain rate, respectively, defined as follows:

$$\begin{array}{ll} S^* = 0.015 & (DO > 1.0 \text{ ppm}) \\ S^* = S & (DO \le 1.0 \text{ ppm } \& \ 0 < S \le 0.015 \text{ wt.\%}) \\ S^* = 0.015 & (DO \le 1.0 \text{ ppm } \& \ S > 0.015 \text{ wt.\%}) \end{array} \quad (5)$$

$$\begin{array}{ll} T^* = 0 & (T < 150°C) \\ T^* = T - 150 & (T = 150\text{–}350°C) \end{array} \quad (6)$$

$$\begin{array}{ll} O^* = 0 & (DO < 0.05 \text{ ppm}) \\ O^* = \ln(DO/0.04) & (0.05 \text{ ppm} \le DO \le 0.5 \text{ ppm}) \\ O^* = \ln(12.5) & (DO > 0.5 \text{ ppm}) \end{array} \quad (7)$$

$$\begin{array}{ll} \dot{\varepsilon}^* = 0 & (\dot{\varepsilon} > 1\%/s) \\ \dot{\varepsilon}^* = \ln(\dot{\varepsilon}) & (0.001 \le \dot{\varepsilon} \le 1\%/s) \\ \dot{\varepsilon}^* = \ln(0.001) & (\dot{\varepsilon} < 0.001\%/s). \end{array} \quad (8)$$

The discontinuity in the value of O^* at 0.05 ppm DO is due to an approximation and does not represent a physical phenomenon.

2.4 Fracture Mechanics Approach to Estimation of Fatigue S–N Curves for Carbon and Low–Alloy Steels

The fatigue S–N behavior of carbon and low–alloy steels in air and LWR environments has been examined by using a fracture mechanics approach and crack growth data. The fatigue life is considered to be composed of the growth of MSCs and mechanically small cracks. Studies on crack initiation in smooth fatigue specimens indicate that surface cracks form quite early in life. Smith et al.[34] detected 10–μm deep surface cracks at temperatures up to 700°C in Waspalloy. Hussain et al.[35] examined the growth of ≈20–μm–deep surface cracks through four or more grains. Tokaji et al.[20,36–38] defined crack initiation as the formation of a 10–μm–deep crack. Gavenda et al.[21] reported that in room–temperature air, 10–μm–deep cracks form early during fatigue life, i.e., <10% of fatigue life. Suh et al.[39,40] reported that a crack is said to have initiated when any cracklike mark grows across a grain boundary, or when the separation of grain boundaries becomes clear. Based on these results, it is reasonable to assume the initial depth of MSCs to be ≈10 μm.

2.4.1 Transition from Microstructurally Small to Mechanically Small Crack

Various criteria may be used to define the crack length for transition from an MSC to a mechanically small crack. They may be related to the size of the plastic zone, crack length–vs.–fatigue life (a–N) curve, Weibull distribution of the cumulative probability of fracture, stress range–vs.–crack length curve, or grain size. The results indicate that the crack length

for transition from MSC to mechanically small crack depends on applied stress and microstructure of the material.

Plastic Zone: de los Rios et al.[41,42] and Lankford[43-45] defined the transition from small to large cracks as the crack length at which the size of the linear elastic fracture mechanics (LEFM) plastic zone exceeds the diameter of a grain.

Crack Length–vs.–Fatigue Life Curve: Obrtlik et al.[22] divided the fatigue crack length a–vs.–fatigue life N curves into two regimes: MSCs, in which the dependence of crack length on fatigue life can be represented by a straight line; and mechanically small cracks, in which fatigue crack growth is represented by an exponential function fit of the experimental data.

Weibull Distribution of the fatigue crack lengths: Suh et al.[39,40] examined fatigue specimens and showed that distribution of crack lengths could be described by a Weibull distribution. They used the knee in the distribution to define the transition from shear crack growth to tensile crack growth. The knee occurred in the range of 3–5 grain diameters.

Stress Range–vs.–Crack Length Curve: Kitagawa and Takahashi[46] and Taylor and Knott[47] used the stress range–vs.–crack length curve to discriminate an MSC from a mechanically small crack. For crack lengths >500 μm, plots of the threshold stress range for fatigue crack growth ($\Delta\sigma_{th}$) vs. crack length yield a straight line, i.e., the threshold stress intensity factor (ΔK_{th}) is constant. For crack lengths <500 μm, $\Delta\sigma_{th}$ deviates from the linear relationship and approaches a constant value as the crack length becomes smaller. The constant value of $\Delta\sigma_{th}$ is approximately equal to the fatigue limit of a smooth specimen of the material. The crack length at which the $\Delta\sigma_{th}$ vs. crack length curve changes from a linear relationship to a constant value is used to define the transition from MSC to mechanically small crack.

Grain Size: Tokaji et al.[20,36,37] estimated the transition crack length to be ≈8 times the microstructural unit size. Ravichandran[48] reported that large fluctuations in crack shape or aspect ratio occur at crack lengths of approximately a few grain diameters (typically five or fewer grain diameters). Hussain et al.[35] observed that fatigue CGRs decreased systematically at microstructural heterogeneities up to a length of three or four grain diameters. Dowling[49] reported that the J-integral correlation is not valid for surface crack lengths <10 crystallographic grain diameters.

The above studies indicate that the crack length for transition from MSC to mechanically small crack is a function of applied stress and microstructure of the material; actual value may range from 150 to 250 μm. A constant value of ≈200 μm was assumed for convenience, for both carbon and low–alloy steels; it is the initial size for mechanically small cracks.

2.4.2 Fatigue Crack Growth Rates

Air Environment

The growth rate da/dN (mm/cycle) of MSCs, i.e., from 10 to 200 μm, in air can be represented by the Hobson relationship[17,19,50,51]

$$da/dN = A_1 \ (\Delta\sigma)^{n_1} \ (d - a), \qquad (9)$$

where a is the length (mm) of the predominant crack, $\Delta\sigma$ is the stress range (MPa), constant A_1 and exponent n_1 are determined from existing fatigue S–N data, and d is the material constant related to grain size. The values of A_1 and n_1 for carbon and low-alloy steels at room temperature and reactor operating temperatures are given in Table 1. A value of 0.3 mm was used for the material constant d. Also, because growth rates increase significantly with decreasing crack length, a constant growth rate was assumed for crack lengths smaller than 0.075 mm. The applied stress range $\Delta\sigma$, which represents the value at fatigue half-life, is determined from Ramberg–Osgood relationships given by Eqs. A1–A5 of the Appendix.

Table 1 Values of the constants A_1 and n_1 in Equation 9

Steel Type	Temperature	A_1	n_1
Carbon	Room	3.33×10^{-41}	13.13
	Operating	9.54×10^{-34}	10.03
Low-Alloy	Room	1.45×10^{-36}	11.10
	Operating	1.07×10^{-43}	13.43

The growth rates of mechanically small cracks in air are estimated from Eq. A8 of the Appendix. A factor of 1.22 enhancement in growth rates was used at reactor operating temperatures.

LWR Environment

A model based on oxide film rupture and anodic dissolution (or slip dissolution/oxidation model) was proposed by Ford et al.[18] to incorporate the effects of LWR environments on fatigue lives of carbon and low-alloy steels. The model considers that a thermodynamically stable protective oxide film forms on the surface to ensure that a crack will propagate with a high aspect ratio without degrading into a blunt pit, and that a strain increment is required to rupture the oxide film, thereby exposing the underlying matrix to the environment. Once the passive oxide film is ruptured, crack extension is controlled by dissolution of freshly exposed surfaces and by oxidation characteristics. Ford and Andresen[52] proposed that the average crack growth rate da/dt (cm/s) is related to the crack tip strain rate $\dot{\varepsilon}_{ct}$ (s^{-1}) by the relationship

$$da/dt = A_2(\dot{\varepsilon}_{ct})^{n_2}, \tag{10}$$

where the constant A_2 and exponent n_2 depend on the material and environmental conditions at the crack tip. A lower limit of crack propagation rate is associated with blunting when the crack tip cannot keep up with the general corrosion rate of the crack sides or when a critical level of sulfide ions cannot be maintained at the crack tip. The crack propagation rate at which this transition occurs may depend on the DO level, flow rate, etc. Based on these factors, the maximum and minimum environmentally assisted crack propagation rates have been defined by Ford et al.,[18] Ford and Andresen,[52] and Ford.[53] For crack-tip sulfide ion concentrations above the critical level, CGR is expressed as

$$da/dt = 2.25 \times 10^{-4}(\dot{\varepsilon}_{ct})^{0.35}; \tag{11}$$

for crack-tip sulfide ion concentrations below the critical level, it is expressed as

$$da/dt = 10^{-2}(\dot{\varepsilon}_{ct})^{1.0}. \tag{12}$$

Assuming that $\dot{\varepsilon}_{ct}$ is approximately the same as the applied strain rate $\dot{\varepsilon}_{app}$, the growth rates predicted by Eqs. 11 and 12 are somewhat higher than those observed experimentally.[21] To be consistent with the experimental data, the constants in Eqs. 11 and 12 were decreased by a factor of 3.2 and 2.5, respectively. If in addition it is assumed that crack advance due to mechanical fatigue is insignificant during the initial stages of fatigue damage, crack advance per cycle from Eq. 11 for significant environmental effects is given by

$$da/dN = 7.03 \times 10^{-5}(\Delta\varepsilon - \varepsilon_f)(\dot{\varepsilon}_{app})^{-0.65}, \tag{13}$$

and from Eq. 12 for moderate environmental effects is given by

$$da/dN = 4.00 \times 10^{-3}(\Delta\varepsilon - \varepsilon_f), \tag{14}$$

where $\dot{\varepsilon}_{app}$ is the applied strain rate (s^{-1}) and ε_f is the threshold strain range needed to rupture the oxide film; ε_f was assumed to be 0.0023 and 0.0029, respectively, for CSs and LASs. For strain rates $\geq\approx$0.3%/s, da/dN is lower from Eq. 13 than from Eq. 14. Also, existing fatigue S–N data indicate that strain rate effects on life saturate at ≈0.001%/s.[10] Therefore, Eq. 13 can be applied at rates between 0.003 and 0.00001 s^{-1}; $\dot{\varepsilon}_{app}$ is assumed to be 0.003 s^{-1} for higher values, and 0.00001 s^{-1} for lower values. Equations 13 and 14 assume that the stress–free state for the surface oxide film is at peak compressive stress.

Studies on crack initiation and crack growth in smooth fatigue specimens indicate that the reference fatigue CGR curves (Fig. A1 in the Appendix) for carbon and low–alloy steels in LWR environments are somewhat higher than those determined experimentally from the growth of mechanically small cracks in LWR environments.[21] Furthermore, use of reference CGR curves and fracture mechanics analyses to examine the fatigue S-N behavior of these steels in LWR environments yields conservative results. Therefore, the reference fatigue CGR curves were modified to estimate the growth rates of mechanically small cracks; the modified curves are shown in Fig. 6. The threshold values of ΔK (MPa·$m^{1/2}$) are given by

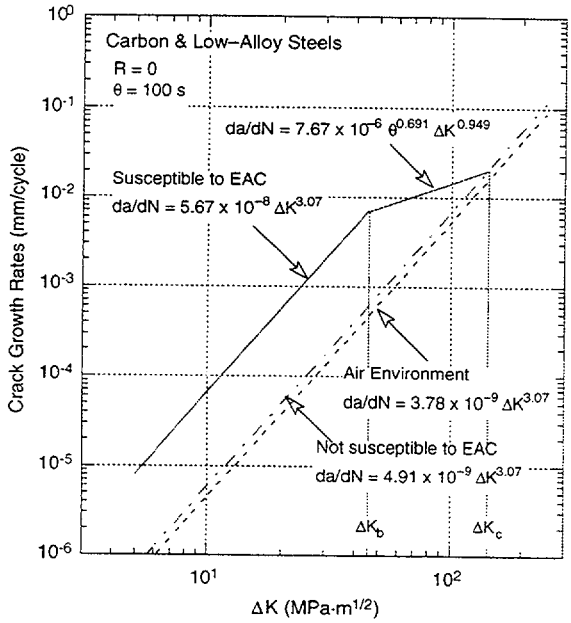

Figure 6.
Modified reference fatigue crack growth rate curves for carbon and low–alloy steels for LWR applications

$$\Delta K_b = 10.11\ \theta^{0.326}, \quad (15)$$

and

$$\Delta K_c = 32.03\ \theta^{0.326}, \quad (16)$$

where rise time θ is in seconds.

Environmental effects on fatigue life are moderate when any one of the threshold environmental conditions is not satisfied, e.g., temperature <150°C, DO <0.05 ppm, strain rate >1%/s, or strain range is below the critical value. For moderate environmental effects, the growth rates of mechanically small cracks are represented by the curves for materials not susceptible to EAC, and those of MSCs, by either Eq. 14 or Eq. 9, whichever yields the higher value. For example, at high strain ranges, growth rates determined from Eq. 9 can be higher than those determined from Eq. 14, i.e., mechanical factors control crack growth and environmental effects are insignificant.

Environmental effects on fatigue life are significant when all of the threshold conditions are satisfied, e.g., temperature ≥150°C, DO ≥0.05 ppm, strain rate <1%/s, and strain range is above the critical value. A minimum threshold sulfur content of 0.005 wt.% was also considered, i.e., sulfur content must also be >0.005 wt.% for significant environmental effects on fatigue life. When all five threshold conditions are satisfied, the growth rates of mechanically small cracks are represented by the curve for materials susceptible to EAC for ΔK values below ΔK_b, by the curve for materials not susceptible to EAC at ΔK values above ΔK_c, and by the transition curve for in-between values of ΔK. The growth rates of MSCs are represented by either Eq. 13 or Eq. 9, whichever yields the higher value.

2.4.3 Estimates of Fatigue Life

The existing fatigue S-N data for carbon and low-alloy steels in air and LWR environments were examined with the present model, in which fatigue life consists of the growth of MSCs and mechanically small cracks. The former may be defined as the initiation stage and represents the growth of MSCs from 10 to 200 μm. The growth of mechanically small cracks may be defined as the propagation stage and represents the growth of fatigue cracks from 200 to 3000 μm. During the initiation stage, the growth of MSCs is expressed by a modified Hobson relationship in air (Eq. 9) and by the slip dissolution/oxidation process in water (Eqs. 13 or 14). During the propagation stage, the growth of mechanically small cracks is characterized in terms of the J-integral range ΔJ and CGR data in air and LWR environments (Fig. 6). The correlations for calculating the stress range, stress intensity range ΔK, J-integral range ΔJ, and the CGRs for long cracks in air are given in the appendix. For the cylindrical fatigue specimens, the stress intensity ranges ΔK were determined from the values of the J-integral range ΔJ. Although ΔJ is often computed only for that portion of the loading cycle during which the crack is open, in the present study, the entire hysteresis loop was used when we estimated ΔJ.[49] The stress intensities associated with conventional cylindrical fatigue specimens were modified according to the correlations developed by O'Donnell and O'Donnell.[54] Typical CGRs and crack growth behavior during fatigue crack initiation in air and water environments are shown in Figs. 7 and 8, respectively.

Experimental values of fatigue life and those predicted from the present model in air and low- and high-DO water are plotted in Fig. 9. The predicted fatigue lives in air show excellent agreement with the experimental data; the predicted values in LWR environments, particularly in high-DO water, are slightly lower than the experimental values. The differences in predicted and experimental fatigue lives in LWR environments are most likely due to crack closure effects that are expected to be significant at low strain amplitudes. The fatigue S-N curves developed from the present model and those obtained from the statistical models in air and in PWR and BWR environments are shown in Figs. 10 and 11, respectively.

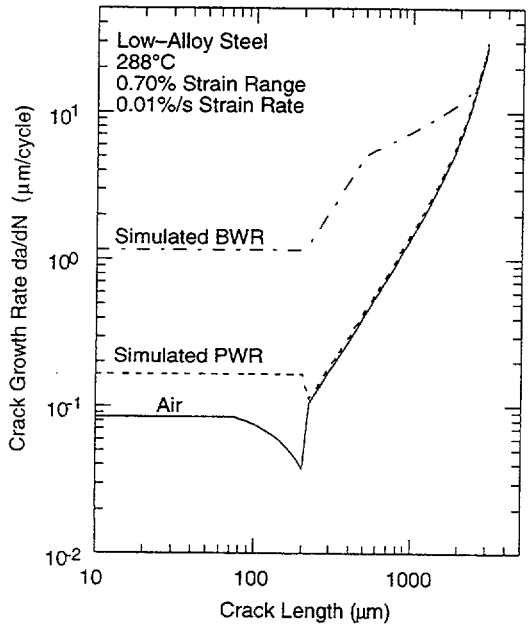

Figure 7.
Crack growth rates during fatigue crack initiation in low-alloy steel in air and simulated PWR and BWR environments

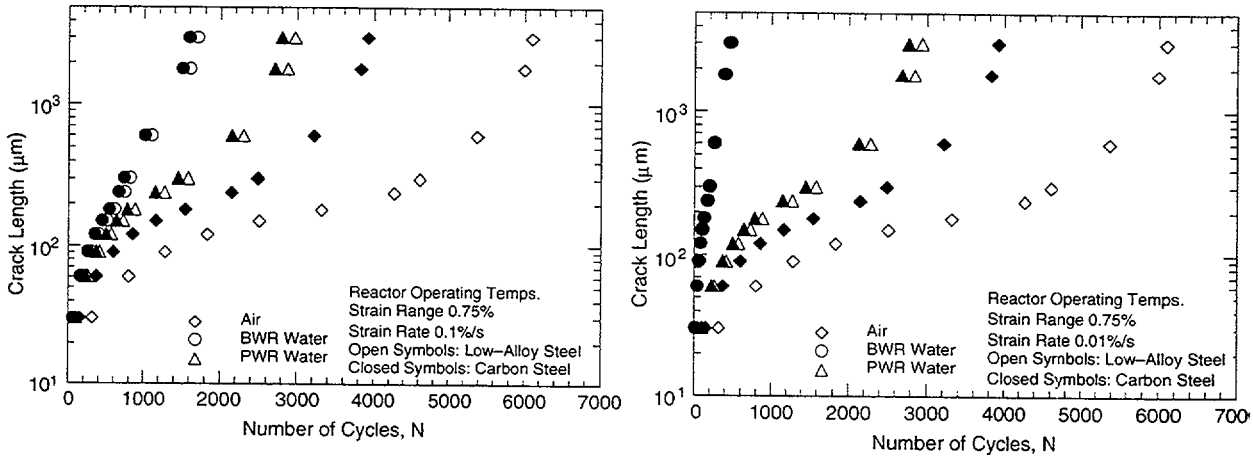

(a) (b)

Figure 8. Crack growth in carbon and low-alloy steels as a function of fatigue cycles at two strain rates of (a) 0.1%/s and (b) 0.01%/s

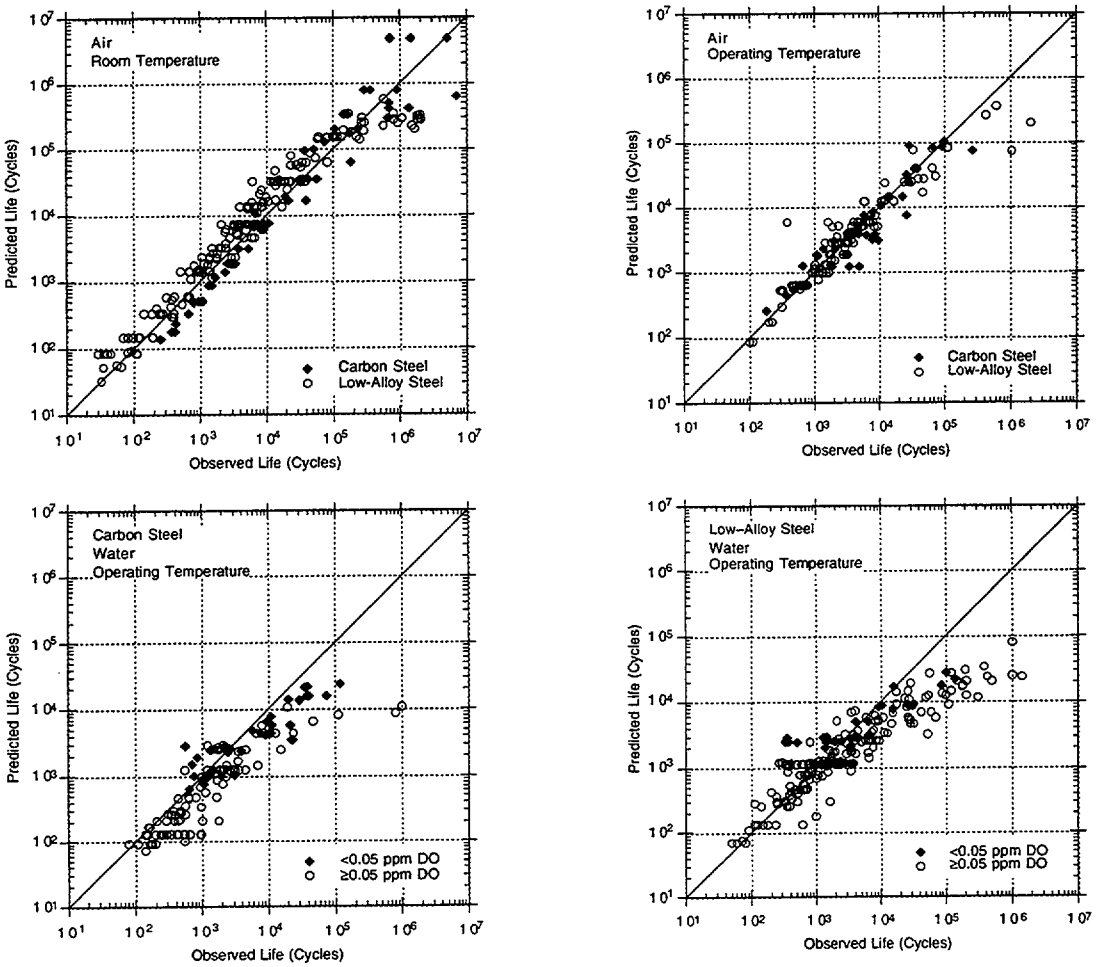

Figure 9. Experimentally observed values of fatigue life of carbon and low–alloy steels vs. those predicted by the present model in air and water environments

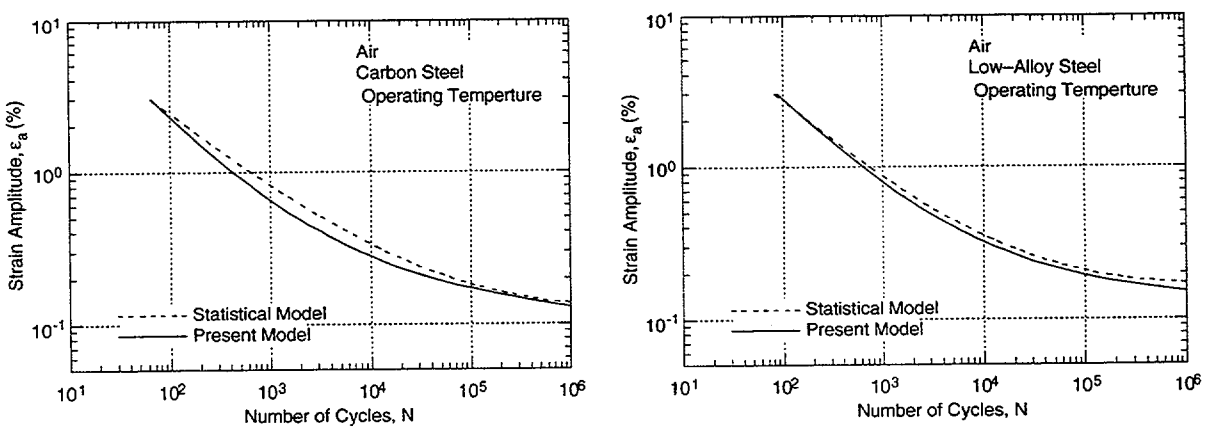

Figure 10. Fatigue strain–vs.–life curves developed from the present model for carbon and low–alloy steels in air

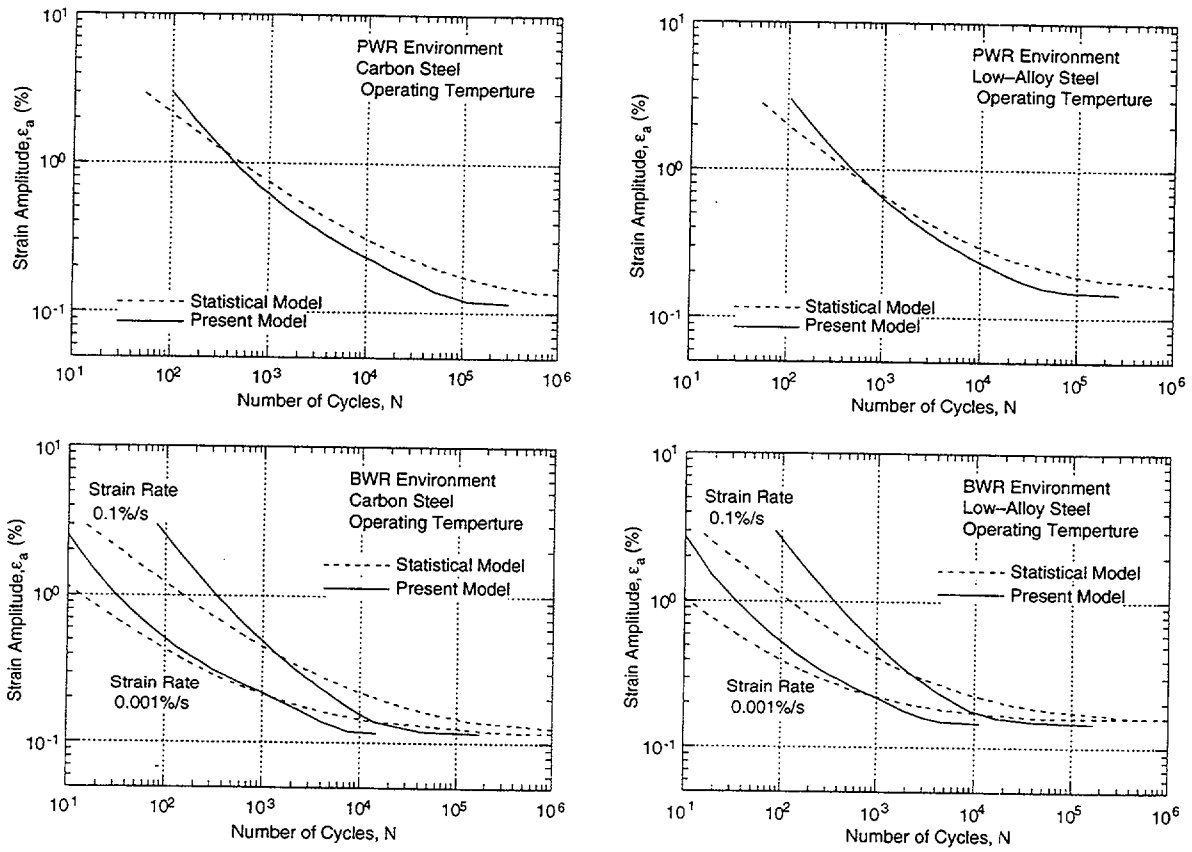

Figure 11. Fatigue strain–vs.–life curves developed from the present model for carbon and low–alloy steels in LWR environments

3 Irradiation–Assisted Stress Corrosion Cracking of Austenitic SS

3.1 Introduction

Failures of some reactor core internal components have been observed after accumulation of fast neutron fluence of $>0.5 \times 10^{21}$ n cm^{-2} (E >1 MeV), or ≈0.7 dpa, in BWRs and at approximately one order of magnitude or higher fluences in some PWR core internal components. The general pattern of the observed failures indicates that as nuclear plants age and fluence increases, various nonsensitized SSs become susceptible to intergranular (IG) failure. Some components have cracked under minimal applied stress. Although most failed components can be replaced (e.g., PWR baffle-former bolts), some safety–significant structural components (e.g., the BWR top guide, shroud, and core plate and PWR baffle plate) would be very difficult or costly to replace. Therefore, the structural integrity of these components has been a subject of concern, and extensive research has been conducted to provide an understanding of this type of degradation, which is commonly known as IASCC.[55–93]

Irradiation produces profound effects on local coolant water chemistry and component microstructure. Neutron irradiation alters local microchemistry, microstructure, and mechanical properties of core internal components, which are usually fabricated from ASTM Types 304, 304L, 316, or 348 SS. Irradiation produces defects, defect clusters, and defect-impurity complexes in grain matrices, and alters dislocation and dislocation loop structures that lead to radiation-induced hardening, and in many cases, flow localization via dislocation channeling. Irradiation also leads to changes in the stability of second–phase precipitates and the local alloy chemistry near grain boundaries, precipitates, and defect clusters. Grain–boundary microchemistry that differs significantly from bulk composition can be produced in association with not only radiation–induced segregation but also thermally driven equilibrium and nonequilibrium segregation of alloying and impurity elements.

Irradiation–induced grain–boundary depletion of chromium has been considered for many years to be the primary metallurgical process that causes IASCC. One of the most important factors that has been considered by many investigators to support the chromium–depletion mechanism is the observation that dependence on water chemistry (i.e., oxidizing potential) of IGSCC of nonirradiated thermally sensitized material and of IASCC of BWR–irradiated solution–annealed material is similar. Other investigators have implicated radiation–induced segregation of ASTM–specified impurities such as silicon, phosphorus, sulfur, and other minor impurities not specified in the ASTM specification. However, the exact mechanism of IASCC still remains unknown. In general, IASCC is characterized by strong heat-to-heat variation in susceptibility, in addition to strong effects of irradiation conditions, material type, and grade, even among materials of virtually identical chemical composition. This characterization indicates that the traditional interpretation based on the role of grain-boundary chromium depletion alone cannot completely explain the IASCC mechanism.

Therefore, an testing program on irradiated materials has been conducted at Argonne National Laboratory (ANL) to systematically investigate the effects of alloying and impurity elements (chromium, nickel, silicon, phosporus, sulfur, manganese, carbon, and nitrogen) on the susceptibility of austenitic SSs to IASCC at several fluence levels. In previous studies, SSRT tests and fractographic analysis were conducted on model austenitic SS specimens irradiated at 289°C in helium in the Halden reactor to a "low-fluence" level of $\approx 0.3 \times 10^{21}$

n cm^{-2} (E >1 MeV), or ≈0.43 dpa and to a "medium-fluence" level of ≈0.9 x 10^{21} n cm^{-2} (E >1 MeV), or ≈1.3 dpa.[94-96]

This report describes results of further analysis of SSRT data and posttest fractographs that were obtained for the "medium-fluence" specimens irradiated to ≈0.9 x 10^{21} n cm^{-2} (E >1 MeV). An initial batch of SSRT specimens irradiated to a "high-fluence" level of ≈2.0 x 10^{21} n cm^{-2} (E >1 MeV), or ≈3 dpa, were also received from the Halden Reactor Project. In continuation of previous efforts,[87,90,91] failure behavior of field-cracked BWR core shroud welds and laboratory-fabricated mockup core shroud welds were also analyzed by transmission electron microscopy (TEM). Observation of unusual microcavities on or near grain boundaries of the heat-affected zone (HAZ) of these welds are reported.

3.2 Slow-Strain-Rate-Tensile Test of Model Austenitic Stainless Steels Irradiated to Medium Fluence (H. M. Chung, D. Perkins, and R. V. Strain)

The irradiation test matrix consists of 27 model austenitic SS alloys. The composition of these alloys is given in Table 2. Of these 27 alloys, eight were commercially fabricated heats of

Table 2. Elemental composition of 27 commercial and laboratory model austenitic stainless steel alloys irradiated in the Halden Reactor

ANL	Source	Composition (wt.%)										
ID[a]	Heat ID	Ni	Si	P	S	Mn	C	N	Cr	O	B	Mo or Nb
C1	DAN-70378	8.12	0.50	0.038	0.002	1.00	0.060	0.060	18.11	-	<0.001	-
L2	BPC-4-111	10.50	0.82	0.080	0.034	1.58	0.074	0.102	17.02	0.0065	<0.001	-
C3	PNL-C-1	8.91	0.46	0.019	0.004	1.81	0.016	0.083	18.55	-	<0.001	-
L4	BPC-4-88	10.20	0.94	0.031	0.010	1.75	0.110	0.002	15.80	-	<0.001	-
L5	BPC-4-104	9.66	0.90	0.113	0.028	0.47	0.006	0.033	21.00	-	<0.001	-
L6	BPC-4-127	10.00	1.90	0.020	0.005	1.13	0.096	0.087	17.10	0.0058	<0.001	-
L7	BPC-4-112	10.60	0.18	0.040	0.038	1.02	0.007	0.111	15.40	0.0274	<0.001	-
L8	BPC-4-91	10.20	0.15	0.093	0.010	1.85	0.041	0.001	18.30	-	<0.001	-
C9	PNL-C-6	8.75	0.39	0.013	0.013	1.72	0.062	0.065	18.48	-	<0.001	-
C10	DAN-23381	8.13	0.55	0.033	0.002	1.00	0.060	0.086	18.19	-	<0.001	-
L11	BPC-4-93	8.15	0.47	0.097	0.009	1.02	0.014	0.004	17.40	-	<0.001	-
C12	DAN-23805	8.23	0.47	0.018	0.002	1.00	0.060	0.070	18.43	-	<0.001	-
L13	BPC-4-96	8.18	1.18	0.027	0.022	0.36	0.026	0.001	17.40	-	<0.001	-
L14	BPC-4-129	7.93	1.49	0.080	0.002	1.76	0.107	0.028	15.00	0.0045	<0.001	-
L15	BPC-4-126	8.00	1.82	0.010	0.013	1.07	0.020	0.085	17.80	0.0110	<0.001	-
C16	PNL-SS-14	12.90	0.38	0.014	0.002	1.66	0.020	0.011	16.92	-	<0.001	-
L17	BPC-4-128	8.00	0.66	0.090	0.009	0.48	0.061	0.078	15.30	0.0092	<0.001	-
L18	BPC-4-98	8.13	0.14	0.016	0.033	1.13	0.080	0.001	18.00	-	<0.001	-
C19	DAN-74827	8.08	0.45	0.031	0.003	0.99	0.060	0.070	18.21	-	<0.001	-
L20	BPC-4-101	8.91	0.017	0.010	0.004	0.41	0.002	0.002	18.10	-	<0.001	-
C21[b]	DAN-12455	10.24	0.51	0.034	0.001	1.19	0.060	0.020	16.28	-	<0.001	Mo 2.08
L22[c]	BPC-4-100	13.30	0.024	0.015	0.004	0.40	0.003	0.001	16.10	-	<0.001	Mo 2.04
L23[d]	BPC-4-114	12.04	0.68	0.030	0.047	0.96	0.043	0.092	17.30	0.0093	<0.001	Nb 1.06
L24[e]	BPC-4-105	12.30	0.03	0.007	0.005	0.48	0.031	0.002	16.90	0.0129	<0.001	Nb 1.72
L25C3	BPC-4-133	8.93	0.92	0.020	0.008	1.54	0.019	0.095	17.20	0.0085	0.010	-
L26C19	BPC-4-131	8.09	0.79	0.004	0.002	0.91	0.070	0.089	17.20	0.0080	<0.001	-
L27C21	BPC-4-132	10.30	0.96	0.040	0.002	0.97	0.057	0.019	15.30	0.0058	0.030	Mo 2.01

[a]First letters "C" and "L" denote commercial and laboratory heats, respectively.
[b]Commercial-purity Type 316 SS.
[c]High-purity Type 316 SS.
[d]Commercial-purity Type 348 SS.
[e]High-purity Type 348 SS.

Types 304, 304L, and 316 SS. The prefix "C" was added to the identification number of these eight commercial heats, i.e., Heats C1, C3, C9, C10, C12, C16, C19, and C21 in Table 2. The remaining 19 heats were fabricated in the laboratory; all were designated with identification numbers that began with "L."

The SSRT specimens were irradiated in the Halden boiling heavy-water reactor in six helium-filled capsules maintained at 289°C. All SSRT tests were conducted in a low-activity-level hot cell in simulated BWR-like water at 289°C. Dissolved oxygen in the water was maintained at ≈8 ppm. Conductivity and pH of the water were kept at ≈0.07-0.10 and 6.3-6.8, respectively. Strain rate was held constant at 1.65×10^{-7} s^{-1}. Electrochemical potential (ECP) was measured on the effluent side at regular intervals. Results of SSRT tests and fractographic analysis, completed for the alloys that were irradiated to a fluence of $\approx 0.9 \times 10^{21}$ n cm^{-2} (E >1 MeV), are summarized in Tables 3 and 4. In Table 3, test conditions, results of SSRT tests, and fractographic characteristics (percent IGSCC, percent TGSCC, and combined percent IGSCC+TGSCC) are listed. These results are correlated with compositional characteristics of the alloys in Table 4.

Table 3. Stress corrosion test conditions, results of SSRT[a] tests and SEM fractographic characteristics for model austenitic stainless steel alloys irradiated to 0.9×10^{21} n cm^{-2} (E >1 MeV)

Alloy &		Feedwater Chemistry				SSRT Parameters				Fracture Behavior		
Spec.		Oxygen	Average	Cond.		Yield	Max.	Uniform	Total			TGSCC
Ident.	SSRT	Conc.	ECP	at 25°C	pH	Stress	Stress	Elongation	Elongation	TGSCC	IGSCC	IGSCC
No.	No.	(ppm)	(mV SHE)	($\mu S \cdot cm^{-1}$)	at 25°C	(MPa)	(MPa)	(%)	(%)	(%)	(%)	(%)
L22-02	HR-17	8.0	+181	0.08	6.77	475	549	4.20	5.82	30	35	65
L11-02	HR-18	8.0	+191	0.08	6.55	820	856	0.43	1.65	50	14	64
L18-02	HR-19	8.0	+193	0.10	6.07	710	755	3.98	5.05	38	14	52
L20-02	HR-28	Test in 289°C Air				826	845	0.31	2.09	0	0	0
L20-05	HR-26	9.0	+182	0.09	6.32	670	743	0.37	1.03	0	0	0
L20-06	HR-27	8.0	+274	0.07	6.05	632	697	0.85	2.72	0	0	0
C9-02	HR-21	8.0	+240	0.07	6.47	651	679	1.42	2.50	62	22	84
L17-02	HR-22	8.0	+198	0.07	6.42	574	654	2.02	3.08	44	41	85
L7-02	HR-23	8.0	+215	0.07	6.03	553	561	0.24	2.44	38	54	92
C10-02	HR-24	7.0	+221	0.07	5.26	651	706	6.35	9.25	14	0	14
C3-02	HR-25	8.0	+240	0.07	6.34	632	668	16.72	19.74	9	4	13
C19-02	HR-30	Test in 289°C Air				888	894	6.41	10.21	1	0	1
C19-04	HR-31	8.0	+252	0.07	6.18	750	769	6.06	8.79	1	0	1
L6-02	HR-32	8.0	+250	0.07	6.40	493	546	2.45	3.77	8	27	35
L14-02	HR-33	8.0	+246	0.08	6.07	649	684	1.90	4.67	84	2	86
L13-02	HR-34	7.0	+222	0.09	6.85	602	624	1.67	4.95	55	2	57
L04-02	HR-35	7.0	+259	0.08	6.54	634	680	1.07	2.02	68	2	70
L05-02	HR-36	7.0	+243	0.07	6.85	665	725	3.07	4.57	3	5	8
C16-02	HR-37	7.0	+230	0.07	6.62	562	618	11.99	15.80	7	1	8
L8-02	HR-38	8.0	+242	0.07	6.57	838	838	0.12	3.12	15	22	37
C21-02	HR-39	8.0	+231	0.08	6.21	643	716	15.38	18.30	1	2	3
L2-02	HR-40	7.0	+239	0.07	7.11	839	849	0.88	1.56	38	4	42
L24-02	HR-41	8.0	+239	0.06	6.40	725	725	0.15	2.45	2	1	3
L23-02	HR-42	7.0	+237	0.08	6.60	787	818	0.38	1.24	3	24	27
C12-02	HR-43	7.0	+227	0.07	6.19	747	756	14.96	18.57	4	0	4
C1-02	HR-44	8.0	+229	0.07	6.30	707	763	13.36	17.04	2	0	2

[a]Test at 289°C at a strain rate of 1.65×10^{-7} s^{-1} in simulated BWR water that contained ≈8 ppm DO.

Table 4. Composition (wt.%) of model austenitic stainless steel alloys irradiated to 0.9 x 10^{21} n cm^{-2} (E >1 MeV) correlated with results of SSRT[a] tests and SEM fractography.

Alloy ID	Ni	Si	P	S	Mn	C	N	Cr	Mo/Nb	Remark[b]	YS (MPa)	UTS (MPa)	UE (%)	TE (%)	TGSCC (%)	IGSCC (%)	TG+IG SCC (%
L22-02	13.30	0.024	0.015	0.004	0.40	0.003	0.001	16.10	Mo 2.04	HP 316L; low Si, N, S	475	549	4.20	5.82	30	35	65
L11-02	8.15	0.47	0.097	0.009	1.02	0.014	0.004	17.40	-	high P; low Si, C, S, N	820	856	0.43	1.65	50	14	64
L18-02	8.13	0.14	0.016	0.033	1.13	0.080	0.001	18.00	-	low Si, N	710	755	3.98	5.05	38	14	52
L20-05	8.91	0.017	0.010	0.004	0.41	0.002	0.002	18.10	O 0.0940	high O; low Si, N; HP 304L	670	743	0.37	1.03	–	–	–
L20-06	8.91	0.017	0.010	0.004	0.41	0.002	0.002	18.10	O 0.0940	highO: low Si, N; HP 304L	632	697	0.85	2.72	–	–	–
C9-02	8.75	0.39	0.013	0.013	1.72	0.062	0.065	18.48	-	low Si; high Mn	651	679	1.42	2.50	62	22	84
L17-02	8.00	0.66	0.090	0.009	0.48	0.061	0.078	15.30	O 0.0090	high P; low Cr, Mn, S	574	654	2.02	3.08	44	41	85
L7-02	10.60	0.18	0.040	0.038	1.02	0.007	0.111	15.40	O 0.0274	high S, N, O; low Si, C	553	561	0.24	2.44	38	54	92
C10-02	8.13	0.55	0.033	0.002	1.00	0.060	0.086	18.19	-	CP 304; low S; high N	651	706	6.35	9.25	14	0	14
C3-02	8.91	0.46	0.019	0.004	1.81	0.016	0.083	18.55	-	CP 304L; high Mn, N; low S	632	668	16.7	19.7	9	4	13
C19-04	8.08	0.45	0.031	0.003	0.99	0.060	0.070	18.21	O 0.0200	CP 304; low S	750	769	6.06	8.79	1	0	1
L6-02	10.00	1.90	0.020	0.005	1.13	0.096	0.087	17.10	O 0.0058	high Si; low S	493	546	2.45	3.77	8	27	35
L14-02	7.93	1.49	0.080	0.002	1.76	0.107	0.028	15.00	O 0.0045	high Si, P, Mn; low Cr, S	649	684	1.90	4.67	84	2	86
L13-02	8.18	1.18	0.027	0.022	0.36	0.026	0.001	17.40	-	high Si, S; Low Mn, C, N	602	624	1.67	4.95	55	2	57
L4-02	10.20	0.94	0.031	0.010	1.75	0.110	0.002	15.80	-	high Si, C; low N, Cr	634	680	1.07	2.02	68	2	70
L5-02	9.66	0.90	0.113	0.028	0.47	0.006	0.033	21.00	-	high Si, P, Cr; Low Mn, C	665	725	3.07	4.57	3	5	8
C16-02	12.90	0.38	0.014	0.002	1.66	0.020	0.011	16.92	0.0157	high Ni; low P, S, C	562	618	12.0	15.8	7	1	8
L8-02	10.20	0.15	0.093	0.010	1.85	0.041	0.001	18.30	-	high P, Mn; low Si, N	838	838	0.12	3.12	15	22	37
C21-02	10.24	0.51	0.034	0.001	1.19	0.060	0.020	16.28	Mo 2.08	CP 316, low S	643	716	15.4	18.3	1	2	3
L2-02	10.50	0.82	0.080	0.034	1.58	0.074	0.102	17.02	O 0.0066	high O, P, S, N	839	849	0.88	1.56	38	4	42
L24-02	12.30	0.03	0.007	0.005	0.48	0.031	0.002	16.90	Nb 1.72 O 0.0129	HP 348L; low Si, P, S, C, N	725	725	0.15	2.45	2	1	3
L23-02	12.04	0.68	0.030	0.047	0.96	0.043	0.092	17.30	Nb 1.06 O 0.0093	CP 348, high S	787	818	0.38	1.24	3	24	27
C12-02	8.23	0.47	0.018	0.002	1.00	0.060	0.070	18.43	-	304, low S, low P	747	756	15.0	18.6	4	0	4
C1-02	8.12	0.50	0.038	0.002	1.00	0.060	0.060	18.11	-	304, low S	707	763	13.4	17.0	2	0	2

[a]Test at 289°C at a strain rate of 1.65 x 10^{-7} s^{-1} in BWR-simulated water; DO ≈8 ppm, effluent ECP +140 to +236 mV SHE, conductivity at 25°C 0.07-0.11 μS cm^{-1}, and pH 6.2-7.0.
[b]HP = high purity, CP = commercial purity.

3.2.1 Effect of Fluence on Slow-Strain-Rate Tensile Behavior

Results of the SSRT tests provide data on the effects of fluence on strength and ductility of the model austenitic SSs. Figures 12 and 13, respectively, show the effects of fluence on tensile strength (yield and maximum strength) and ductility (uniform and total elongation). As fluence increases, the difference between yield and maximum strength in water decreases, as shown in Fig. , because of decreased work-hardening capability and increased susceptibility to transgranular and intergranular stress corrosion cracking (TGSCC and IGSCC). Figure 14 shows the correlation of total elongation as a function of susceptibility to TGSCC and IGSCC i.e., percent TGSCC + percent IGSCC. Two laboratory alloys L4 and L8 exhibited significantly higher ductility than predicted on the basis of susceptibility to TGSCC and IGSCC. The reason for this behavior is not well known at this time.

The effect of fast fluence on yield strength of the commercial heats of Types 304 and 304L SS irradiated in the Halden reactor are shown in Fig. 15. No data on laboratory-fabricated alloys are included in this plot. Also shown for comparison are similar data reported in the literature for BWR components (neutron absorber tubes and control blade sheath) and sheet specimens irradiated in BWRs. Yield strength increases rapidly at fluences >0.2 x 10^{21} n cm^{-2} (E >1 MeV) and reaches a saturated value of ≈800-850 MPa at fluences >2.0 x 10^{21} n cm^{-2} (E >1 MeV). The effect of carbon concentration (i.e., Type 304 vs. Type 304L SS) appears to be secondary or insignificant when compared with the predominant effect of irradiation-induced damage.

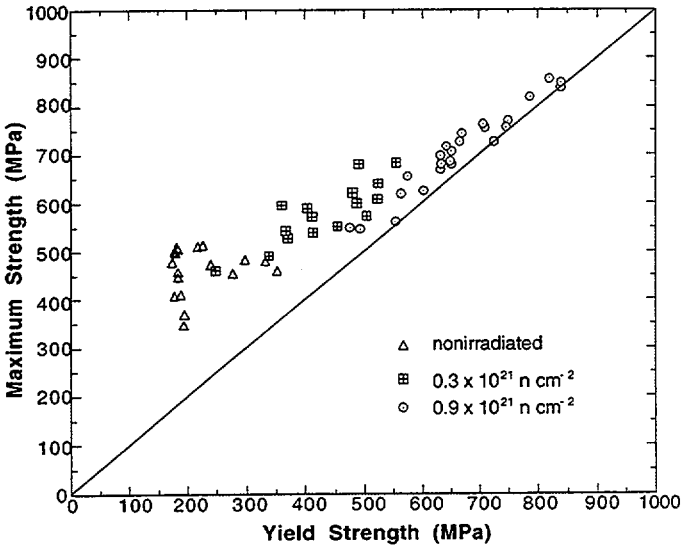

Figure 12.
Effect of fluence on yield and maximum strength of model austenitic stainless steel alloys irradiated in the Halden reactor

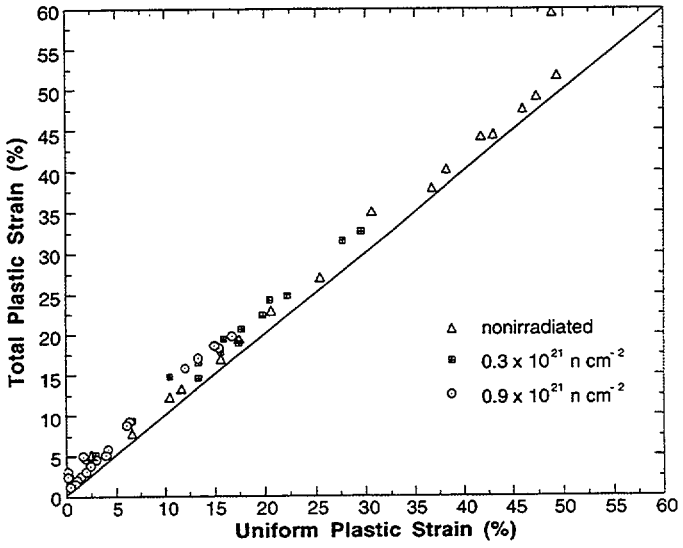

Figure 13.
Effect of fluence on uniform and total elongation of model austenitic stainless steel alloys irradiated in the Halden reactor

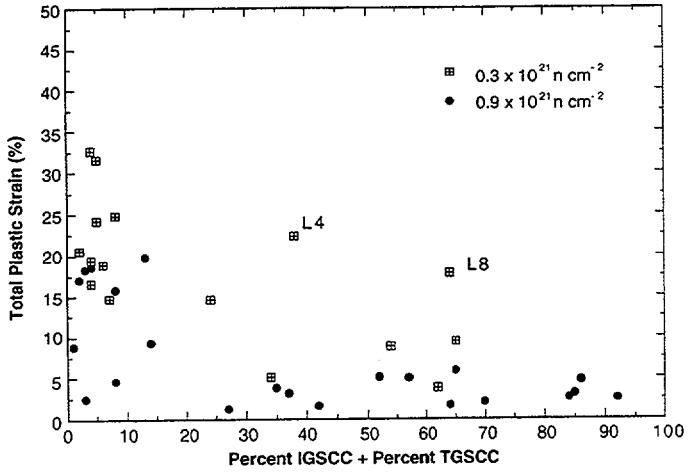

Figure 14.
Total elongation as function of percent TGSCC + percent IGSCC

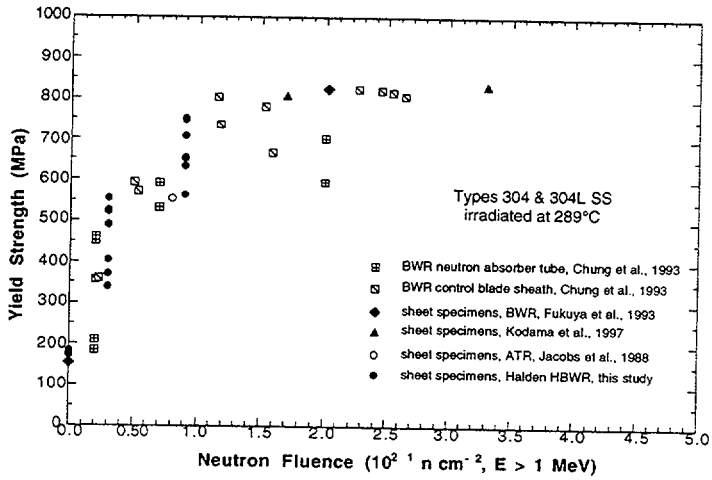

Figure 15.
Effect of fast neutron fluence on yield strength of Types 304 and 304L SS irradiated in BWR or test reactors at 289°C

3.2.2 Effect of Sulfur

Based on the information given in Tables 2 and 3, we examined the relationship between the fracture properties and the compositional characteristics of the alloys to identify the alloying and impurity elements that significantly influence SCC behavior. The effects of silicon on strength and susceptibility to IGSCC were reported previously.[96]

In the unirradiated state or after irradiation to ≈0.3 x 10^{21} n cm^{-2}, commercial and laboratory heats of Types 304, 304L, and 348 SS that contain relatively high concentrations of sulfur (>0.009 wt.% sulfur, 15-18.50 wt.% chromium) exhibited significant susceptibility to TGSCC, whereas alloys that contain a relatively low concentration of sulfur (<0.005 wt.% sulfur) exhibited good resistance to TGSCC. These relationships are shown in Fig. 16.

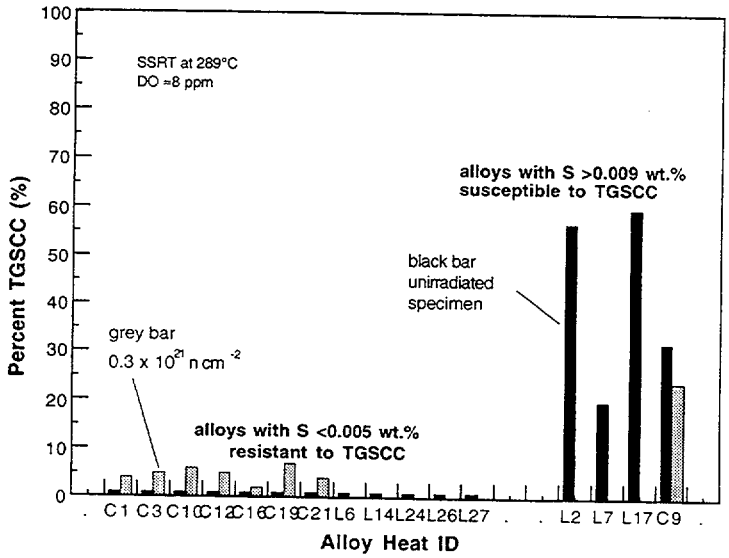

Figure 16.
Effect of sulfur on susceptibility to TGSCC of two groups of alloys in unirradiated state or after irradiation to ≈0.3 x 10^{21} n cm^{-2} (E >1 MeV); one group contains low concentrations of sulfur (<0.005 wt.%) and the other contains relatively high concentrations of sulfur (>0.009 wt.%)

At ≈0.9 x 10^{21} n cm^{-2} (E >1 MeV), commercial heats of Types 304 and 316 SS that contain low concentrations of sulfur (<0.004 wt.% sulfur) exhibited high resistance to TGSCC and IGSCC (see Fig. 17) and high uniform and total elongation (see Fig. 18), whereas a commercial heat of Type 304 SS that contains a relatively high concentration of sulfur (≈0.013 wt.% sulfur) exhibited poor resistance to TGSCC and IGSCC (Fig. 17) and low uniform and total elongation (Fig. 18). Susceptibilities of the high-sulfur heat C9 to TGSCC were high in the nonirradiated state and after irradiation to low fluence (see Fig. 16).

The observations summarized in Figs. 16-18 strongly indicate that for commercial heats of Types 304 and 304L SS, a high concentration of sulfur (>0.009 wt.%) is significantly detrimental and that a sufficiently low concentration of sulfur (e.g., <0.004 wt.%) is a necessary condition for good resistance to IASCC.

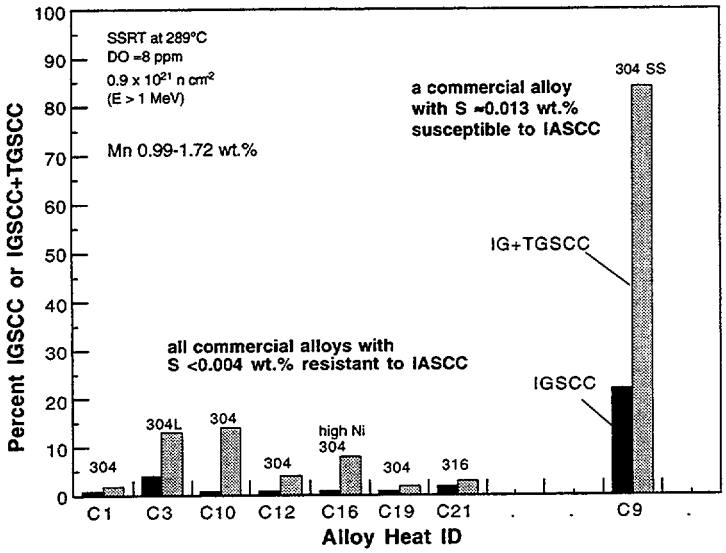

Figure 17.
Effect of sulfur on susceptibility to TGSCC and IGSCC of commercial alloys measured after irradiation to ≈0.9 x 10^{21} n cm^{-2} (E >1 MeV); one group of alloys contains low concentrations of sulfur (<0.004 wt.%) the other, relatively high concentrations of sulfur (>0.013 wt.%)

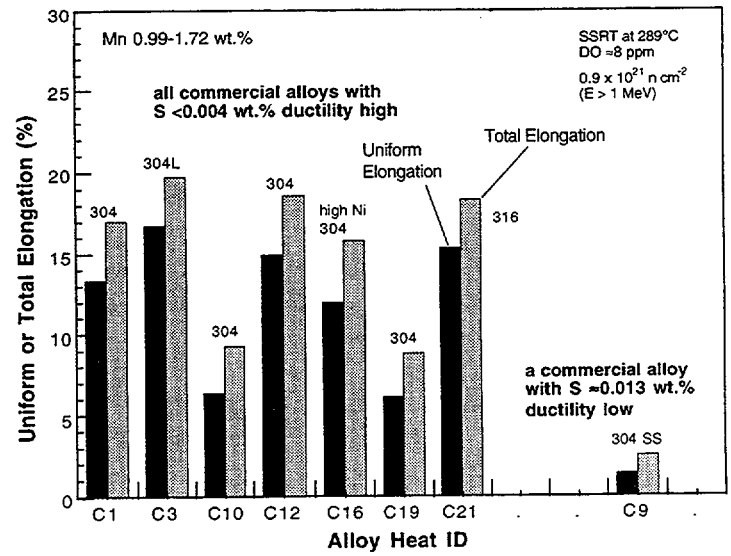

Figure 18.
Effect of sulfur on uniform and total elongation of commercial alloys measured after irradiation to ≈0.9 x 10^{21} n cm^{-2} (E >1 MeV); one group of alloys contains low concentrations of sulfur (<0.004 wt.%), the other, relatively high concentration of sulfur (>0.013 wt.%)

From an earlier study on steels irradiated to ≈2.5 x 10^{21} n cm^{-2} (E >1 MeV) in a BWR, Kasahara et al.[75] reported that the effect of high concentrations of sulfur on IASCC susceptibility was significant for one heat of Type 316L SS that contained 0.035 wt.% sulfur, whereas for a similar heat of Type 316L SS that contained 0.001 wt.% sulfur, susceptibility to IASCC was insignificant. A similar effect of the concentration of sulfur was not observed for two heats of Type 304L SS. In other studies on steels irradiated to ≈0.67 x 10^{21} n cm^{-2} (E >1 MeV), Tsukada et al. reported deleterious effects of high concentrations of sulfur for a heat of Type 304L SS (0.032 wt.% sulfur)[77] and a Ti-doped heat of Type 316 SS (0.037 wt.% sulfur).[84] Although these earlier investigations were conducted on a limited number of heats, the results appear to be consistent with the present observation that a sulfur concentration as low as ≈0.009 wt.% could be deleterious to the susceptibility of steel to TGSCC and IGSCC.

The exact mechanism of how a high concentration of sulfur in Types 304, 304L, or 316 SS leads to higher susceptibilities to TGSCC and IGSCC, as observed in this study, is not clear. In a previous investigation, grain-boundary concentrations of sulfur in BWR neutron absorber tubes and control blade sheath fabricated from several high- and commercial-purity heats of Types 304 and 304L SS and irradiated to ≈2.6 x 10^{21} n cm^{-2} (E >1 MeV) were determined by Auger electron spectroscopy (AES).[68] However, because of sulfur contamination that occurs during the process of anodic charging of hydrogen into the specimen before analysis by AES (which is necessary to induce intergranular fracture in vacuum in an Auger electron microscope and hence reveal grain boundaries of the specimen), a good correlation could not be established between grain-boundary sulfur concentration and susceptibility to IGSCC of the BWR neutron absorber tubes and control blade sheath.

Grain-boundary segregation of sulfur in irradiated steels is also difficult to determine by energy-dispersive spectroscopy (EDS) in a transmission electron or analytical electron microscope. Furthermore, several factors complicate the exact distribution of sulfur in irradiated steels, i.e., trapping of sulfur in MnS and other sulfide precipitates, potential dissolution of MnS and other sulfides in BWR-like water,[97] and irradiation-induced modification of the composition and morphology of MnS precipitates.[89] Therefore, it is not surprising that a good correlation could not be established between grain-boundary sulfur concentration and susceptibility of irradiated steels to IGSCC.

For unirradiated steels, thermally induced grain-boundary segregation of sulfur has been measured by AES by Andresen and Briant[98] for one heat of Type 304L and one heat of 316NG SS that contained 0.030-0.037 wt.% sulfur and were annealed at 400-700°C. Susceptibility of both materials to IGSCC was significant. The former material did not contain any manganese; therefore, IGSCC in that material was attributed to grain-boundary segregation of sulfur. The lower percent IGSCC observed for the latter material, which contained 1.1 wt.% manganese and 0.067 wt.% phosphorus, was attributed to lower grain-boundary segregation of sulfur that may have occurred in the material because phosphorus and sulfur must compete for grain-boundary sites for segregation.

A similar model, based on irradiation-induced grain-boundary segregation of sulfur, does not appear to be consistent with the present observation that a higher concentration of sulfur is conducive to higher susceptibilities to TGSCC and IGSCC. Conclusive evidence and quantitative data of irradiation-induced grain-boundary segregation of sulfur do not appear to have been established in the study of Andresen and Briant.[98] As pointed out previously, the IGSCC fracture surface in high-sulfur steels was often observed in the middle of and

surrounded by a TGSCC fracture surface. This finding appears to indicate that MnS, and possibly other soluble sulfides that may have more complex chemical compositions,[97] dissolves in crack tip water that initially advances via TGSCC and then releases into the crack-tip crevice water deleterious ions that are conducive to producing IGSCC. To identify the exact processes and mechanisms, SSRT tests on higher fluence specimens and a systematic microstructural investigation will be helpful.

3.2.3 Effect of Chromium

At a fluence of ≈0.9 x 10^{21} n cm^{-2}, a laboratory alloy L5 that contains an unusually high concentration of chromium (≈21 wt.%), exhibited excellent resistance to TGSCC and IGSCC, in spite of high sulfur content (≈0.028 wt.%). In contrast to this, several heats that contain relatively low concentrations of chromium (<17.5 wt.%) exhibited significant susceptibility to TGSCC and IGSCC (see Fig. 19). This observation indicates that chromium atoms in high concentration play a major role in suppressing susceptibility to IASCC under BWR conditions.

The IASCC-resistant alloy L5 was found to contain <3 vol.% small (≈2–8 μm) globules of delta ferrite (see Fig. 20). This is not surprising considering that the chromium content in the alloy is ≈21 wt.%. In this case the reduced susceptibility to IASCC is probably simply due to the higher chromium level. In the case of IGSCC due to thermal sensitization, it is well known that when ferrite-austenite phase boundaries exist in significant proportion, intergranular stress corrosion cracks are inherently difficult to propagate. Likewise, it is possible that the presence of delta ferrite could reduce susceptibility to IASCC even if grain-boundary chromium depletion occurs via irradiation-induced process in the austenite phase.

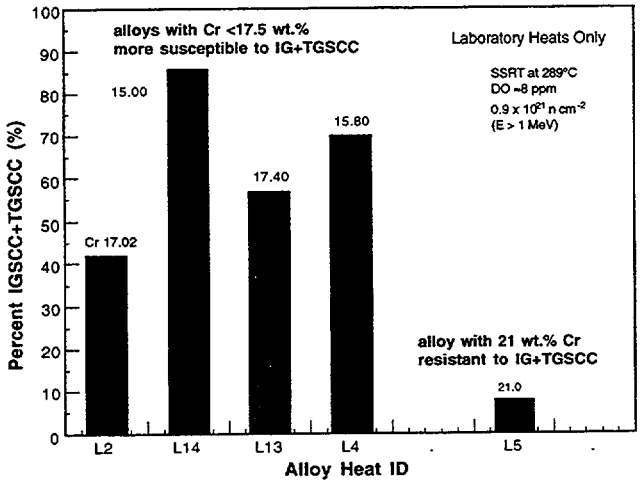

Figure 19.
Effect of chromium on susceptibility to TGSCC and IGSCC of laboratory alloys measured after irradiation to ≈0.9 x 10^{21} n cm^{-2} (E >1 MeV); alloys susceptible to IASCC contain relatively low concentrations of chromium (<17.4 wt.%), an alloy resistant to IASCC contains relatively high concentrations of chromium (≈21.0 wt.%)

3.2.4 Work-Hardening Capability

Although susceptibilities to TGSCC and IGSCC were insignificant and the fracture surface morphology was mostly ductile, some laboratory-fabricated alloys exhibited very low uniform elongation and poor work-hardening capability in water after irradiation to ≈0.9 x 10^{21} n cm^{-2}, i.e., L20 (characterized by dendritic structure and very high oxygen concentration), L8 (304 SS), L23 (348 SS), and L24 (348 SS). These alloys contained unusually high concentrations of oxygen or unusually low concentrations of silicon, or both. To better understand such behavior, which usually indicates severe susceptibility to dislocation

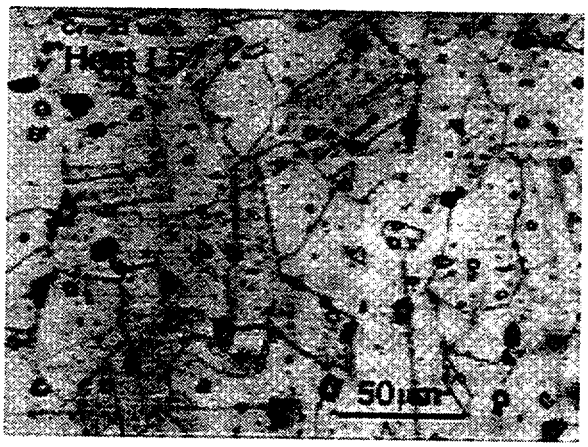

Figure 20.
Optical photomicrograph of IASCC-resistant high-chromium Alloy L5 (21 wt.%), showing twins and 3- to 15-μm-diameter globules of delta ferrite

channeling or other forms of localized deformation, a systematic microstructural investigation by TEM and SEM is desirable.

Laboratory alloys that contain unusually high concentrations of oxygen exhibited either high susceptibility to IGSCC or poor work-hardening capability. Fracture surfaces of such alloys indicated that void coalescence and crack initiation are promoted at or near oxide inclusions that are in high density. Then, ductile tearing of remaining ridges occurs early, leading to low uniform and total elongation. This observation indicates that careful control of oxygen concentration, which is not specified in the ASTM Specifications for austenitic SSs, is a very important factor in minimizing susceptibility to IASCC.

3.3 Phase-II Irradiation Experiment in the Halden Reactor (H. M. Chung, O. K. Chopra, and W. J. Shack)

A total of 28 compact-tension (CT) and 32 SSRT specimens were fabricated, QA-inspected, cleaned, and shipped to the Halden Reactor to initiate the Phase-II Irradiation Experiment, the primary objectives of which are the study of the

(a) Stress corrosion and crack growth behavior of BWR core shroud welds fabricated by shielded-metal- and submerged-arc (SMA and SA) procedures,

(b) Effects of postwelding annealing at 600 and 500°C on stress corrosion and crack growth behavior of core shroud welds,

(c) Effects of grain-boundary optimization on IASCC behavior of Types 304, 304L, 316 SS and Alloy 690,

(d) Effects of oxygen content on IASCC behavior of Type 304 SS,

(e) Resistance of selected heats of Types 316, 316LN, and Ti-modified 316LN SS to IASCC,

(f) IASCC behavior of aged cast duplex SS.

Table 5 lists the type of materials and the history of welding, annealing, and sensitizing heat treatments of the CT and SSRT specimens. These specimens will be loaded into four capsules and irradiated in helium at 289°C to accumulate two levels of fluences, i.e.,

≈0.6 x 10^{21} n cm^{-2} (E >1 MeV) for Capsule 2A and ≈1.2 x 10^{21} n cm^{-2} (E >1 MeV) for Capsules 2B, 2C, and 2D. The scheduled start of the irradiation was fall 2000. Table 6 summarizes capsule-by-capsule information about the target fluence, specimen type (CT or SSRT), and the identification number of each specimen.

Table 5. List of materials to be irradiated and tested in Phase-II Experiment in the Halden Reactor

ID of Alloy or Heat	Material ID Engraved on the Specimen	Description of Material[a]
945	945	high-purity 304L SS, high O
1327	327	high-purity 304L SS, low O
6-23	623	316LN (high N, low C)
6-25	625	316LN, Ti-doped
1151	151	Fe-20Cr-24Ni
L15	L15	304 SS, laboratory heat
2333	333	316 SS
304-BASE	IT304	304 SS, base heat of GB304
316-BASE	IT316	316 SS, base heat of GB316
304L-BASE	304L	304L SS, base heat of GB304L
690-BASE	690	Alloy 690, base heat of GB690
GB304	GB304	Grain-boundary-optimized 304 SS
GB304L	GB304L	Grain-boundary-optimized 304L SS
GB316	GB316	Grain-boundary-optimized 316 SS
GB690	GB690	Grain-boundary-optimized Alloy 690
75	75	CF8M cast SS, aged 400°C/10,000 h
Grand Gulf core shroud	GG (5TA, 5TB, 6TA, 6TB)	304L SS, SAW, as-welded
	GG (3TA-TT, 3TB-TT)	GG SAW, annealed 500°C/24 h
10285	85 (7A, 7B, XA, XB)	304, SMAW, as-welded
	85 (1ATT, 1BTT)	304 SMAW, annealed 500°C/24 h
	85 (2ATT, 2BTT)	304 SMAW, annealed 500°C/24 h
	85 (1TT, 2TT, 3TT, 4TT)	304 SMAW, annealed 600°C/10.5 h
	85 (5A1TT, 5B1TT)	304 SMAW, annealed 600°C/24 h
	85 (5A2TT, 5B2TT)	304 SMAW, annealed 600°C/24 h

[a] SS = stainless steel; SAW = submerged-arc weld; SMAW = shielded-metal-arc weld.

3.4 Microstructural Characteristics of Field-Cracked BWR Core Shroud Welds (H. M. Chung)

To provide a better understanding of the cracking mechanism, failure behavior, and microstructural characteristics of BWR core shroud welds, in this task, we analyzed the welds by advanced metallographic techniques such as analytical electron microscopy (AEM), secondary ion mass spectroscopy (SIMS), and Auger electron spectroscopy (AES). Results of microstructural analyses on field-cracked Types 304 and 304L SS core shroud welds and unirradiated mockup welds have been reported previously.[90,91] Analysis by SIMS was, however, limited to unirradiated mockup welds. A major finding from the earlier studies was that the HAZs of the field-cracked core shroud and mockup welds were contaminated with high levels of oxygen, fluorine, and calcium, the elements that originate from air or the CaF_2-containing coating of the weld electrodes used in the SMA procedure.

Table 6. Target fluence (E >1 MeV), specimen type, and identification number of specimens to be irradiated in four capsules in Phase-II experiment in the Halden Reactor[a]

Capsule 2A (0.6×10^{21} n cm^{-2})	Capsule 2B (1.2×10^{21} n cm^{-2})	Capsule 2C (1.2×10^{21} n cm^{-2})	Capsule 2D (1.2×10^{21} n cm^{-2})
CT, GG5TA	CT, GG6TA	CT, GB304-CT01	CT, GG3TA-TT
CT, GG5TB	CT, GG6TB	CT, GB316-CT01	CT, GG3TB-TT
CT, 85-7A	CT, 85-XA	CT, IT304-CT01	CT, 75-11TT
CT, 85-7B	CT, 85-XB	CT, IT316-CT01	CT, 75-11TM
CT, 85-1ATT	CT, 85-2ATT	SSRT, GB304-02	SSRT, 945-02
CT, 85-1BTT	CT, 85-2BTT	SSRT, GB304-03	SSRT, 945-03
CT, 85-1TT	CT, 85-3TT	SSRT, GB304-13	SSRT, 945-04
CT, 85-2TT	CT, 85-4TT	SSRT, GB304L-06	SSRT, 327-01
CT, 85-5A1TT	CT, 85-5A2TT	SSRT, GB304L-07	SSRT, 327-03
CT, 85-5B1TT	CT, 85-5B2TT	SSRT, GB304L-11	SSRT, 327-04
		SSRT, GB316-08	SSRT, 333-01
		SSRT, GB316-12	SSRT, 333-02
		SSRT, GB316-15	SSRT, 333-04
		SSRT, GB690-10	SSRT, L15-01
		SSRT, GB690-12	SSRT, 151-01
		SSRT, GB690-14	SSRT, 151-02
		SSRT, 304L-01	SSRT, 623-01
		SSRT, 304L-2	SSRT, 623-02
		SSRT, 690-01	SSRT, 625-01
		SSRT, 690-02	SSRT, 625-02
10 CT	10 CT	4 CT, 16 SSRT	4 CT, 16 SSRT

[a] CT = compact tension specimen, SSRT = slow-strain-rate tensile specimen.

Solubilities of oxygen, fluorine, and calcium are negligible or extremely low in austenitic SSs, except at high temperatures when SMA or SA welding passes are made. During cooling after the completion of welding passes or during long-term aging in reactor, oxygen, fluorine, and calcium are, therefore, predicted to segregate either to grain boundaries or to precipitates in the HAZ. Consistent with this prediction, results of previous investigations by AES indicated that concentrations of oxygen and fluorine are significantly higher on grain boundaries of weld HAZs than in the grain matrix.[90,91] Evidence of fluorine segregation to oxides and sulfides in irradiated base-metal components (i.e., BWR neutron absorber rod tubes and control blade sheath) was also reported.[89] On the basis of higher concentration of oxygen or fluorine on grain boundaries of HAZs, a core shroud cracking model was proposed in a previous report.[91]

In field-cracked Types 304[90] and 304L[91] core shroud welds, chromium-rich internal oxides, Fe-Ni spinel oxides, and Ca(O,F) precipitates were observed in high number-density, preferentially on or near grain boundaries of HAZs. However, carbide precipitation was absent or negligible in the HAZs of Types 304 and 304L SS core shroud welds, either on or away from grain boundaries. The absence of carbide precipitation in Type 304 SS weld is attributed to preferential interaction of chromium atoms with oxygen rather than with carbon atoms. These microstructural characteristics were essentially the same for the HAZs of Types 304 and 304L SS core shroud welds, indicating that the cracking mechanism is essentially the same for both types of core shroud welds.

Ca(O,F) precipitates dissolve readily in water, thereby releasing fluorine ions into the crack-tip water. It was suggested that this process exacerbates the susceptibility of core shroud welds to fluorine–catalyzed IGSCC.[91] Consistent with this premise, an unusual microcavity structure was often observed in the HAZs of field-cracked Types 304 and 304L SS core shrouds and several mockup SMA welds. Effort in this reporting period was focused on TEM characterization of this unusual microstructure.

3.4.1 TEM Characterization of Microcavity Structure

Figure 21 shows light-contrasted low- and high-magnification bright-field images of microcavities produced on or near a grain boundary in the HAZ of a mockup SMA weld (Type 304 SS Heat 19611, carbon content 0.060 wt.%).[90] The microcavities were observed during examination in a high-voltage electron microscope (HVEM) operated at 1 MeV or in a CM-30 AEM operated at 200 keV. Thickness fringes near grain-boundary microcavities are visible in Fig. 21b. Figure 22 shows a similar microcavity structure (with microcavities in much higher

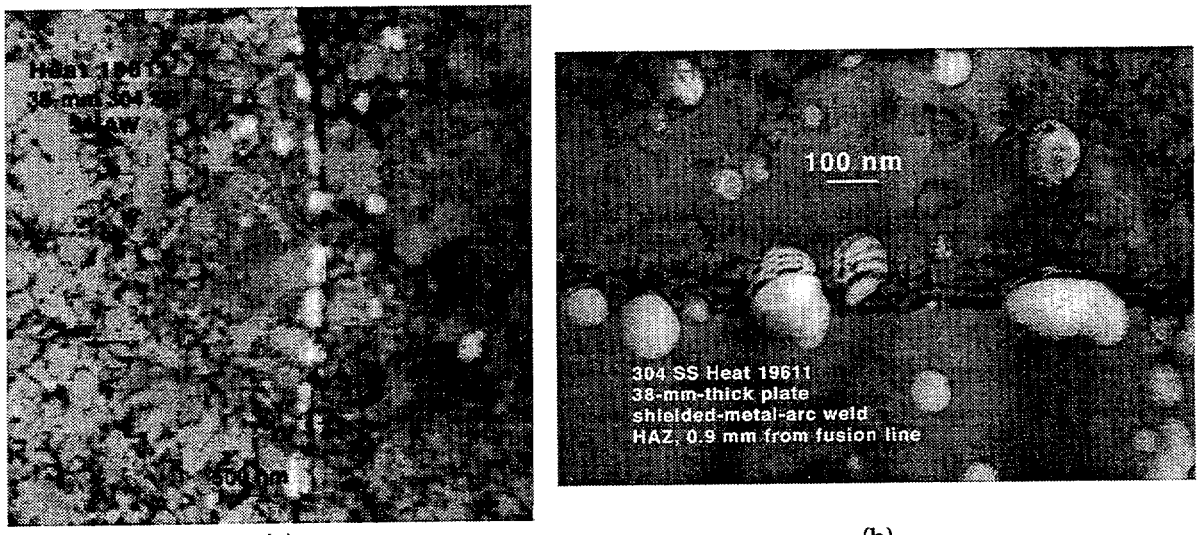

(a) (b)

Figure 21. Microcavities observed in HAZ of shielded-metal-arc weld, Type 304 SS Heat 19611; (a) low magnification in 1-MeV HVEM, (b) high magnification in 200-keV CM-30 TEM

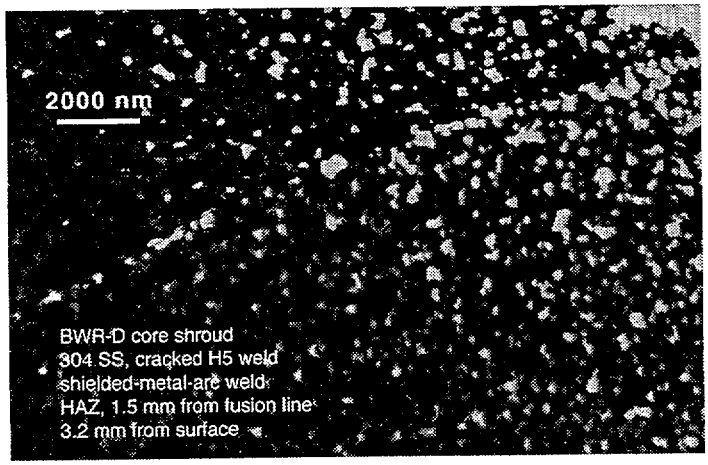

Figure 22.
Unusual microcavity structures in cracked HAZ of BWR-D core shroud weld, Type 304 SS

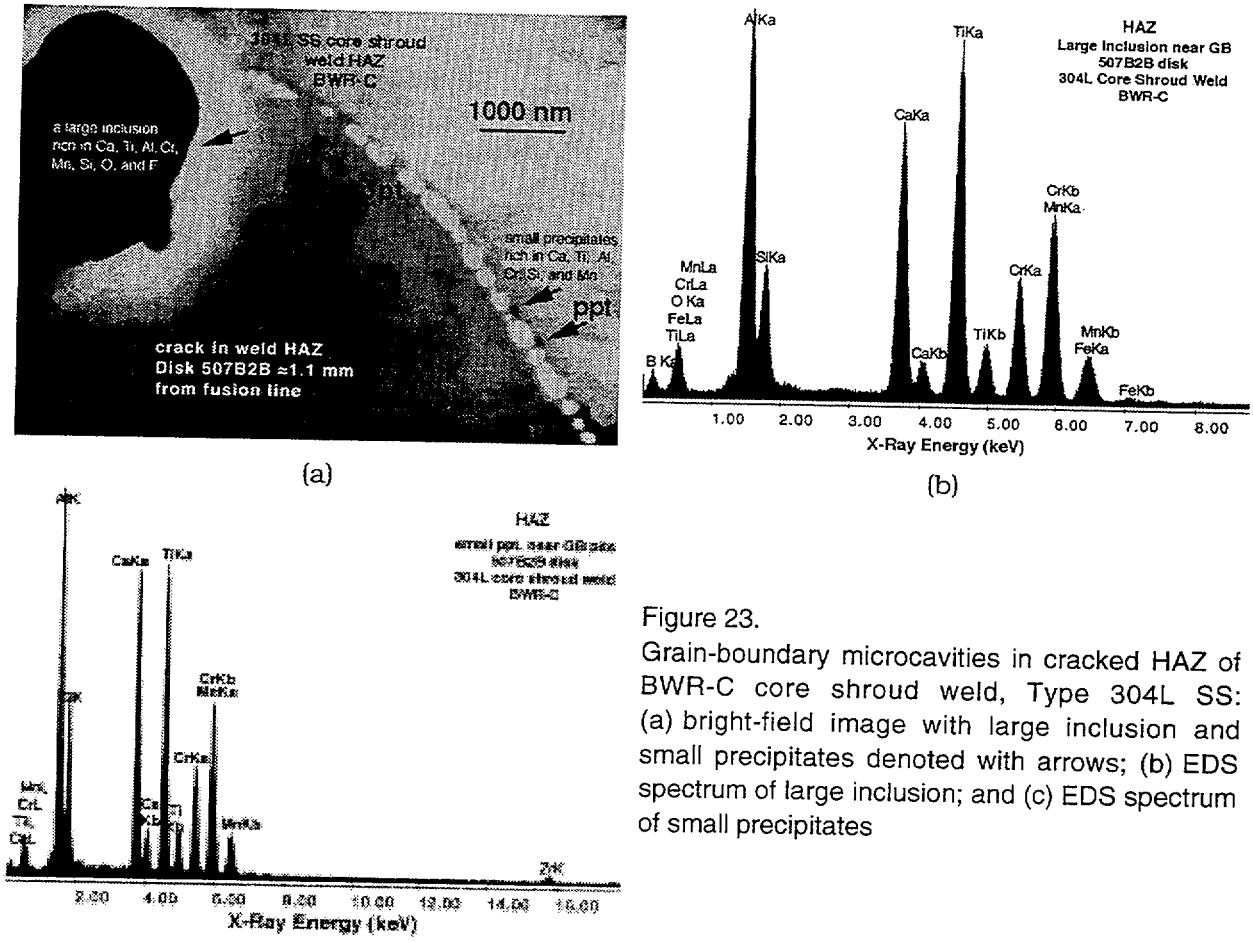

Figure 23.
Grain-boundary microcavities in cracked HAZ of BWR-C core shroud weld, Type 304L SS: (a) bright-field image with large inclusion and small precipitates denoted with arrows; (b) EDS spectrum of large inclusion; and (c) EDS spectrum of small precipitates

number density) that was observed in the HAZ near an in-reactor-produced crack in a horizontal weld of a BWR-D core shroud (Type 304 SS, carbon content 0.063 wt.%).[90] This bright-field image was observed in a JEOL-100CXII TEM operated at 100 keV. Figure 23 shows nearly continuous microcavities that formed on a grain boundary in the HAZ of the cracked BWR-C core shroud weld (Type 304L SS, carbon content 0.027 wt.%).[91]

As shown in Figs. 21–23, there is a tendency for the microcavities to form preferentially on or near grain boundaries. Analyses of three-dimensional images from several stereopairs showed that the light-contrasted features are voids or microcavities (size ≈50-300 nm) contained in the bulk of the HAZ. Although widely varied in number density and volume fraction, similar features were observed in all mockup SMA welds. The microcavities appeared to be in higher number density in regions <1 mm away from the fusion line.

A region at or near a microcavity appeared to be attacked more rapidly by the jet-thinning solution (than the regions away from microcavities) during specimen preparation. The result is that tiny holes were frequently observed in high number density near the edge of the large central perforation of jet-polished specimens. This observation indicates that the chemical composition of the regions near the microcavities differs significantly from the composition of the background material.

To better understand the formation of microcavities, several mockup and BWR core shroud welds, prepared by SMA or gas-tungsten-arc (GTA) procedures from several heats of Types 304, 304L, and 316 SS, were analyzed to determine the absence or presence of the unusual microcavity structure in the HAZ. A summary of these analyses is presented in Table 7. The microcavity structure was observed in all examined SMA welds. However, the characteristic microcavity structure was not observed in the HAZ of any of welds fabricated by GTA procedure.

Table 7. Summary of TEM analysis of microcavity structure in heat-affected zone of mockup and BWR core shroud welds

Steel Type	ANL Heat ID	Fluence (E >1 MeV) ($n\ cm^{-2}$)	Base Metal Carbon (wt.%)	Base Plate Thickness (mm)	Weld Type[a]	Microcavity Detected by TEM
304	C1	0, Mockup	0.060	12.7	SMA	Yes
304	C1	0, Mockup	0.060	12.7	GTA	None
316	C21	0, Mockup	0.060	12.7	SMA	Yes
316	C21	0, Mockup	0.060	12.7	GTA	None
304	19611	0, Mockup	0.060	38	SMA	Yes
304	M9284	0, Mockup	0.050	38	SMA	Yes
304	M9284	0, Mockup	0.050	38	GTA	None
304L Core Shroud	BWR-C	4.6×10^{19}	0.027	38	SMA	Yes
304 Core Shroud	BWR-D	1.0×10^{20}	0.063	50.8	SMA	Yes

[a] SAW = submerged-arc weld; GTAW = gas-tungsten-arc weld.

3.4.2 Supporting Analyses by EDS

From Fig. 23a, it can be observed that the grain-boundary microcavities in the HAZ of the Type 304L SS core shroud weld are associated with the presence of a large inclusion and small precipitates that are near the grain boundary. The compositions of the large inclusion and the small precipitates were analyzed by X-ray energy dispersive spectroscopy (EDS). The results, given in Figs. 23b and c, show, respectively, that the large inclusion and the small precipitates have high concentrations of aluminum, silicon, calcium, titanium, chromium, manganese, and oxygen. These compositions are similar to those of the coating material of the welding electrodes or powders used in core shroud welding. Such weld flux compounds typically contain $CaCO_3$, CaF_2, SiO_2, TiO_2, and Al_2O_3.[90] Also, Type 308 SS weld electrodes contain iron, chromium, manganese, and silicon. The EDS spectrum shown in Fig. 23c is in fact similar to that reported for surface weld scale formed on an SMA weld of a commercial heat of Type 304 SS.[90]

Considering these observations, the large inclusion and the small precipitates in Fig. 23a are believed to have originated from a particle of broken weld scale that was incorporated in the metal during the process of mechanical grinding and wire-brushing of the weld cusps.[90] Therefore, formation of the characteristic microcavities appears to be associated with contamination of the weld HAZ and is a unique microstructural feature that occurs in SMA or SA welds. It is not clear, however, whether the microcavities observed in the BWR-D and -C core shroud welds were produced during welding, during neutron irradiation in the reactor, or during electron irradiation in TEM.

3.4.3 Supporting Analyses by AES

As reported previously, dense oxides were observed by optical microscopy and by AES on in-situ-fractured grain boundaries and grain-boundary triple points in the HAZ of a field-cracked Type 304L SS core shroud weld.[91] This observation indicates that oxygen atoms segregate to grain boundaries of weld HAZs, either during welding, during service in-reactor, or both. More direct evidence for oxygen distribution near grain boundaries was obtained by AES via an automated depth-profiling technique. Such a result, shown in Fig. 24, was obtained from a grain-boundary spot ≈5,000 nm away from any visible oxides (i.e., ≈10 times greater than the radius of the beam).

For intergranular or ductile fracture surfaces produced in-situ in neutron-irradiated base-metal components (such as BWR neutron absorber tubes), oxygen distribution near a grain boundary was difficult to determine because significant chemisorption of oxygen occurred (at ≈23°C) as a result of exposure to the ultrahigh-vacuum environment of the scanning Auger microscope. This artifact oxygen-rich layer, usually ≈2-3 nm thick, is readily removed after several seconds of Ar-ion sputtering. Subsequently, the oxygen signal reaches an asymptotic level that corresponds to the oxygen concentration of the bulk material (Fig. 24). For such situations, the degree of grain-boundary oxygen segregation could not be determined by AES.

It was also difficult to determine oxygen distribution by EDS in HB603 field-emission-gun scanning transmission electron microscope (FEG-STEM) because the K line of oxygen and the L lines of chromium and iron virtually overlap.

However, in contrast to base-metal components, oxygen chemisorption on in-situ-fractured grain-boundary surfaces of the core shroud weld HAZ (Fig. 24) was insignificant, and no sudden decrease of the oxygen signal was observed during the initial seconds of sputtering in the same scanning Auger microscope. We believe this occurred because the core shroud weld HAZ contains an unusually high concentration of oxygen (Fig. 24). The profile of the 510-eV peak of oxygen, normalized with respect to the primary peak of iron at 703 eV, shows that oxygen concentration is significantly higher on or near the grain boundary than in the grain matrix.

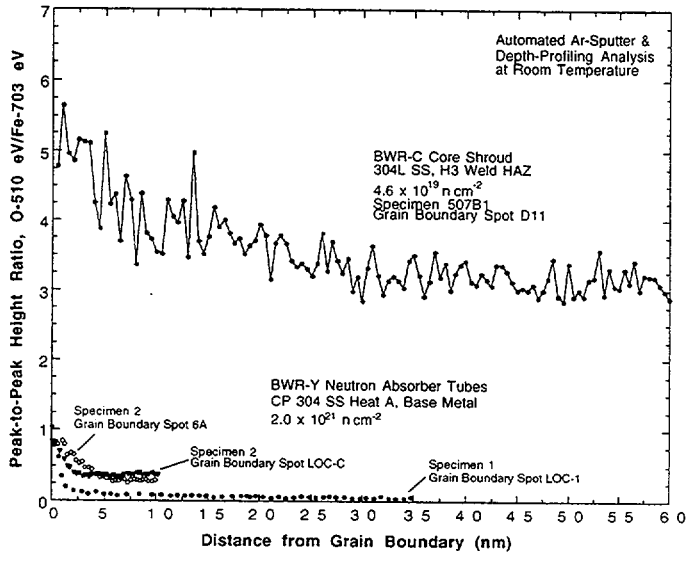

Figure 24.
Peak-to-peak height ratio of Auger electron from O at ≈510 eV to Fe at ≈703 eV as function of distance from grain boundary, Type 304L SS BWR-C core shroud weld HAZ. Similar data for BWR neutron absorber tubes are also shown

Analysis of grain-boundary distribution of fluorine by AES is more difficult, because the primary dN(E)/dE peak of fluorine overlaps the strong iron peak. However, fluorine gives rise to a weak secondary peak at ≈625 eV, and semiquantitative information can be obtained from the behavior of the secondary peak. Although results from such analysis of fluorine cannot be considered quantitative because of this limitation, results of a depth-profiling analysis indicated that relative fluorine concentration is higher on grain boundaries than in grain matrices in the HAZ of the BWR-C core shroud weld. This behavior is shown in Fig. 25.

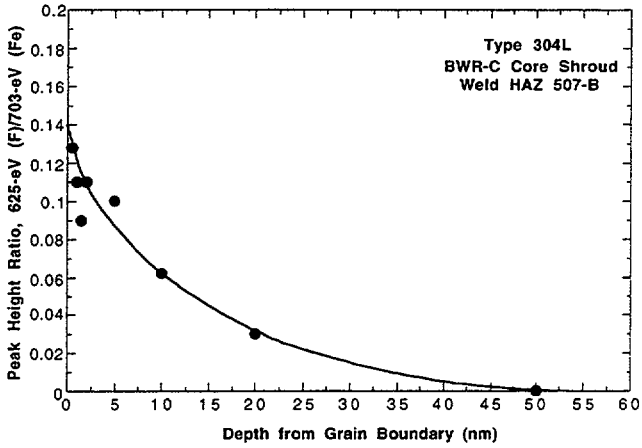

Figure 25.
Fluorine AES signal intensity as function of sputter distance from grain–boundary surface in HAZ of Type 304L SS BWR-C core shroud weld

The information given in Figs. 21–25 indicates that calcium, oxygen, and fluorine tend to concentrate on or near the grain boundaries of the HAZ in core shroud welds. The unusual microcavity structure, observed in the BWR-D core shroud weld and shown in Fig. 22, is in fact strikingly similar to the microcavity structures that were observed in fluorine apatite [$Ca_5(PO_4)_3(F,OH,C)$] which is rich in calcium, oxygen, and fluorine (see Fig. 26, from an unpublished work by Wang and Ewing). The figure shows a labyrinth of microcavities that were produced in calcium-rich material during irradiation with 200-keV electrons. It appears possible that welding-related contamination by calcium, oxygen, and fluorine produces a significantly modified microchemical composition at or near grain boundaries in the HAZ of a BWR core shroud weld, leading to a condition that is susceptible to the formation of microcavities.

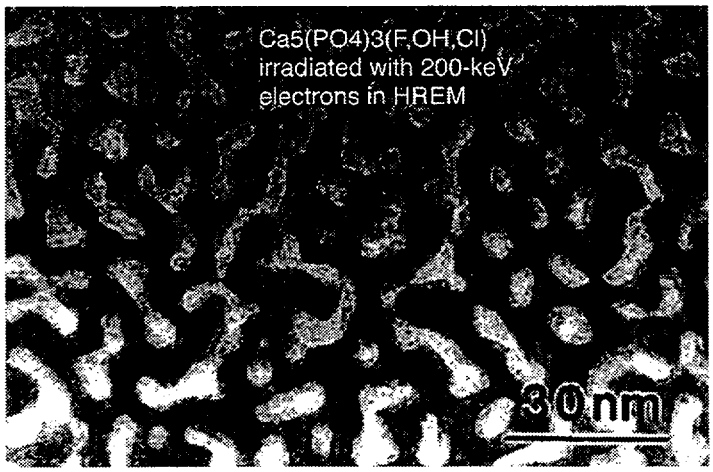

Figure 26.
Microcavities in $Ca_5(PO_4)_3(F,OH,Cl)$ (fluorine apatite) during irradiation with 200-keV electrons reported (but not published) by Wang and Ewing

3.5 Fracture Toughness J–R Test of Austenitic Stainless Steels Irradiated in the Halden Reactor (E. E. Gruber and O. K. Chopra)

3.5.1 Introduction

Austenitic SSs are used extensively as structural alloys in reactor pressure vessel internal components because of their high strength, ductility, and fracture toughness. Fracture of these steels occurs by stable tearing at stresses well above the yield stress, and tearing instabilities require extensive plastic deformation. However, exposure to neutron irradiation for extended periods changes the microstructure and degrades the fracture properties of these steels.

Fracture toughness J–R curve tests have been conducted on two laboratory heats and two commercial heats of Type 304 SS that were irradiated to fluence levels of ≈0.3 and 0.9×10^{21} n cm^{-2} (E >1 MeV) (≈0.45 and 1.35 dpa) at ≈288°C in a helium environment in the Halden boiling heavy water reactor.[99,100] The tests were performed on 1/4–T CT specimens in air at 288°C; crack extensions were determined by both DC potential and elastic unloading compliance techniques. Detailed descriptions of the test facility and procedures are given in Refs. 101 and 102.

Neutron irradiation at 288°C to 0.9×10^{21} n cm^{-2} (E >1 MeV) (1.35 dpa) decreased the fracture toughness of all of the steels. For these materials, minor differences in the chemical composition of the steels, e.g., differences in nickel content for Heats C16 and C19 or silicon content for heats L2 and L20, have little or no effect on the fracture toughness of irradiated steels. The fracture toughness of commercial Heats C16 and C19 was superior to that of laboratory Heats L20 and L2. For steels irradiated to 0.9×10^{21} n cm^{-2} (E >1 MeV) (1.35 dpa), the J_{IC} values are 299 and 304 kJ/m^2, respectively, for Heats C16 and C19; and 38 and 39 kJ/m^2, respectively, for Heats L2 and L20. The data from commercial heats fall within the scatter band for the data obtained on steels that have been irradiated at higher temperatures, i.e., 350–450°C.

During the current reporting period fatigue crack growth tests were conducted in high–purity water at 289°C to establish the test procedure and conditions that will be used for crack growth tests on irradiated materials. Tests were performed in accordance with ASTM E647 "Standard Test Method for Measurement of Fatigue Crack Growth Rates." A mechanical test facility, located outside the hot cell, has been modified to include an autoclave and a recirculating water system for conducting fatigue crack growth tests on 1/4–T CT specimens in simulated LWR environments. The mechanical test facility consists of a test frame mounted on a portable wheeled cart, a recirculating water system, Instron 8500+ electronic control console, hydraulic pump, temperature control units, DC potential rig, two PCs for data acquisition and DC potential measurements, and a strip chart recorder.

3.5.2 Experimental

The test facility is designed for in–cell testing, with the test train, furnace, and other required equipment mounted on top of the portable wheeled cart that can be easily rolled into the cell. A schematic representation of the system is shown in Fig. 27. A small autoclave is installed inside the furnace for conducting tests in simulated LWR environments. The hydraulic actuator is mounted on top of the frame, with the test train components suspended

beneath it. An enlarged drawing of the actuator, load cell, test train, autoclave, and furnace are shown in Fig. 28. The 22.24–kN (5–kip) load cell is at the top of the pull rod. The furnace is mounted on a pneumatic cylinder and can be raised to enclose the autoclave with the load cage and the specimen during the test.

The load cage that contains the test specimen consists of the cover plate of a 1–liter SS autoclave (from PARR Associates) and a 12.7–mm–thick bottom plate separated by four compression rods. The lower two–piece clevis assembly is fastened to the bottom plate of the cage, and the upper piece is connected to the pull rod. A 1/4–T CT or dog bone tensile specimen can be mounted in the clevises with Inconel pins. For resistance measurements, current is passed through the specimen by means of a current clip. A ceramic clip was used initially, however, because of poor compatibility with the high–temperature aqueous environment, it was replaced with a metal clip. Potential leads are attached by spot-welding the platinum leads to short SS pins, which are inserted into threaded holes in the specimens. Water is circulated through a port in the autoclave cover plate that serves both as inlet and outlet.

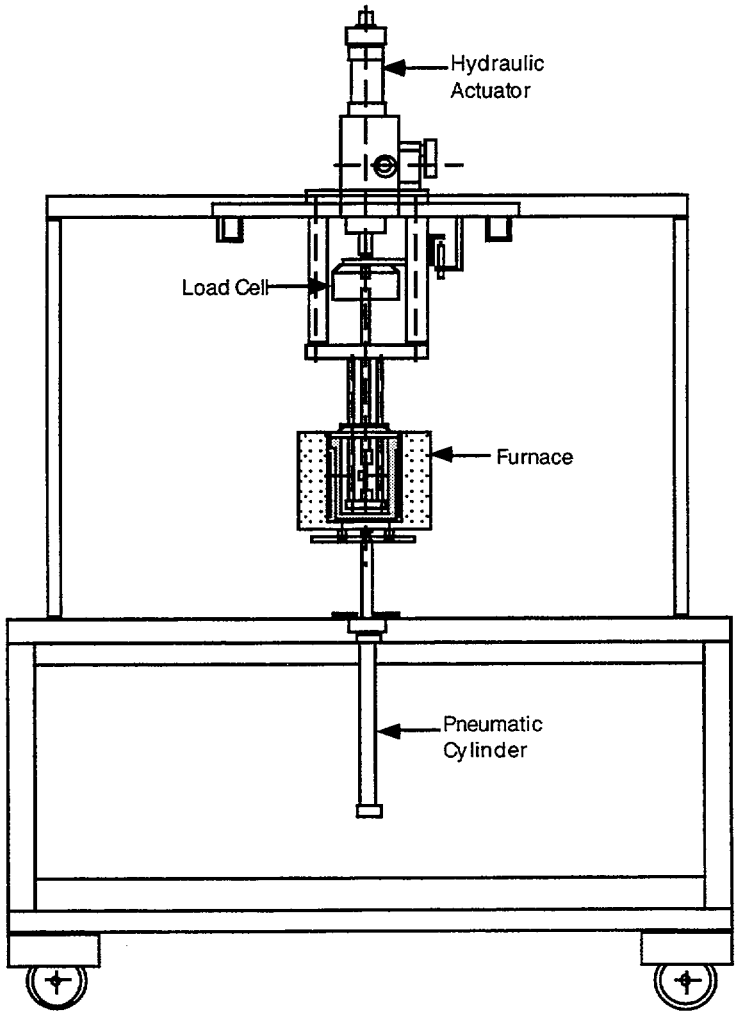

Figure 27. Schematic representation of hot–cell J–R test facility

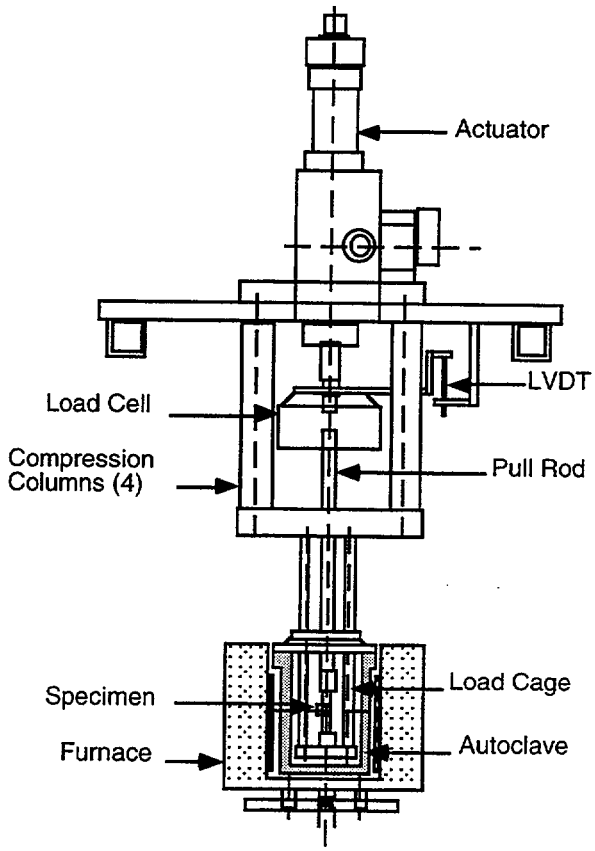

Figure 28. Schematic of the actuator, load cell, test train, autoclave, and furnace

An Instron Model 8500+ Dynamic Materials Testing System is used for the various mechanical tests. In general, the conventional dynamic testing systems that use a feedback signal for control are analog instruments, i.e., command, control, feedback, and transducer signals are all analog.

The recirculating water system consists of a storage tank, high pressure pump, regenerative heat exchanger, autoclave preheater, test autoclave, electrochemical potential (ECP) cell preheater, ECP cell, regenerative heat exchanger, Mity Mite^{TM} back-pressure regulator, an ion–exchange cartridge, a 0.2 micron filter, a demineralizer resin bed, another 0.2 micron filter, and return line to the tank. A schematic diagram of recirculating water system is shown in Fig. 29. Water is recirculated at low flow rates (≈10 ml/min.) at 200–320°C and pressures between 1200–1500 psig. For fatigue tests in low–DO simulated PWR environments, the ECP cell and the ion–exchange filter in the return line from the autoclave to the water supply tank are both bypassed during recirculation. The capacity of the Type 304 SS feedwater storage tank, manufactured by Filpaco Industries, is 30–gallon. The tank is designed for vacuum and over pressure to 60 psig. The cover gas of the storage tank is either nitrogen/oxygen or hydrogen to maintain a desired DO or hydrogen concentration in the water.

The LWR environments comprise high–purity deionized water that contains either up to 300 ppb DO or <10 ppb DO but with small additions of lithium and boron. The DO level in water is established by bubbling nitrogen that contains 1–2% oxygen through deionized water in a supply tank. The deionized water is prepared by passing purified water through a set of

filters that comprise a carbon filter, an Organex-Q filter, two ion exchangers, and a 0.2-mm capsule filter. Water samples are taken periodically to measure pH, resistivity, and DO concentration. Simulated PWR water is prepared by dissolving boric acid and lithium hydroxide in 20 L of deionized water before adding the solution to the supply tank. The DO in the deionized water is reduced to <0.01 ppm by bubbling nitrogen through the water. A vacuum is drawn on the tank cover gas to speed deoxygenation.

1. COVER GAS SUPPLY TANK
2. HIGH-PRESSURE REGULATOR WITH FLASH ARRESTOR
3. LOW-PRESSURE REGULATOR
4. FLOW METER
5. GAS PURIFIER
6. PRESSURE GAUGE
7. PRESSURE RELIEF VALVE
8. VENT TO AIR WITH FLASH ARRESTOR
9. FEEDWATER STORAGE TANK
10. SPARGE TUBE
11. FEEDWATER FILL PORT
12. WATER SAMPLE PORT
13. SOLENOID VALVE
14. 0.2-MICRON FILTER
15. HIGH-PRESSURE PUMP
16. CHECK VALVE
17. RUPTURE DISK
18. HEAT EXCHANGER
19. SYSTEM BLEED PORT
20. HIGH-PRESSURE GAUGE
21. AUTOCLAVE PREHEATER
22. PARR AUTOCLAVE
23. THERMOCOUPLE WELL
24. ECP CELL PREHEATER
25. ECP CELL
26. ECP CELL BYPASS LINE
27. BACK-PRESSURE RELIEF VAVLE
28. ION EXCHANGE CARTRIDGE
29. RECIRCULATING PUMP
30. DEMINERALIZER
31. DEMINERALIZER BYPASS LINE

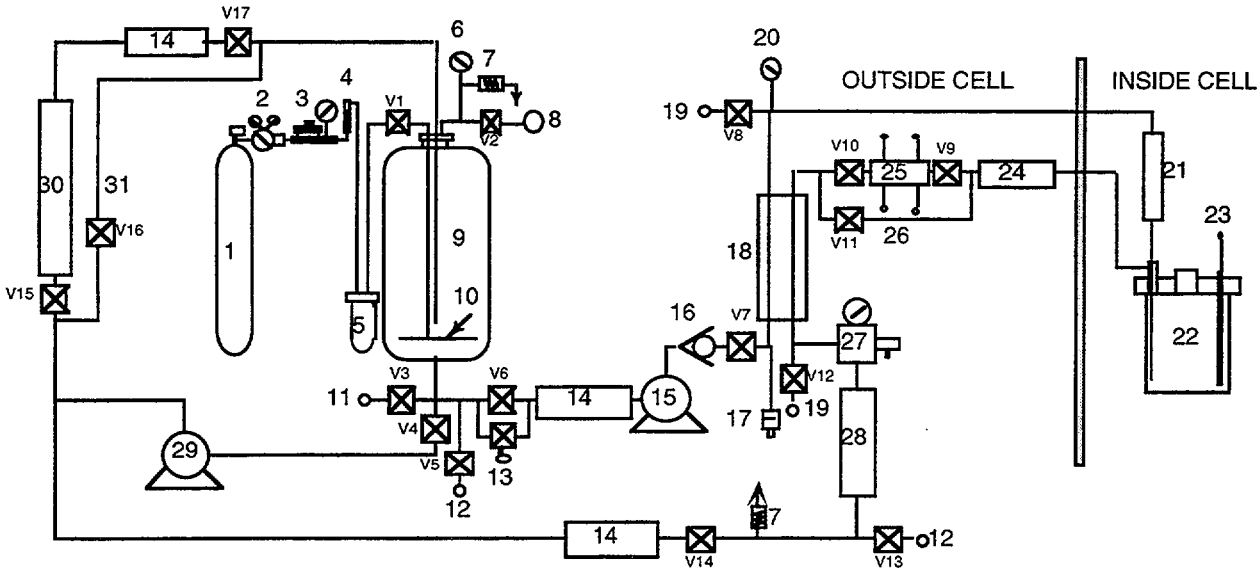

Figure 29. Schematic diagram of recirculating water system

3.5.3 Results

Fatigue crack growth tests were conducted on 1/4-T CT specimens of two heats of thermally aged CF8M cast SS (Heats 4331 and 75 with ≈23 and 28% ferrite, respectively) in high-purity water with 160-390 ppb DO, load ratio $R \approx 0.7$, initial $\Delta K \approx 8.0$ MPa $m^{1/2}$, and rise times between 60 and 5000 s. Crack extensions were monitored by the DC potential method. The composition and ferrite content of the two heats of cast SS are given in Table 8. Before testing, Heat 75 was thermally aged for 10,000 h at 400°C, and Heat 4331, for 700 h at 400°C. The crack growth results for the heats are given in Tables 9 and 10, and the crack-length-vs.-time plots are shown in Figs. 30 and 31.

Table 8. Composition of Heats 75 and 4331 of cast stainless steel

Heat	Composition (wt.%)									Ferrite
	Mn	Si	P	S	Mo	Cr	Ni	N	C	%
75	0.53	0.67	0.022	0.012	2.58	20.86	9.12	0.052	0.065	27.8
4331	0.76	1.17	–	–	2.58	20.75	10.05	0.040	0.044	23.1

Table 9. Crack growth results for Heat 4331 of CF8M cast SS[a] in high–purity water at 289°C

Phase No.	Test Time, h	O_2[b] Conc. ppb	Cond.[c] at 25°C, µS/cm	pH at 25°C	Potential mV(SHE) at 289°C SS	Potential mV(SHE) at 289°C Pt	Load Ratio	Rise Time s	K_{max},[d] MPa·m$^{1/2}$	ΔK, MPa·m$^{1/2}$	Growth Rate, m/s
0	0	–	–	–	–	–	0.70	–	26.94	8.08	–
1a	80	164	–	–	93	60	0.71	60	26.31	7.68	–
1b	120	222	–	–	84	102	0.71	60	27.10	7.91	5.23E-10
1c	230	290	–	–	93	125	0.71	60	28.67	8.37	7.56E-10
1d	275	320	–	–	100	140	0.71	60	29.87	8.72	1.03E-09
1e	310	328	–	–	105	149	0.70	60	31.00	9.21	1.21E-09
2a	365	380	0.10	–	100	153	0.70	300	31.71	9.42	4.11E-10
2b	403	366	0.10	–	105	160	0.70	300	32.20	9.56	3.95E-10
2c	502	396	0.10	–	124	174	0.70	300	33.66	10.00	4.70E-10
3	638	410	0.07	–	140	190	0.70	1000	34.76	10.43	2,50E-10
4	1008	440	0.07	–	175	204	0.70	5000	35.91	10.77	8.85E-10

[a]Compact tension Specimen Y4–09 of CF8M steel Heat 4331, aged for 700 h at 400°C.
[b]Effluent dissolved oxygen concentration was determined with an Orbisphere DO monitor.
[c]Represents feedwater conductivity.
[d]Stress intensity, K_{max}, values at the end of the time period.

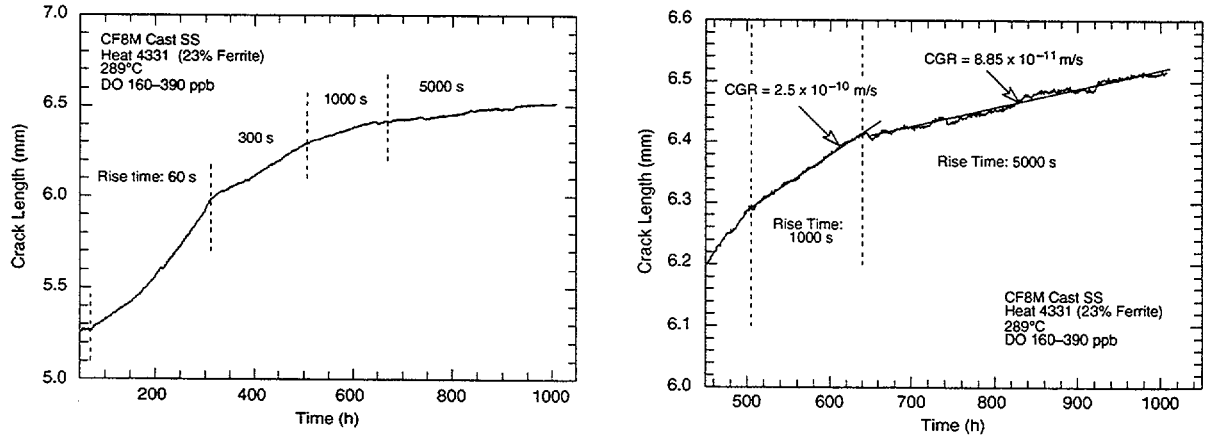

Figure 30. Crack–length–vs.–time plot for Specimen Y4–09 of thermally aged Heat 4331 in high–purity water at 289°C

Table 10. Crack growth results for Heat 75 of CF8M cast SS[a] in high–purity water at 289°C

Phase No.	Test Time, h	O_2[b] Conc. ppb	Cond.[c] at 25°C, µS/cm	pH at 25°C	Potential mV(SHE) at 289°C SS	Potential mV(SHE) at 289°C Pt	Load Ratio	Rise Time s	K_{max},[d] MPa·m$^{1/2}$	ΔK, MPa·m$^{1/2}$	Growth Rate, m/s
0	2	380	0.23		163	164	0.71	–	25.62	7.51	
1	27	380	0.23		163	164	0.71	60	26.68	7.80	1.57E-09
2	41	380	0.23		165	164	0.71	60	27.77	8.11	2.80E-09
3	50	380	0.23		168	164	0.71	60	28.97	8.44	4.00E-09
4	58	380	0.23		168	164	0.71	60	30.31	8.81	5.79E-09
5	63	380	0.23		168	166	0.71	60	31.62	9.18	7.55E-09
6	68	380	0.23		168	166	0.71	60	33.18	9.63	8.30E-09
7	74	370	0.23		170	168	0.71	60	35.69	10.33	8.57E-09
8	83	370	0.23		170	170	0.71	60	39.74	11.45	1.04E-08
9	110	350	0.23		176	172	1.00	–	26.93	0.00	7.10E-11
10	144	350	0.23		176	172	1.00	–	27.29	0.00	2.97E-10
11	192	350	0.23		176	166	0.70	60	24.95	7.51	8.41E-09
12	238	380	0.23	6.9	182	179	0.70	1000	26.33	7.92	5.97E-10
13	260	400	0.23		190	194	0.70	5000	21.67	6.59	1.11E-10
14	300	500	0.23		190	194	0.70	5000	21.71	6.60	4.22E-11
15	385	500	0.23		192	199	0.70	5000	21.76	6.62	1.22E-11
16	455	–	–		180	207	0.70	1000	25.55	7.71	9.90E-11
17	475	–	–		–	–	0.70	1000	25.96	7.84	5.47E-10
18	500	600	0.13		202	214	0.70	1000	26.82	8.10	8.72E-10

[a]Compact tension Specimen 75–09T of CF8M steel Heat 75, aged for 10,000 h at 400°C.
[b]Effluent dissolved oxygen concentration was determined with an Orbisphere DO monitor.
[c]Represents feedwater conductivity.
[d]Stress intensity, K_{max}, values at the end of the time period.

The final crack size was marked by fatigue cycling at room temperature. The specimens were then fractured and the initial (i.e., fatigue precrack) and final (test) crack lengths of both halves of the fractured specimen were measured optically. The crack lengths were determined by the 9/8 averaging technique, i.e., the two near–surface measurements were averaged and the resultant value was averaged with the remaining seven measurements. The optically measured crack lengths showed excellent agreement with the values determined by the DC potential method. The precrack and final crack lengths measured optically and those determined by DC potential method were 5.01 and 6.40 mm, and 5.04 and 6.40 mm, respectively, for Specimen Y4–09, and 6.34 and 8.16 mm, and 6.31 and 8.24 mm, respectively, for Specimen 75–09T.

The results indicate that for a 1/4-T CT specimen, K_{max} increases rapidly with crack growth, e.g., for Specimen 75-09, K_{max} increased from ≈27 to 40 MPa·m$^{1/2}$ when the crack length increased from ≈6.5 to 7.6 mm (Phases 1–8, Table 10). A similar increase in K_{max} was observed for Specimen Y4–09 (Phases 1a–1e, Table 9). The applied load, therefore, should be decreased (load shedding) during the test to prevent a large increase in K_{max} and to maintain approximately the same loading conditions at the crack tip. The effect of load shedding on CGRs was examined for Specimen 75–09. At the end of Phase 12, K_{max} was changed from ≈26 to 22 MPa·m$^{1/2}$ (a decrease of ≈18%) and the rise time was increased from 1000 to 5000 s while all other conditions remained the same. Because of the change in rise time, the CGR

decreased immediately, as expected, by a factor of ≈5. However, during the next ≈130 h (i.e., during Phases 13–15), the CGRs decreased further by nearly an order of magnitude. The results suggest that the reduction in maximum load of ≈18% is too large. Future tests that employ step shedding of load will follow the guidelines of ASTM E647, i.e., the reduction in maximum load of adjacent load steps will not exceed 10% of the previous value of maximum load.

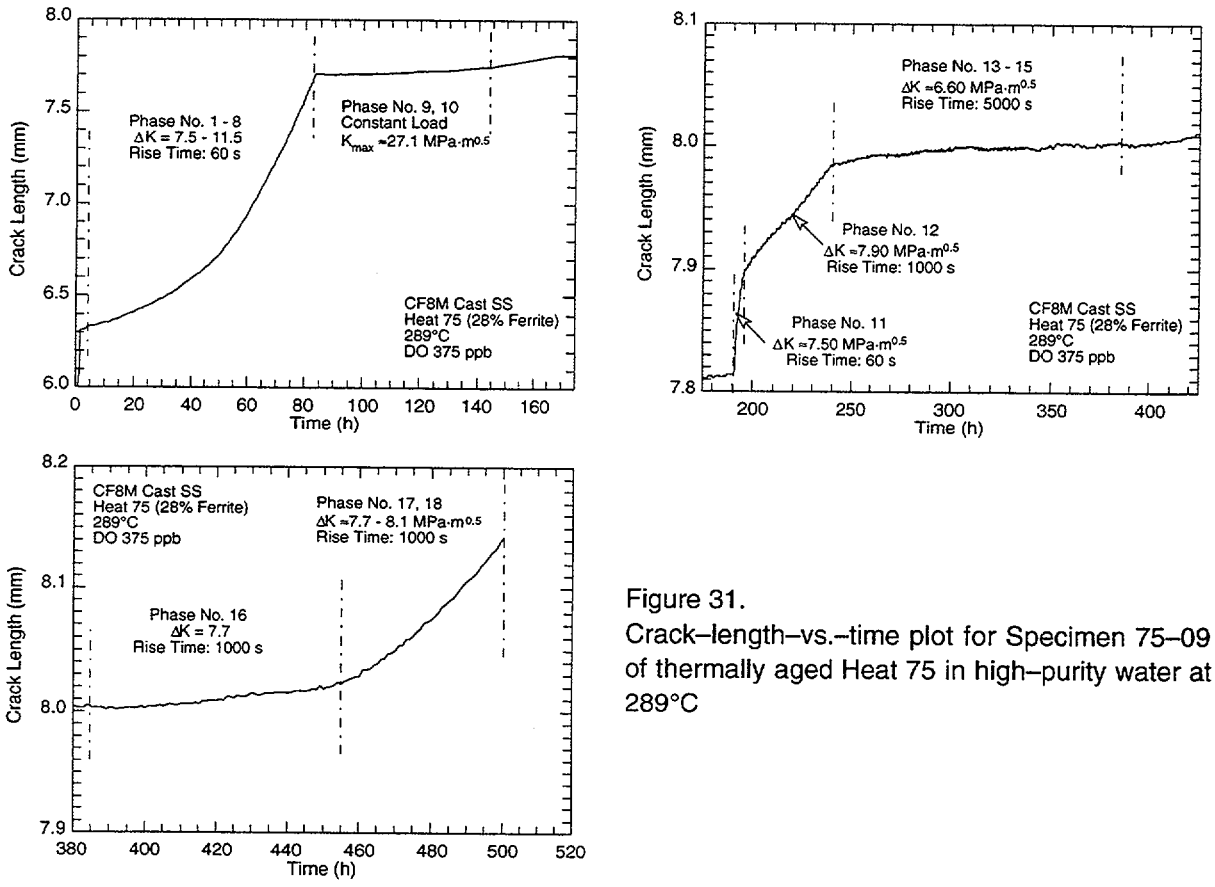

Figure 31.
Crack–length–vs.–time plot for Specimen 75–09 of thermally aged Heat 75 in high–purity water at 289°C

The experimental CGRs for CF–8M cast SS in water and those predicted in air for wrought SSs for the same loading conditions are plotted in Fig. 32. The results obtained earlier on 1–T CT specimens of thermally aged Heat 75 are also included in the figure. The CGRs for 1/4–T CT specimens of Heat 4331 show good agreement with the results obtained on 1–T CT specimens of Heat 75 in ≈0.3 ppm DO water; the CGRs for 1/4–T CT specimens of Heat 75 (shown as triangles in Fig. 32) are a factor of 3–6 greater. The high growth rates for small specimens of Heat 75 may be related to water chemistry. The feedwater conductivity during the test was higher than is normally maintained in our tests; the nature of the impurities (sulfate, phosphate, etc.) is unknown.

The results also indicate significant SCC of cast CF-8M SS in high–DO water at 289°C, e.g., during Phases 9 and 10 at constant load, CGR varied between $\approx 7 \times 10^{-11}$ and 3×10^{-10} m/s at a K_{max} of ≈27 MPa·m$^{1/2}$. These values are in good agreement with the data obtained on wrought SSs in high–DO water.

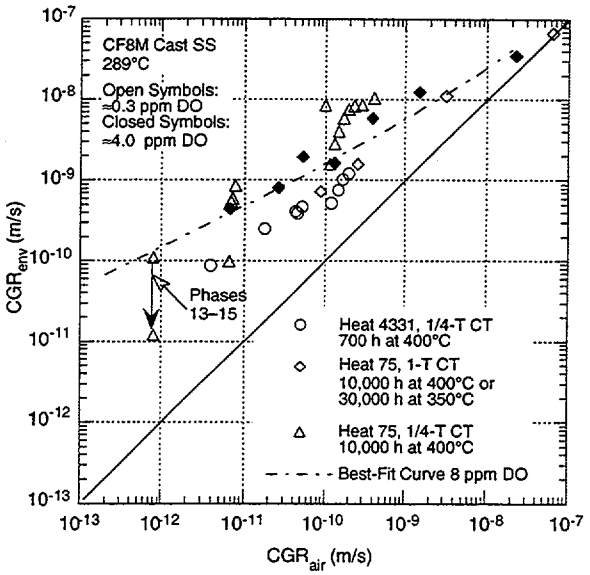

Figure 32.
Corrosion fatigue data for thermally aged CF–8M cast stainless steel in high–purity water at 289°C

4 Environmentally Assisted Cracking of Alloys 600 and 690 in Simulated LWR Water (W. K. Soppet, O. K. Chopra, and W. J. Shack)

The objective of this work is to evaluate the resistance of Alloys 600 and 690 to EAC in simulated LWR coolant environments. High-nickel alloys have experienced general corrosion (tube wall thinning), localized intergranular attack (IGA), and SCC in LWRs. Secondary-side IGA* and axial and circumferential SCC** have occurred in Alloy 600 tubes at tube support plates in many steam generators. Primary-water SCC of Alloy 600 steam generator tubes in PWRs at roll transitions and U-bends and in tube plugs*** is a widespread problem that has been studied intensively. Cracking has also occurred in Alloy 600 and other high-nickel alloys (e.g., Inconel-82 and -182 and Alloy X750) that are used in applications such as instrument nozzles and heater thermal sleeves in the pressurizer† and the penetrations for control-rod drive mechanisms in reactor vessel closure heads in the primary system of PWRs;†† in dissimilar-metal welds between SS piping and LAS nozzles and in jet pump hold-down beams;††† and in shroud-support-access-hole covers§ in BWRs. Alloy 690, with a higher chromium content and greater resistance to SCC, has been proposed as an alternate to Alloy 600.

Alloys 600 and 690, in general, undergo differing thermomechanical processing for applications other than steam generator tubes. Because environmental degradation of the alloys in many cases is very sensitive to processing, further evaluation of SCC is needed. In addition, experience strongly suggests that materials that are susceptible to SCC are also susceptible to environmental degradation of fatigue life and fatigue-crack growth properties. A program is being conducted at ANL to evaluate the resistance of Alloys 600 and 690 and their welds to EAC in simulated LWR coolant environments. Fracture mechanics CGR tests are being conducted on CT specimens of Alloys 600 and 690 in oxygenated and deaerated water that contains boron, lithium, and low concentrations of dissolved hydrogen at 289-380°C. The experimental details and results from this study are presented elsewhere.[103-107]

---

* USNRC Information Notice No. 91-67, "Problems with the Reliable Detection of Intergranular Attack (IGA) of Steam Generator Tubing," Oct. 1991.

** USNRC Information Notice No. 90-49, "Stress Corrosion Cracking in PWR Steam Generator Tubes," Aug. 1990; Notice No. 91-43, "Recent Incidents Involving Rapid Increases in Primary-to-Secondary Leak Rate," July 1991; Notice No. 92-80, "Operation with Steam Generator Tubes Seriously Degraded," Dec. 1992; Notice No. 94-05, "Potential Failure of Steam Generator Tubes with Kinetically Welded Sleeves," Jan. 1994.

*** USNRC Information Notice No. 89-33, "Potential Failure of Westinghouse Steam Generator Tube Mechanical Plugs," March 1989; Notice No. 89-65, "Potential for Stress Corrosion Cracking in Steam Generator Tube Plugs Supplied by Babcock and Wilcox," Sept. 1989; Notice No. 94-87, "Unanticipated Crack in a Particular Heat of Alloy 600 Used for Westinghouse Mechanical Plugs for Steam Generator Tubes," Dec. 1994.

† USNRC Information Notice No. 90-10, "Primary Water Stress Corrosion Cracking (PWSCC) of Inconel 600," Feb. 1990.

†† USNRC Generic Letter 97-01: "Degradation of Control Rod Drive Mechanism and Other Vessel Closure Head Penetrations," Apr. 1, 1997; USNRC Information Notice No. 96-11, "Ingress of Demineralizer Resins Increases Potential for Stress Corrosion Cracking of Control Rod Drive Mechanism Penetrations," Feb. 1996; INPO Document SER 20-93 "Intergranular Stress Corrosion Cracking of Control Rod Drive Mechanism Penetrations," Sept. 1993.

††† USNRC Information Notice 93-101, "Jet Pump Hold-Down Beam Failure," Dec. 1993.

§ USNRC Information Notice 92-57, "Radial Cracking of Shroud Support Access Hole Cover Welds," Aug. 1992.

The existing CGR data obtained at ANL and elsewhere for Alloys 600 and 690 under cyclic loading conditions have been compiled and evaluated to establish the effects of alloy type, temperature, load ratio R, stress intensity K, and DO level. The experimental CGRs have been compared with CGRs that would be expected in air under the same mechanical loading conditions to obtain a qualitative understanding of the degree and range of conditions that are necessary for significant environmental enhancement of growth rates.

For austenitic SSs, temperature, stress ratio R, and cyclic frequency have a significant effect on CGRs.[108] Growth rates can be represented by

$$da/dN = C(T)\, F(f)\, S(R)\, (\Delta K)^n, \tag{17}$$

where the functions C, F, and S express the dependence of temperature, frequency, and stress ratio, and n is the exponent for the power–law dependence of growth rates on the stress intensity factor range ΔK. The existing fatigue CGR data on Alloys 600 and 690 were analyzed by using Eq. 17 to establish the effects of temperature, stress ratio R, cyclic frequency, and stress intensity factor range ΔK on the CGRs in air.[107] The CGR (m/cycle) of Alloy 600 in air is expressed as

$$da/dN = C_{A600}\, (1 - 0.82\, R)^{-2.2}\, (\Delta K)^{4.1}, \tag{18}$$

where ΔK is in $MPa \cdot m^{1/2}$, and the constant C_{A600} is given by a third-order polynomial of temperature T (°C) expressed as

$$C_{A600} = 4.835 \times 10^{-14} + (1.622 \times 10^{-16})T - (1.490 \times 10^{-18})T^2 + (4.355 \times 10^{-21})T^3. \tag{19}$$

The CGR (m/cycle) of Alloy 690 in air is expressed as

$$da/dN = C_{A690}\, (1 - 0.82\, R)^{-2.2}\, (\Delta K)^{4.1}, \tag{20}$$

where ΔK is in $MPa \cdot m^{1/2}$ and constant C_{A690} is given by a third-order polynomial of temperature T (°C) expressed as

$$C_{A690} = 5.423 \times 10^{-14} + (1.83 \times 10^{-16})T - (1.725 \times 10^{-18})T^2 + (5.490 \times 10^{-21})T^3. \tag{21}$$

For both alloys, the estimated values show good agreement with the experimental results. Under similar loading conditions, the CGRs of Alloy 690 appear to be slightly higher than those of Alloy 600. This difference most likely is an artifact of a smaller database for Alloy 690.

4.1 Fatigue Crack Growth in LWR Environments

4.1.1 Alloy 600

Fatigue crack growth experiments have been performed on Alloy 600 to determine the effects of temperature, load ratio, stress intensity, material heat treatment, and water chemistry on CGR. The existing database[103–117] consists of results of ≈800 tests on several heats of Alloy 600 under various heat treatment conditions. The tests were conducted in high–purity water at temperatures between 240 and 325°C; ≈600 tests have been conducted at 289°C. The loading conditions include load ratio R = 0.05–0.95, maximum stress intensity

K_{max} = 10–96 MPa·m$^{1/2}$, stress intensity factor range ΔK = 1.4–79 MPa·m$^{1/2}$, and rise time t_r = 0.05–800 s. To obtain a qualitative understanding of the degree of enhancement and the range of conditions over which significant environmental enhancement is observed, it is helpful to plot the observed CGRs against the CGRs that would be expected in air under the same loading conditions, i.e., the same ΔK, R, and t_r.

The experimental CGRs in high–DO (≥300 ppb DO) water and those predicted by Eqs. 18 and 19 for the same mechanical loading conditions are plotted in Fig. 33.[103,104,115,117] The significant results and influence of critical parameters on CGRs in high–DO water are summarized below.

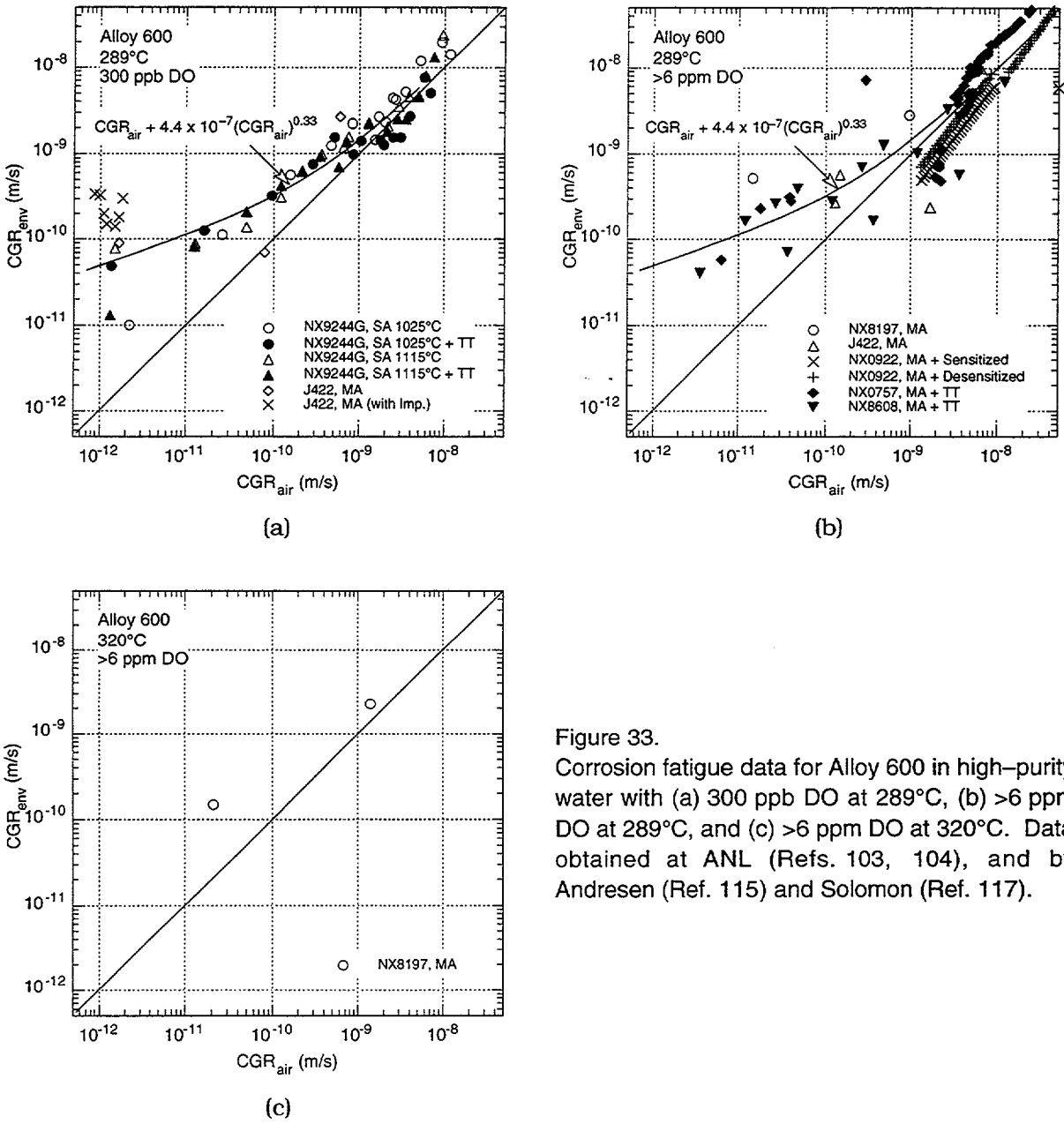

Figure 33.
Corrosion fatigue data for Alloy 600 in high–purity water with (a) 300 ppb DO at 289°C, (b) >6 ppm DO at 289°C, and (c) >6 ppm DO at 320°C. Data obtained at ANL (Refs. 103, 104), and by Andresen (Ref. 115) and Solomon (Ref. 117).

Water Chemistry: The fatigue CGRs of Alloy 600 are enhanced in high–DO water; see Fig. 33. Growth rates increase slightly when DO level is increased from 300 to 6000 ppb or when 15–100 ppb sulfates are added to the water.[103]

Material Condition: The environmental enhancement of growth rates does not appear to depend on either the carbon content or heat treatment of the material. For example, the CGRs of a low–carbon heat (NX9244G) are comparable to those of high–carbon heats (e.g., NX8197, NX8844J). The high–carbon heats contain continuous (NX8197) or semicontinuous (NX8844J, J422) carbide precipitation at the grain boundaries whereas, because of the low carbon content (≈0.03%) and relatively high solution–annealing temperatures (1025 or 1115°C), Heat NX9244G does not contain intergranular carbides.[104] Also, thermal treatment for 24 h at 600°C has no effect on the CGRs in high–DO water; the growth rates of solution–annealed Heat NX9244G are approximately the same with or without thermal treatment; see Fig. 33a.[104]

Mechanical Loading: The results indicate that the effects of environment on growth rates in high–DO water are greater under loading conditions that correspond to $<1 \times 10^{-9}$ m/s CGRs in air; under certain loading conditions, the CGRs in high–DO water may be enhanced by nearly two orders of magnitude.

Temperature: Limited data suggest that in high–DO water, the growth rates at 320°C are comparable to those at 289°C. However, nearly all of the fatigue crack growth data on Alloy 600 have been obtained at 289°C, and additional tests at 320°C are needed to verify the temperature dependence of growth rates in high–DO water.

The experimental CGRs in simulated PWR or low–DO (<10 ppb DO) water and those predicted by Eqs. 18 and 19 for the same mechanical loading conditions are plotted in Figs. 34 a–c. In contrast to the behavior in high–DO water, where the CGRs of Alloy 600 are enhanced under nearly all material and loading conditions that have been investigated, only some conditions appear to enhance fatigue CGRs in low–DO water, Fig. 34.[103,104,109,111] The significant results and influence of critical parameters on CGRs in simulated PWR water are summarized below.

Material Condition: The material yield strength and microstructure, such as grain boundary carbide distribution, and temperature appear to be important parameters that influence environmental enhancement of CGRs. In low–DO water, environmental enhancement of CGRs is observed for the solution–annealed (at 1025°C) low–carbon Heat NX9244G tested at 320°C, and for the mill–annealed high–carbon Heat J422 tested at 289°C, Figs. 34a and b. However, the low–carbon Heat NX9244G, when solution annealed at 1115°C and tested under the same loading conditions, shows no effect of environment on growth rates, Fig. 34a. The two solution treatments exhibit similar grain boundary carbide distribution but the material that was solution annealed at 1025°C exhibits higher yield strength than that annealed at 1115°C.[104] Materials with poor grain boundary coverage of carbides and high yield strength are known to exhibit high susceptibility to SCC in low–DO PWR environments.[118,119] At 289°C, not all high–carbon heats show environmental enhancement of CGRs; Heats NX8197 and NX8844J show no effect of environment on growth rates. The enhanced growth rates of Heat J422 may be attributed to the yield strength of the material, which is higher than that of Heats NX8197 or NX8844J.[104]

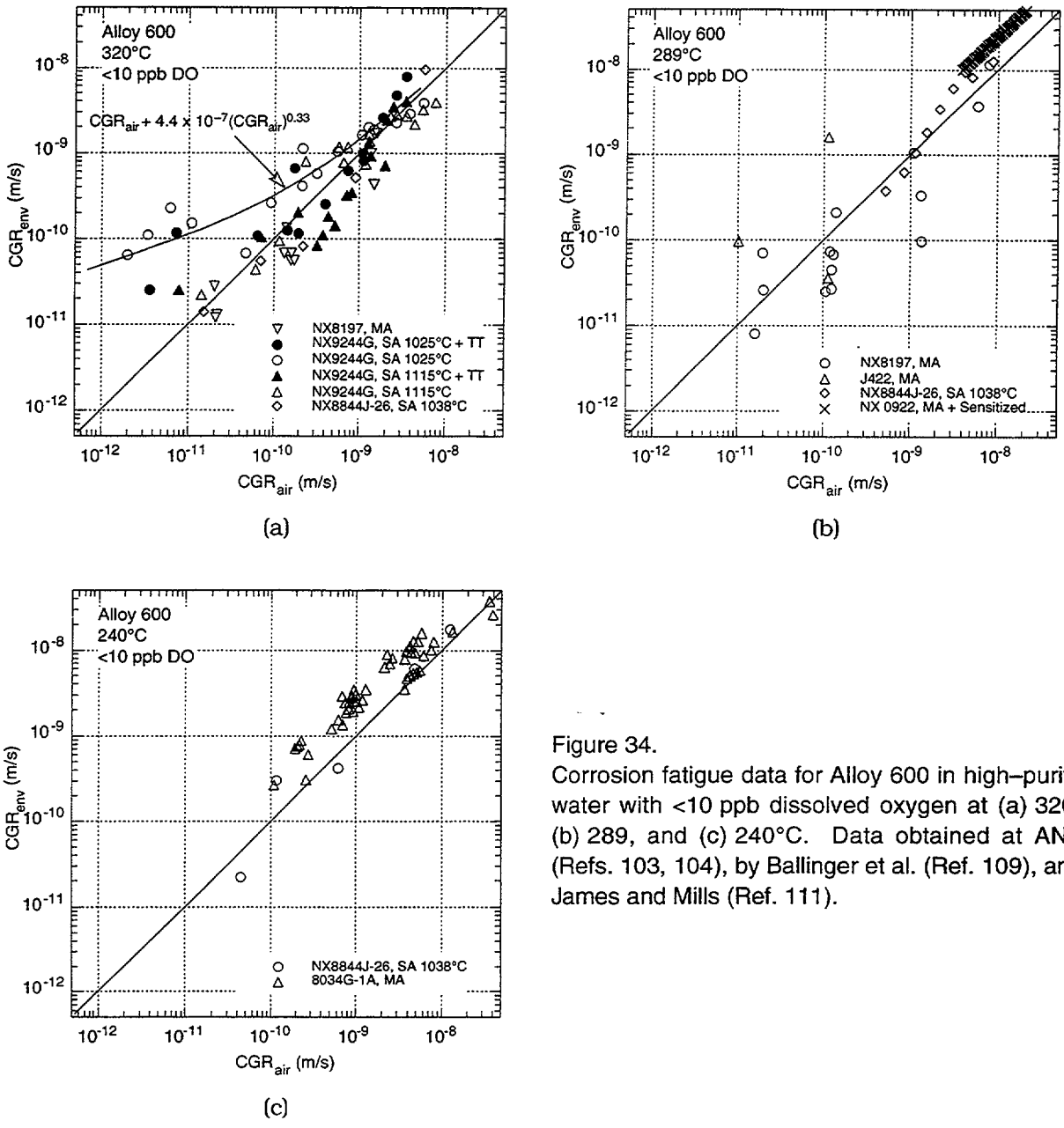

Figure 34.
Corrosion fatigue data for Alloy 600 in high–purity water with <10 ppb dissolved oxygen at (a) 320, (b) 289, and (c) 240°C. Data obtained at ANL (Refs. 103, 104), by Ballinger et al. (Ref. 109), and James and Mills (Ref. 111).

Temperature: The fatigue CGR data in Fig. 34 suggest that environmental enhancement of CGR is greater at higher temperature. However, the existing data are inadequate to determine the effect of temperature on the fatigue CGR of Alloy 600 in low–DO water. For example, tests on susceptible heats of material have either not been conducted at low temperatures or the mechanical loading conditions are such that the contributions of environmental effects are moderate. At ≈240°C, all of the tests have been conducted under loading conditions that correspond to growth rates >1 x 10^{-10} m/s in air.[104,111] For these conditions, the growth rates of mill–annealed Heat 8034G are enhanced by a factor of ≈2 in low–DO water.[111]

Dissolved Hydrogen: The dissolved hydrogen in water can influence the corrosion product films on nickel alloys, and thereby play a role in the crack growth process. A decrease in the bulk

hydrogen content of water leads to an increase in the corrosion potential of the material and thus to increased oxidation of the material and higher CGRs. The effects of dissolved hydrogen in low–DO water on CGRs of Alloy 600 have been investigated.[103,120] Studies on hot–worked and mill–annealed Alloy 600 tested in simulated PWR water[120] indicate that the CGRs increase by a factor of 1.5 when dissolved hydrogen in water is decreased from 25 to 0 cm^3/kg of water. Similar results have also been observed in mill–annealed Alloy 600 (Heat NX8197) tested in simulated PWR water;[103] CGRs increase when dissolved hydrogen is decreased from 58 to 3 cm^3/kg of water, Fig. 35. However, the significance of these results on enhanced CGRs in PWR environments is not clear; the results for Heat NX8197, shown in Fig. 34, show little or no effect of environment on CGRs at both 289 and 320°C.

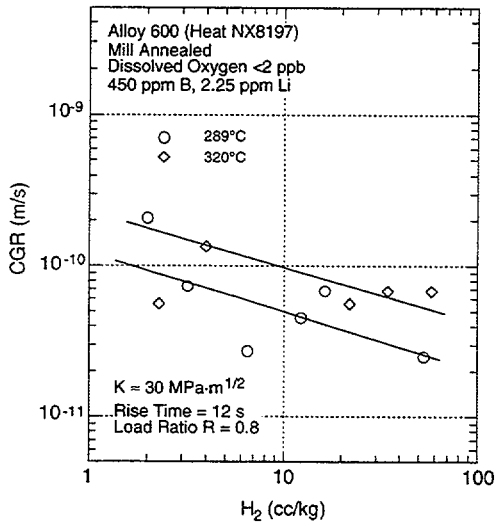

Figure 35.
Dependence of CGRs of Alloy 600 at 289 and 320°C on concentration of dissolved hydrogen in simulated PWR water at load ratio of 0.8. Data obtained at ANL (Ref. 103).

Mechanical Loading. In PWR environments, high load ratios, e.g., 0.75 or higher, and low frequencies produce intergranular cracking, and low load ratios, e.g., 0.5 and lower, and high frequencies produce transgranular cracking.[120] The differing fracture morphology has been explained on the basis of the thermodynamic conditions at the crack tip, i.e., intergranular cracking is enhanced when the crack tip environment contains steam hydrogen bubbles.

The existing fatigue crack growth data have been analyzed to develop correlations for estimating the enhancement of CGRs in LWR environments relative to the CGRs in air. Ford and Andresen[121,122] argue that there are fundamental reasons to expect that in LWR environments, the CGRs of austenitic SSs and nickel alloys should be of the form

$$CGR_{env} = CGR_{air} + A(\dot{\varepsilon}_{CT})^m, \quad (22)$$

where CGR_{env} is the CGR in the environment, CGR_{air} is the CGR in air (a relatively inert environment), and $\dot{\varepsilon}_{CT}$ is the crack tip strain rate. Parameters A and m depend on the material and the environment. Shoji[123] has argued that under cyclic loading, $\dot{\varepsilon}_{CT}$ is proportional to CGR_{air}. In this case, Eq. 22 can be written as

$$CGR_{env} = CGR_{air} + A(CGR_{air})^m, \quad (23)$$

which is a form convenient for comparisons with experimental data and which has been widely used to correlate CGR data. Fitting the fatigue crack growth data on Alloy 600 in high–purity water with ≈300 ppb DO to Eq. 23 by minimizing the least–squares error between the experimental and predicted CGRs gives the values of 4.4×10^{-7} and 0.33 for A and m, respectively.[105] The CGRs in the environment estimated from Eq. 23 and the best–fit values of constants A and m are plotted in Fig. 33. The same correlation may also be used to represent environmental enhancement of CGRs of the susceptible heats of Alloy 600 in low–DO water.

4.1.2 Alloy 690

The existing fatigue crack growth data on Alloy 690 in high–purity high–temperature water are very limited. The existing database[103–106] consists of data from ≈110 tests on three heats of Alloy 690, tested in high–purity water at temperatures between 240 and 320°C; only 15 of these have been conducted in high–DO water, the remainder were conducted in either simulated PWR or <10 ppb DO water. The loading conditions include K_{max} = 30–64 MPa·m$^{1/2}$, R = 0.2–0.9, ΔK = 3–32 MPa·m$^{1/2}$, and a 12–s rise time. To obtain a qualitative understanding of the degree of enhancement and the range of conditions over which significant environmental enhancement is observed, in Figs. 36 and 37, respectively, we plotted the experimental CGRs against those predicted by Eqs. 20 and 21 for the same mechanical loading conditions for high–DO (≥300 ppb DO) water and simulated PWR or low–DO (<10 ppb DO) water.

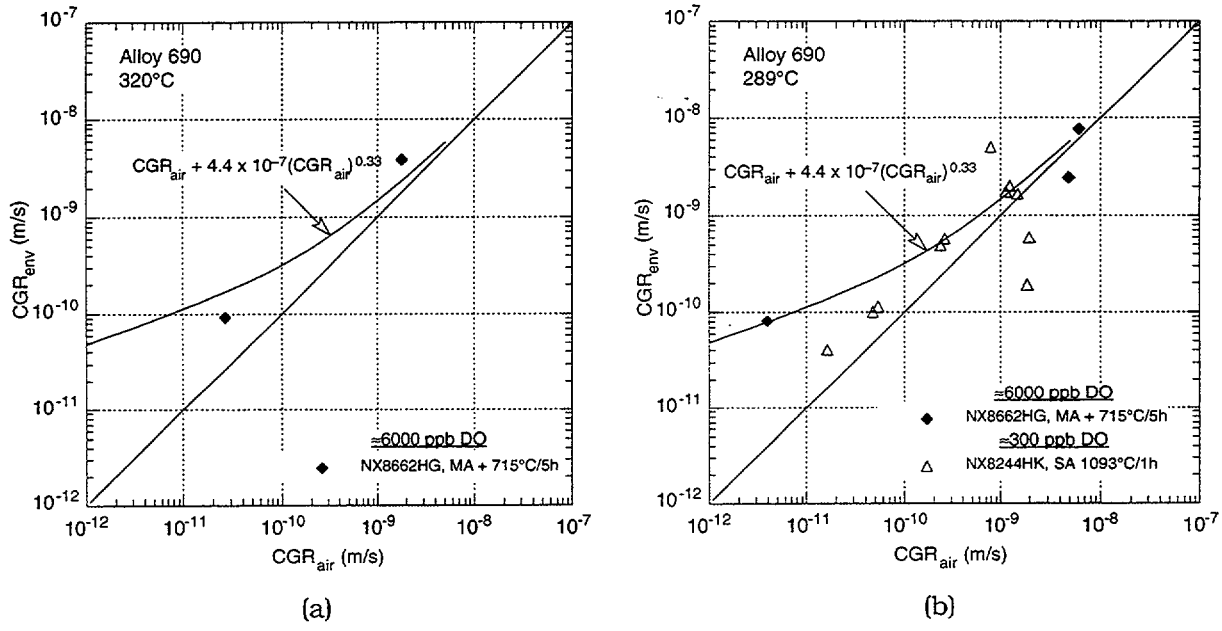

Figure 36. Corrosion fatigue data for Alloy 690 in high–purity water with ≈6000 or 300 ppb dissolved oxygen at (a) 320 and (b) 289°C. Data obtained at ANL (Refs. 103–106).

Limited data indicate some enhancement of growth rates in high–DO (300 ppb or higher) water, Fig. 36. Results in high–DO water are bounded by the CGRs estimated from Eq. 23 for Alloy 600 in high–DO water. The results at 240–320°C indicate no environmental effects on the CGRs of Alloy 690 in low–DO (<10 ppb DO) water under the investigated material and loading conditions, Fig. 37. However, the existing database for Alloy 690 is small and additional tests are needed to verify these results.

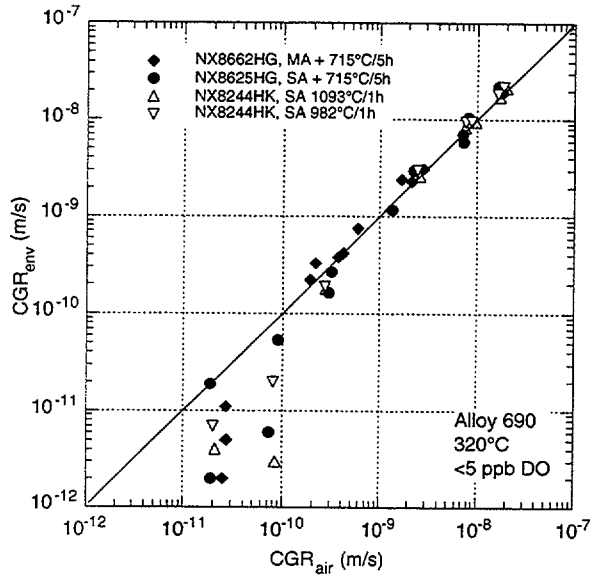

(a)

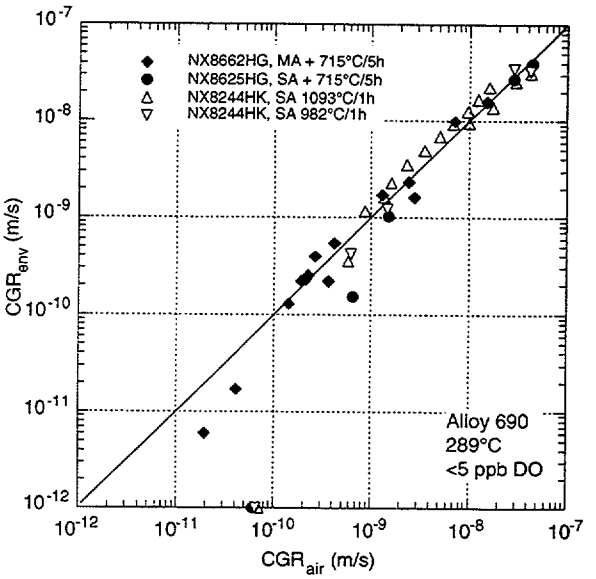

(b)

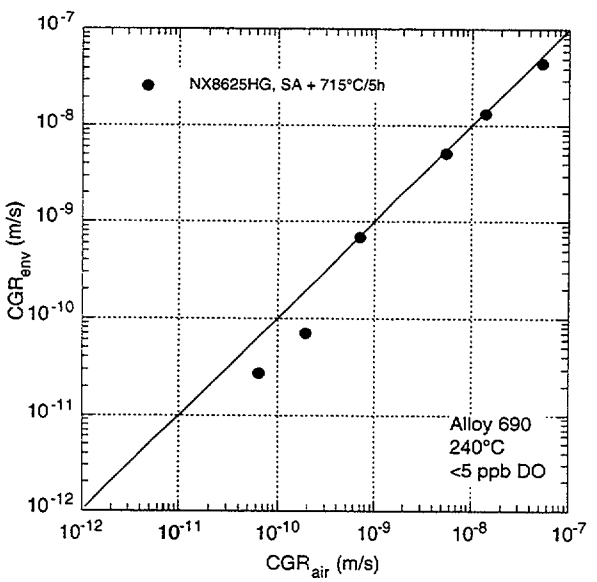

(c)

Figure 37.
Corrosion fatigue data for Alloy 690 in high–purity water with <10 ppb dissolved oxygen at (a) 320, (b) 289, and (c) 240°C. Data obtained at ANL (Refs. 103–106).

5 Summary

5.1 Environmental Effects on Fatigue Strain–versus–Life (S–N) Behavior of Primary Pressure Boundary Materials

The influence of reactor environments on the mechanism of fatigue crack initiation in carbon and low–alloy steels is discussed. Decreased fatigue lives of these steels in high–DO water are caused primarily by the effects of environment on the growth of small cracks <100 μm deep. In LWR environments, the growth of small fatigue cracks in carbon and low–alloy steels occurs by a slip oxidation/dissolution process.

A fracture mechanics approach was used to predict the fatigue lives of carbon and low-alloy steels in air and LWR environments. The fatigue life is considered composed of the growth of microstructurally and mechanically small cracks. The growth of the former cracks is very sensitive to microstructure and is characterized by decelerating crack growth, that of the latter, which can be predicted by fracture mechanics methodology, is characterized by accelerating crack growth, and has been characterized in terms of the J–integral range ΔJ and CGR data in air and LWR environments. Fatigue lives estimated from the present model show good agreement with the experimental data for carbon and low–alloy steels in air and LWR environments. At low strain amplitudes, i.e., fatigue lives of $>10^4$ cycles, the predicted lives in water are slightly lower than those observed experimentally, most likely because of the effects of crack closure.

5.2 Irradiation–Assisted Stress Corrosion Cracking of Austenitic SS

In unirradiated state and at the relatively low fluence level of $\approx 0.3 \times 10^{21}$ n cm^{-2}, commercial and laboratory heats of Types 304, 304L, and 348 SS that contain relatively high concentrations of sulfur (>0.009 wt.% sulfur, 15-18.50 wt.% chromium) exhibited significant susceptibility to TGSCC, whereas alloys that contain a relatively low concentration of sulfur (<0.004 wt.%) exhibited good resistance to TGSCC At $\approx 0.9 \times 10^{21}$ n cm^{-2}, commercial heats of Types 304 and 316 SS that contain low concentrations of sulfur, exhibited good resistance to TGSCC and IGSCC and high levels of uniform and total elongation, whereas a commercial heat of Type 304 SS that contains a relatively high concentration of sulfur exhibited poor resistance to TGSCC and IGSCC and low levels of uniform and total elongation. These observations indicate that for commercial heats of Types 304 and 304L SS, a high concentration of sulfur (>0.009 wt.%) is significantly detrimental and a sufficiently low concentration of sulfur is a necessary condition to ensure good resistance to IASCC.

At $\approx 0.9 \times 10^{21}$ n cm^{-2}, a laboratory alloy that contains a high concentration of chromium (≈21 wt.%) exhibited excellent resistance to TGSCC and IGSCC in spite of high sulfur content (≈0.028 wt.%), whereas heats with <17.5 wt.% chromium exhibited significant susceptibility to TGSCC plus IGSCC. This finding indicates that chromium atoms in high concentration, and low ferrite content of <3 volume % play a beneficial role in suppressing susceptibility to IASCC under BWR conditions.

Twenty eight CT and 32 SSRT specimens were fabricated, QA-inspected, cleaned, and shipped to the Halden Reactor to initiate the Phase-II Irradiation Experiment. The primary objectives of the Phase II Irradiation Experiment are to determine: stress corrosion and crack

growth behavior of core shroud welds, effects of postwelding annealing at 500 and 600°C on crack growth behavior of core shroud welds, effects of grain-boundary optimization on IASCC behavior of Types 304, 304L, 316 SS and Alloy 690, and effects of oxygen, molybdenum, titanium, and delta ferrite.

The HAZ of BWR core shroud welds are contaminated with significant amounts of calcium, oxygen, and fluorine. These low-solubility impurities tend to concentrate on or near the grain boundaries of HAZs in core shroud welds, during either welding, in-reactor service, or both. Unusual microcavity structures were observed in the HAZs of field-cracked Type 304 and 304L SS core shroud welds and unirradiated mockup welds fabricated by the SMA procedure. The microcavities are formed preferentially on or near grain boundaries of HAZs. It appears that segregation of the welding-related impurities calcium, oxygen, and fluorine produces a significantly modified composition at or near grain boundaries in the HAZ of a BWR core shroud weld, leading to a condition that is susceptible to the formation of microcavities and fluorine–catalyzed stress corrosion at or near grain boundaries under irradiation.

Fatigue crack growth tests have been conducted on 1/4–T CT specimens of two heats of cast SS in high–purity water at 289°C to establish the test procedure and conditions that will be used to perform crack growth tests on irradiated materials. Tests were performed in accordance with ASTM E647 "Standard Test Method for Measurement of Fatigue Crack Growth Rates." The CGRs from 1/4–T CT specimens show good agreement with the results obtained from 1–T CT specimens in ≈0.3 ppm DO water.

5.3 Environmentally Assisted Cracking of Alloys 600 and 690 in Simulated LWR Water

The resistance of Alloys 600 and 690 to EAC in simulated LWR environments has been evaluated. Existing CGR data for these materials under cyclic loads have been analyzed to establish the effects of alloy chemistry, material heat treatment, cold work, temperature, load ratio R, stress intensity K, and DO level. The experimental CGRs in high–temperature, high–purity water are compared with CGRs that would be expected in air under the same mechanical loading conditions to obtain a qualitative understanding of the degree and range of conditions that are necessary for significant environmental enhancement in growth rates. The fatigue CGRs of Alloy 600 are enhanced in high–DO water; the environmental enhancement of growth rates does not appear to depend on either the carbon content or heat treatment of the material. Also, in high–DO water, the CGRs at 320°C are comparable to those at 289°C. In contrast to the behavior in high–DO water, environmental enhancement of CGRs of Alloy 600 in low–DO water seems to depend on material conditions such as yield strength and grain boundary coverage of carbides. Material with high yield strength and/or low grain boundary coverage of carbides exhibit enhanced CGRs. Correlations have been developed for estimating the enhancement of CGRs of Alloy 600 in LWR environments relative to the CGRs in air under the same loading conditions.

For Alloy 690, the data suggest some enhancement of CGRs in high–DO water, i.e., ≈300 ppb DO. Limited data indicate no environmental effects on CGRs in low–DO water, i.e., water with <10 ppb DO. However, the existing database for Alloy 690 is small, and additional tests are needed to verify these results.

References

1. K. Kussmaul, R. Rintamaa, J. Jansky, M. Kemppainen, and K. Törrönen, *On the Mechanism of Environmental Cracking Introduced by Cyclic Thermal Loading*, in IAEA Specialists Meeting Corrosion and Stress Corrosion of Steel Pressure Boundary Components and Steam Turbines, VTT Symp. 43, Espoo, Finland, pp. 195–243 (1983).

2. K. Iida, *A Review of Fatigue Failures in LWR Plants in Japan*, Nucl. Eng. Des. **138**, pp. 297–312 (1992).

3. K. Kussmaul, D. Blind, and J. Jansky, *Formation and Growth of Cracking in Feed Water Pipes and RPV Nozzles, Nucl. Eng. Des.* **81**, pp. 105–119 (1984).

4. H. Watanabe, *Boiling Water Reactor Feedwater Nozzle/Sparger, Final Report*, NEDO–21821–A, General Electric Co., San Jose, CA (1980).

5. B. M. Gordon, D. E. Delwiche, and G. M. Gordon, *Service Experience of BWR Pressure Vessels*, in Performance and Evaluation of Light Water Reactor Pressure Vessels, PVP Vol.–119, American Society of Mechanical Engineers, New York, pp. 9–17 (1987).

6. E. Lenz, B. Stellwag, and N. Wieling, *The Influence of Strain–Induced Corrosion Cracking on the Crack Initiation in Low–Alloy Steels in HT–Water – A Relation Between Monotonic and Cyclic Crack Initiation Behavior*, in IAEA Specialists Meeting Corrosion and Stress Corrosion of Steel Pressure Boundary Components and Steam Turbines, VTT Symp. 43, Espoo, Finland, pp. 243–267 (1983).

7. J. Hickling and D. Blind, *Strain–Induced Corrosion Cracking of Low–Alloy Steels in LWR Systems – Case Histories and Identification of Conditions Leading to Susceptibility*, Nucl. Eng. Des. **91**, pp. 305–330 (1986).

8. R. B. Dooley, and R. S. Pathania, *Corrosion Fatigue of Water Touched Pressure Retaining Components in Power Plants*, EPRI TR–106696, Electric Power Research Institute, Palo Alto, CA (1997).

9. O. K. Chopra and W. J. Shack, *Evaluation of Effects of LWR Coolant Environments on Fatigue Life of Carbon and Low–Alloy Steels*, in Effects of the Environment on the Initiation of Crack Growth, ASTM STP 1298, W. A. Van Der Sluys, R. S. Piascik, and R. Zawierucha, eds., American Society for Testing and Materials, Philadelphia, pp. 247–266 (1997).

10. O. K. Chopra and W. J. Shack, *Effects of LWR Coolant Environments on Fatigue Design Curves of Carbon and Low–Alloy Steels*, NUREG/CR–6583, ANL–97/18 (March 1998).

11. O. K. Chopra and W. J. Shack, *Low–Cycle Fatigue of Piping and Pressure Vessel Steels in LWR Environments*, Nucl. Eng. Des. **184**, 49–76 (1998).

12. O. K. Chopra and W. J. Shack, *Overview of Fatigue Crack Initiation in Carbon and Low–Alloy Steels in Light Water Reactor Environments*, J. Pressure Vessel Technol. **121**, 49–60 (1999).

13. O. K. Chopra and J. Muscara, *Effects of Light Water Reactor Coolant Environments on Fatigue Crack Initiation in Piping and Pressure Vessel Steels*, in Proc. 8th Int. Conf. on Nuclear Engineering, 2.08 LWR Materials Issue, Paper 8300, American Society of Mechanical Engineers, New York (2000).

14. O. K. Chopra and D. J. Gavenda, *Effects of LWR Coolant Environments on Fatigue Lives of Austenitic Stainless Steels*, J. Pressure Vessel Technol. **120**, 116–121 (1998).

15. O. K. Chopra and J. L. Smith, *Estimation of Fatigue Strain–Life Curves for Austenitic Stainless Steels in Light Water Reactor Environments*, in Fatigue, Environmental Factors, and New Materials, PVP Vol. 374, H. S. Mehta, R. W. Swindeman, J. A. Todd, S. Yukawa, M. Zako, W. H. Bamford, M. Higuchi, E. Jones, H. Nickel, and S. Rahman, eds., American Society of Mechanical Engineers, New York, pp. 249–259 (1998).

16. O. K. Chopra, *Effects of LWR Coolant Environments on Fatigue Design Curves of Austenitic Stainless Steels*, NUREG/CR–5704, ANL–98/31 (1999).

17. P. D. Hobson, *The Formulation of a Crack Growth Equation for Short Cracks*, Fatigue Fract. Eng. Mater. Struct. **5**, pp. 323-327 (1982).

18. F. P. Ford, S. Ranganath, and D. Weinstein, *Environmentally Assisted Fatigue Crack Initiation in Low–Alloy Steels – A Review of the Literature and the ASME Code Requirements*, EPRI TR–102765, Electric Power Research Institute, Palo Alto, CA (1993).

19. K. J. Miller, *Initiation and Growth Rates of Short Fatigue Cracks*, Fundamentals of Deformation and Fracture, Eshelby Memorial Symposium, Cambridge University Press, Cambridge, U.K., pp. 477–500 (1985).

20. K. Tokaji, T. Ogawa, and S. Osaka, *The Growth of Microstructurally Small Fatigue Cracks in a Ferrite–Pearlite Steel*, Fatigue Fract. Engng. Mater. Struct. **11**, pp. 311–342 (1988).

21. D. J. Gavenda, P. R. Luebbers, and O. K. Chopra, *Crack Initiation and Crack Growth Behavior of Carbon and Low–Alloy Steels*, Fatigue and Fracture 1, Vol. 350, S. Rahman, K. K. Yoon, S. Bhandari, R. Warke, and J. M. Bloom, eds., American Society of Mechanical Engineers, New York, pp. 243–255 (1997).

22. K. Obrtlik, J. Polák, M. Hájek, and A. Vasek, *Short Fatigue Crack Behaviour in 316L Stainless Steel*, Intl. J. Fatigue **19**, pp. 471–475 (1997).

23. S. G. Sundara Raman, D. Argence, and A. Pineau, *High Temperature Short Fatigue Crack Behaviour in a Stainless Steel*, Fatigue Fract. Eng. Mater. Struct. **20**, pp. 1015–1031 (1997).

24. K. J. Miller, *Damage in Fatigue: A New Outlook*, International Pressure Vessels and Piping Codes and Standards: Volume 1 – Current Applications, PVP Vol. 313–1, K. R. Rao and Y. Asada, eds., American Society of Mechanical Engineers, New York, pp. 191–192 (1995).

25. N. Nagata, S. Sato, and Y. Katada, *Low–Cycle Fatigue Behavior of Pressure Vessel Steels in High–Temperature Pressurized Water*, ISIJ Intl. **31** (1), 106–114 (1991).

26. F. P. Ford, *Overview of Collaborative Research into the Mechanisms of Environmentally Controlled Cracking in the Low Alloy Pressure Vessel Steel/Water System*, Proc. 2nd Int. Atomic Energy Agency Specialists' Meeting on Subcritical Crack Growth, NUREG/CP-0067, MEA-2090, Vol. 2, pp. 3-71 (1986).

27. H. Hänninen, K. Törrönen, and W. H. Cullen, *Comparison of Proposed Cyclic Crack Growth Mechanisms of Low Alloy Steels in LWR Environments*, Proc. 2nd Int. Atomic Energy Agency Specialists' Meeting on Subcritical Crack Growth, NUREG/CP-0067, MEA-2090, Vol. 2, pp. 73-97 (1986).

28. M. Higuchi and K. Iida, *Fatigue Strength Correction Factors for Carbon and Low-Alloy Steels in Oxygen-Containing High-Temperature Water*, Nucl. Eng. Des. **129**, 293-306 (1991).

29. M. Higuchi, K. Iida, and Y. Asada, *Effects of Strain Rate Change on Fatigue Life of Carbon Steel in High-Temperature Water*, in Effects of the Environment on the Initiation of Crack Growth, ASTM STP 1298, W. A. Van Der Sluys, R. S. Piascik, and R. Zawierucha, eds., American Society for Testing and Materials, Philadelphia, pp. 216-231 (1997).

30. G. Nakao, H. Kanasaki, M. Higuchi, K. Iida, and Y. Asada, *Effects of Temperature and Dissolved Oxygen Content on Fatigue Life of Carbon and Low-Alloy Steels in LWR Water Environment*, in Fatigue and Crack Growth: Environmental Effects, Modeling Studies, and Design Considerations, PVP Vol. 306, S. Yukawa, ed., American Society of Mechanical Engineers, New York, pp. 123-128 (1995).

31. M. Higuchi, presented at Working Group Meeting on S-N Data Analysis, the Pressure Vessel Research Council, Milwaukee, WI (June 1995).

32. A. Hirano, M. Yamamoto, K. Sakaguchi, K. Iida, and T. Shoji, *Effects of Water Flow Rate on Fatigue Life of Carbon Steel in High Temperature Pure Water Environment*, in Assessment Methodologies for Predicting Failure: Service Experience and Environmental Considerations, PVP Vol. 410-2, R. Mohan, ed., American Society of Mechanical Engineers, New York, pp. 13-18 (2000).

33. E. Lenz, N. Wieling, and H. Muenster, *Influence of Variation of Flow Rates and Temperature on the Cyclic Crack Growth Rate under BWR Conditions*, in Environmental Degradation of Materials in Nuclear Power Systems - Water Reactors, The Metallurgical Society, Warrendale, PA (1988).

34. R. A. Smith, Y. Liu, and L. Garbowski, *Short Fatigue Crack Growth Behavior in Waspaloy at Room and Elevated Temperature*, Fatigue Fract. Engng. Mater. Struct. **19**, pp. 1505-1514 (1996).

35. K. Hussain, A. Tauqir, S. M. Hashmi, and A. Q. Khan, *Short Fatigue Crack Growth Behavior in Ferrite-Bainitic Steel*, Metall. Trans. A **25A**, pp. 2421-2425 (1994).

36. K. Tokaji and T. Ogawa, *The Growth Behavior of Microstructurally Small Fatigue Cracks in Metals*, Short Fatigue Cracks, ESIS 13, Mechanical Engineering Pub., London, pp. 85-99 (1992).

37. K. Tokaji, T. Ogawa, and Y. Harada, *The Growth of Small Fatigue Cracks in a Low Carbon Steel; The Effect of Microstructure and Limitation of Linear Elastic Fracture Mechanics*, Fatigue Fract. Eng. Mater. Struct. **9**, pp. 205-217 (1986).

38. K. Tokaji, T. Ogawa, Y. Harada, and Z. Ando, *Limitation of Linear Elastic Fracture Mechanics in Respect of Small Fatigue Cracks and Microstructure*, Fatigue Fract. Eng. Mater. Struct. **9**, pp. 1-14 (1986).

39. C. M. Suh, J. J. Lee, and Y. G. Kang, *Fatigue Microcracks in Type 304 Stainless Steel at Elevated Temperature*, Fatigue Fract. Eng. Mater. Struct. **13**, pp. 487-496 (1990).

40. C. M. Suh, R. Yuuki, and H. Kitagawa, *Fatigue Microcracks in a Low Carbon Steel*, Fatigue Fract. Eng. Mater. Struct. **8**, pp. 193-203 (1985).

41. E. R. de los Rios, A. Navarro, and K. Hussain, *Microstructural Variations in Short Fatigue Crack Propagation of a C-Mn Steel*, Short Fatigue Cracks, ESIS 13, Mechanical Engineering Pub., London, pp. 115-132 (1992).

42. E. R. de los Rios., X. D. Wu, and K. J. Miller, *A Micro-Mechanics Model of Corrosion-Fatigue Crack Growth in Steels*, Fatigue Fract. Eng. Mater. Struct. **19**, pp. 1383-1400 (1996).

43. J. Lankford, *Initiation and Early Growth of Fatigue Cracks in High Strength Steels*, Eng. Fract. Mech. **9**, pp. 617-624 (1977).

44. J. Lankford, *The Growth of Small Fatigue Cracks in 7075-T6 Aluminum*, Fatigue Fract. Eng. Mater. Struct. **5**, pp. 233-248 (1982).

45. J. Lankford, *The Influence of Microstructure on the Growth of Small Fatigue Cracks*, Fatigue Fract. Eng. Mater. Struct. **8**, pp. 161-175 (1985).

46. H. Kitagawa and S. Takahashi, *Applicability of Fracture Mechanics to Very Small Cracks of the Cracks in the Early Stage*, in Proc. 2nd Int. Conf. on Mechanical Behavior of Materials, ASM, pp. 627-631 (1976).

47. D. Taylor and J. F. Knott, *Fatigue Crack Propagation Behavior of Short Cracks; The Effect of Microstructure*, Fatigue Fract. Eng. Mater. Struct. **4**, pp. 147-155 (1981).

48. K. S. Ravichandran, *Effects of Crack Aspect Ratio on the Behavior of Small Surface Cracks in Fatigue; Part II. Experiments on a Titanium (Ti-8Al) Alloy*, Metall. Trans. A **28A**, pp. 157-167 (1997).

49. N. E. Dowling, *Crack Growth During Low-Cycle Fatigue of Smooth Axial Specimens*, ASTM STP 637, American Society for Testing and Materials, Philadelphia, pp. 97-121 (1977).

50. M. W. Brown, *Interface Between Short, Long and Non-Propagating Cracks*, Mechanical Engineering Pub., London, pp. 423-439 (1986).

51. E. P. Carbonell and M. W. Brown, *A Study of Short Crack Growth in Torsional Low-Cycle Fatigue for a Medium Carbon Steel*, Fatigue Fract. Eng. Mater. Struct. **9**, pp. 15-33 (1986).

52. F. P. Ford and P. L. Andresen, *Corrosion in Nuclear Systems: Environmentally Assisted Cracking in Light Water Reactors*, Marcel Dekker Inc., pp. 501-546 (1995).

53. F. P. Ford, *Quantitative Prediction of Environmentally Assisted Cracking*, Corrosion **52**, pp. 375-395 (1996).

54. T. P. O'Donnell W. J. and O'Donnell, *Stress Intensity Values in Conventional S-N Fatigue Specimens*, in International Pressure Vessels and Piping Codes and Standards, PVP 313, American Society of Mechanical Engineers, New York, pp. 195-197 (1995).

55. V. Pasupathi and R. W. Klingensmith, *Investigation of Stainless Steel Clad Fuel Rod Failures and Fuel Performance in the Connecticut Yankee Reactor*, EPRI NP-2119, 1981, Electric Power Research Institute, Palo Alto, CA (1981).

56. A. J. Jacobs, G. P. Wozadlo, K. Nakata, T. Yoshida, and I. Masaoka, *Radiation Effects on the Stress Corrosion and Other Selected Properties of Type-304 and Type-316 Stainless Steels*, in Proc. 3rd Int. Symp. on Environmental Degradation of Materials in Nuclear Power Systems – Water Reactors, G. J. Theus and J. R. Weeks, eds., The Metallurgical Society, Warrendale, PA, pp. 673-680 (1988).

57. M. P. Manahan, R. Kohli, J. Santucci, and P. Sipushi, *A Phenomenological Investigation of In-Reactor Cracking of Type 304 Stainless Steel Control Rod Cladding*, Nucl. Eng. Des. **113**, pp. 297-321 (1989).

58. R. Katsura, M. Kodama, and S. Nishimura, *DL-EPR Study of Neutron Irradiation in Type 304 Stainless Steel*, Corrosion **48**, pp. 384-390 (1992).

59. S. M. Bruemmer, L. A. Charlot, and E. P. Simpson, *Irradiation-Induced Chromium Depletion and Its Influence on Intergranular Stress Corrosion Cracking of Stainless Steels*, in Proc. 5th Int. Symp. on Environmental Degradation of Materials in Nuclear Power Systems – Water Reactors, D. Cubicciotti, E. P. Simonen, and R. Gold, eds., American Nuclear Society, La Grange Park, IL, pp. 821-826 (1992).

60. A. J. Jacobs, G. E. C. Bell, C. M. Shepherd, and G. P. Wozadlo, *High-Temperature Solution Annealing as an IASCC Mitigating Technique*, in Proc. 5th Int. Symp. on Environmental Degradation of Materials in Nuclear Power Systems – Water Reactors, D. Cubicciotti, E. P. Simonen, and R. Gold, eds., American Nuclear Society, La Grange Park, IL, pp. 917-934 (1992).

61. M. E. Indig, J. L. Nelson, and G. P. Wozadlo, *Investigation of Protection Potential against IASCC*, in Proc. 5th Int. Symp. on Environmental Degradation of Materials in Nuclear Power Systems – Water Reactors, D. Cubicciotti, E. P. Simonen, and R. Gold, eds., American Nuclear Society, La Grange Park, IL, pp. 941-947 (1992).

62. M. Kodama, S. Nishimura, J. Morisawa, S. Shima, S. Suzuki, and M. Yamamoto, *Effects of Fluence and Dissolved Oxygen on IASCC in Austenitic Stainless Steels*, in Proc. 5th Int. Symp. on Environmental Degradation of Materials in Nuclear Power Systems – Water Reactors, D. Cubicciotti, E. P. Simonen, and R. Gold, eds., American Nuclear Society, La Grange Park, IL, pp. 948-954 (1992).

63. H. M. Chung, W. E. Ruther, J. E. Sanecki, A. G. Hins, and T. F. Kassner, *Stress Corrosion Cracking Susceptibility of Irradiated Type 304 Stainless Steels*, in Effects of Radiation on Materials: 16th Int. Symp., ASTM STP 1175, A. S. Kumar, D. S. Gelles, R. K. Nanstad, and T. A. Little, eds., American Society for Testing and Materials, Philadelphia, pp. 851-869 (1993).

64. M. Kodama, K. Fukuya, and H. Kayano, *The Relationship of Grain Boundary Composition in Irradiated Type 304 SS to Neutron Fluence and IASCC*, in Effects of Radiation on Materials: 16th Int. Symp., ASTM STP 1175, A. S. Kumar, D. S. Gelles, R. K. Nanstad, and T. A. Little, eds., American Society for Testing and Materials, Philadelphia, pp. 889-901 (1993).

65. F. Garzarolli, D. Alter, P. Dewes, and J. L. Nelson, *Deformability of Austenitic Stainless Steels and Ni-Base Alloys in the Core of a Boiling and Pressurized Water Reactor*, in Proc. 3rd Int. Symp. on Environmental Degradation of Materials in Nuclear Power Systems - Water Reactors, G. J. Theus and J. R. Weeks, eds., The Metallurgical Society, Warrendale, PA, pp. 657-664 (1993).

66. A. J. Jacobs, *Influence of Impurities and Alloying Elements on IASCC in Neutron Irradiated Austenitic Stainless Steels*, in Effects of Radiation on Materials: 16th Int. Symp., ASTM STP 1175, A. S. Kumar, D. S. Gelles, R. K. Nanstad, and T. A. Little, eds., American Society for Testing and Materials, Philadelphia, pp. 902-918 (1993).

67. R. D. Carter, D. L. Damcott, M. Atzmon, G. S. Was, S. M. Bruemmer, and E. A. Kenik, *Capabilities and Limitations of Analytical Methods Used to Measure Radiation Induced Grain Boundary Segregation*, in Proc. 6th Int. Symp. on Environmental Degradation of Materials in Nuclear Power Systems - Water Reactors, R. E. Gold and E. P. Simonen, eds., The Minerals, Metals, and Materials Society, Warrendale, PA, pp. 501-509 (1993).

68. H. M. Chung, W. E. Ruther, J. E. Sanecki, and T. F. Kassner, *Grain-Boundary Microchemistry and Intergranular Cracking of Irradiated Austenitic Stainless Steels*, in Proc. 6th Int. Symp. on Environmental Degradation of Materials in Nuclear Power Systems - Water Reactors, R. E. Gold and E. P. Simonen, eds., The Minerals, Metals, and Materials Society, Warrendale, PA, pp. 511-519 (1993).

69. S. M. Bruemmer, J. I. Cole, J. L. Brimhall, R. D. Carter, and G. S. Was, *Radiation Hardening Effects on Localized Deformation and Stress Corrosion Cracking of Stainless Steels*, in Proc. 6th Int. Symp. on Environmental Degradation of Materials in Nuclear Power Systems - Water Reactors, R. E. Gold and E. P. Simonen, eds., The Minerals, Metals, and Materials Society, Warrendale, PA, pp. 537-545 (1993).

70. K. Fukuya, S. Shima, K. Nakata, S. Kasahara, A. J. Jacobs, G. P. Wozadlo, S. Suzuki, and M. Kitamura, *Mechanical Properties and IASCC Susceptibility in Irradiated Stainless Steels*, in Proc. 6th Int. Symp. on Environmental Degradation of Materials in Nuclear Power Systems - Water Reactors, R. E. Gold and E. P. Simonen, eds., The Minerals, Metals, and Materials Society, Warrendale, PA, pp. 564-572 (1993).

71. J. L. Cookson, D. L. Damcott, G. W. Was, and P. L. Andresen, *The Role of Microchemical and Microstructural Effects in the IASCC of High-Purity Austenitic Stainless Steels*, in Proc. 6th Int. Symp. on Environmental Degradation of Materials in Nuclear Power Systems - Water Reactors, R. E. Gold and E. P. Simonen, eds., The Minerals, Metals, and Materials Society, Warrendale, PA, pp. 573-580 (1993).

72. K. Kodama, R. Katsura, J. Morisawa, S. Nishimura, S. Suzuki, K. Asano, K. Fukuya, and K. Nakata, *IASCC Susceptibility of Austenitic Stainless Steels Irradiated to High Neutron Fluence*, Proc. 6th Int. Symp. on Environmental Degradation of Materials in Nuclear Power Systems - Water Reactors, R. E. Gold and E. P. Simonen, eds., The Minerals, Metals, and Materials Society, Warrendale, PA, pp. 583-588 (1993).

73. A. J. Jacobs, G. P. Wozadlo, K. Nakata, S. Kasahara, T. Okada, S. Kawano, and S. Suzuki, *The Correlation of Grain Boundary Composition in Irradiated Stainless Steel with IASCC Resistance*, in Proc. 6th Int. Symp. on Environmental Degradation of Materials in Nuclear Power Systems - Water Reactors, R. E. Gold and E. P. Simonen, eds., The Minerals, Metals, and Materials Society, Warrendale, PA, pp. 597-606 (1993).

74. F. Garzarolli, P. Dewes, R. Hahn, and J. L. Nelson, *Deformability of High-Purity Stainless Steels and Ni-Base Alloys in the Core of a PWR*, in Proc. 6th Int. Symp. on Environmental Degradation of Materials in Nuclear Power Systems - Water Reactors, R. E. Gold and E. P. Simonen, eds., The Minerals, Metals, and Materials Society, Warrendale, PA, pp. 607-613 (1993).

75. S. Kasahara, K. Nakata, K. Fukuya, S. Shima, A. J. Jacobs, G. P. Wozadlo, and S. Suzuki, *The Effects of Minor Elements on IASCC Susceptibility in Austenitic Stainless Steels Irradiated with Neutrons*, in Proc. 6th Int. Symp. on Environmental Degradation of Materials in Nuclear Power Systems - Water Reactors, R. E. Gold and E. P. Simonen, eds., The Minerals, Metals, and Materials Society, Warrendale, PA, pp. 615-623 (1993).

76. M. Kodama, J. Morisawa, S. Nishimura, K. Asano, S. Shima, and K. Nakata, *Stress Corrosion Cracking and Intergranular Corrosion of Austenitic Stainless Steels Irradiated at 323 K*, J. Nucl. Mater. **1509**, pp. 212–215 (1994).

77. T. Tsukada and Y. Miwa, *Stress Corrosion Cracking of Neutron Irradiated Stainless Steels*, in Proc. 7th Int. Symp. on Environmental Degradation of Materials in Nuclear Power Systems - Water Reactors, NACE International, Houston, pp. 1009–1018 (1995).

78. A. Jenssen and L. G. Ljungberg, *Irradiation Assisted Stress Corrosion Cracking - Postirradiation CERT Tests of Stainless Steels in a BWR Test Loop*, in Proc. 7th Int. Symp. on Environmental Degradation of Materials in Nuclear Power Systems - Water Reactors, NACE International, Houston, pp. 1043–1052 (1995).

79. F. Garzarolli, P. Dewes, R. Hahn, and J. L. Nelson, *In-Reactor Testing of IASCC Resistant Stainless Steels*, in Proc. 7th Int. Symp. on Environmental Degradation of Materials in Nuclear Power Systems - Water Reactors, NACE International, Houston, pp. 1055–1065 (1995).

80. H. M. Chung, W. E. Ruther, J. E. Sanecki, A. G. Hins, and T. F. Kassner, *Effects of Water Chemistry on Intergranular Cracking of Irradiated Austenitic Stainless Steels*, in Proc. 7th Int. Symp. on Environmental Degradation of Materials in Nuclear Power Systems - Water Reactors, NACE International, Houston, pp. 1133-1143 (1995).

81. K. Hide, T. Onchi, M. Mayazumi, K. Dohi, and Y. Futamura, *Intergranular Cracking of Irradiated Thermally Sensitized Type 304 Stainless Steel in High-Temperature Water and Inert Gas*, Corrosion **51**, pp. 757-766 (1995).

82. H. M. Chung, W. E. Ruther, J. E. Sanecki, A. G. Hins, N. J. Zaluzec, and T. F. Kassner, *Irradiation-Assisted Stress Corrosion Cracking of Austenitic Stainless Steels: Recent Progress and New Approaches*, J. Nucl. Mater., **239**, 61 (1996).

83. H. Kanasaki, T. Okubo, I. Satoh, M. Koyama, T. R. Mager, and R. G. Lott, *Fatigue and Stress Corrosion Cracking Behaviors of Irradiated Stainless Steels in PWR Primary Water*, in Proc. 5th Int. Conf. on Nuclear Engineering, Nice, France (May 26-30, 1997).

84. T. Tsukada, Y. Miwa, H. Nakajima, and T. Kondo, *Effects of Minor Elements on IASCC of Type 316 Model Stainless Steels*, in Proc. 8th Int. Symp. on Environmental Degradation of Materials in Nuclear Power Systems - Water Reactors, Aug. 10-14, 1997, Amelia Island, FL, S. M. Bruemmer, ed., American Nuclear Society, La Grange Park, IL, pp. 795-802 (1997).

85. T. Yonezawa, K. Fujimoto, H. Kanasaki, T. Iwamura, S. Nakada, K. Ajiki, and K. Sakai, *SCC Susceptibility of Irradiated Austenitic Stainless Steels for PWR*, in Proc. 8th Int. Symp. on Environmental Degradation of Materials in Nuclear Power Systems - Water Reactors, Aug. 10-14, 1997, Amelia Island, FL, S. M. Bruemmer, ed., American Nuclear Society, La Grange Park, IL, pp. 823-830 (1997).

86. M. Kodama, S. Nishimura, Y. Tanaka, S. Suzuki, K. Fukuya, S. Shima, K. Nakata, and T. Kato, *Mechanical Properties of Various Kinds of Irradiated Austenitic Stainless Steels*, in Proc. 8th Int. Symp. on Environmental Degradation of Materials in Nuclear Power Systems - Water Reactors, Aug. 10-14, 1997, Amelia Island, FL, S. M. Bruemmer, ed., American Nuclear Society, La Grange Park, IL, pp. 831-838 (1997).

87. H. M. Chung, J.-H. Park, W. E. Ruther, J. E. Sanecki, R. V. Strain, and N. J. Zaluzec, *Fabrication-Related Impurity Contamination and Stress Corrosion Cracking of Austenitic Stainless Steel Core-Internal Components*, in Proc. 8th Int. Symp. on Environmental Degradation of Materials in Nuclear Power Systems - Water Reactors, Aug. 10-14, 1997, Amelia Island, FL, S. M. Bruemmer, ed., American Nuclear Society, La Grange Park, IL, pp. 846-856 (1997).

88. J. M. Cookson, G. S. Was, and P. L. Andresen, *Oxide-Induced Initiation of Stress Corrosion Cracking in Irradiated Stainless Steels*, Corrosion **54**, 299 (1998).

89. H. M. Chung, J. E. Sanecki, and F. A. Garner, *Radiation-Induced Instability of Mns Precipitates and Its Possible Consequences on Irradiation-Induced Stress Corrosion Cracking of Austenitic Stainless Steels*, Effects of Radiation on Materials: 18th Int. Symp., ASTM STP 1325, eds. R. K. Nanstad, M. L. Hamilton, A. S. Kumar, and F. A. Garner, American Society for Testing and Material, pp. 647-658 (1999).

90. H. M. Chung, W. E. Ruther, J.-H. Park, J. E. Sanecki, and N. J. Zaluzec, *Stress Corrosion Cracking of Austenitic Stainless Steel Core Internal Weld*, Paper #443, Corrosion '99, (Feb. 1999).

91. H. M. Chung, J.-H. Park, J. E. Sanecki, N. J. Zaluzec, T. T. Yang, and M. S. Yu, *Cracking Mechanism of Type 304L Stainless Steel Core Shroud Welds*, Proc. 9th Int. Conf. on Environmental Degradation of Materials in Nuclear Power Systems - Water Reactors, eds. S. Bruemmer, P. Ford, and G. Was, The Minerals, Metals, and Materials Society, Warrendale, PA, pp. 973-984 (1999).

92. H. M. Chung, W. E. Ruther, R. V. Strain, W. J. Shack, and T. M. Karlsen, *Irradiation-Assisted Stress Corrosion Cracking of Model Austenitic Stainless Steels*, Proc. 9th Int. Conf. on Environmental Degradation of Materials in Nuclear Power Systems - Water Reactors, eds. S. Bruemmer, P. Ford, and G. Was, The Minerals, Metals, and Materials Society, Warrendale, PA, pp. 931-939 (1999).

93. H. M. Chung, W. E. Ruther, R. V. Strain, and W. J. Shack, *Stress Corrosion Cracking of Type 304 Stainless Steel Irradiated to Very High Dose*, Paper #204, Corrosion 2000, Orlando, FL, March 26-31 (2000).

94. H. M. Chung, W. E. Ruther, and R. V. Strain, *Slow Strain Rate Tensile Testing of Model Austenitic Stainless Steels Irradiated in the Halden Reactor*, in Environmentally Assisted Cracking in Light Water Reactors, Semiannual Report, July-December 1998, NUREG/CR-4667, Vol. 27, ANL-99/11, pp. 28-38 (Oct. 1999).

95. H. M. Chung, W. E. Ruther, and R. V. Strain, *Slow Strain Rate Tensile Test of Model Austenitic Stainless Steels Irradiated in the Halden Reactor*, in Environmentally Assisted Cracking in Light Water Reactors, Semiannual Report, January-June 1999, NUREG/CR-4667, Vol. 28, ANL-00/7, pp. 14-17 (July 2000).

96. H. M. Chung, W. E. Ruther, and R. V. Strain, *Slow Strain Rate Tensile Test of Model Austenitic Stainless Steels Irradiated in the Halden Reactor*, in Environmentally Assisted Cracking in Light Water Reactors, Semiannual Report, July 1999-December 1999, NUREG/CR-4667, Vol. 29, ANL-00/23, pp. 18-29 (Nov. 2000).

97. *Sulfide Inclusions in Steel*, Proc. Int. Symp., Nov. 7-8, 1974, Port Chester, New York, J. J. de Barbadillo and E. Snape, eds., American Society of Metals (1975).

98. P. L. Andresen and C. L. Briant, *Role of S, P, and N Segregation on Intergranular Environmental Cracking of Stainless Steels in High Temperature Water*, in Proc. 3rd Int. Symp. on Environmental Degradation of Materials in Nuclear Power Systems – Water Reactors, G. J. Theus and J. R. Weeks, eds., The Metallurgical Society, Warrendale, PA, pp. 371-381 (1988).

99. O. K. Chopra, E. E. Gruber, and W. J. Shack, *Fracture Toughness Characterization of Type 304 Stainless Steel Irradiated in the Halden Reactor*, in Proc. 8th Int. Conf. on Nuclear Engineering, 2.02 Aging and Modeling of Component Aging Including Corrosion of Metals and Welds, Paper 8301, American Society of Mechanical Engineers, New York (2000).

100. E. E. Gruber and O. K. Chopra, *Fracture Toughness J-R Test of Austenitic Stainless Steels Irradiated in the Halden Reactor*, in Environmentally Assisted Cracking in Light Water Reactors, Semiannual Report, July–December 1999, NUREG/CR-4667, Vol. 29, ANL-00/23, pp. 30–38 (Nov. 2000).

101. T. H. Hughes and E. E. Gruber, *Development of Hot–Cell J–R Test Facility*, in Environmentally Assisted Cracking in Light Water Reactors Semiannual Report July 1996–December 1996, NUREG/CR–4667, Vol. 23, ANL–97/10, pp. 42–52 (1997).

102. E. E. Gruber and O. K. Chopra, *Fracture Toughness J-R Test of Austenitic Stainless Steels Irradiated in Halden Reactor*, in Environmentally Assisted Cracking in Light Water Reactors Semiannual Report July 1998–December 1998, NUREG/CR–4667, Vol. 27, ANL–99/11, pp. 39–45 (Oct. 1999).

103. W. E. Ruther, W. K. Soppet, and T. F. Kassner, *Corrosion Fatigue of Alloys 600 and 690 in simulated LWR Environments*, NUREG/CR–6383, ANL–95/37 (April 1996).

104. W. E. Ruther, W. K. Soppet, and T. F. Kassner, *Environmentally Assisted Cracking of Alloys 600 and 690 in Simulated LWR Water*, in Environmentally Assisted Cracking in Light Water Reactors, Semiannual Report, July 1997–December 1997, NUREG/CR–4667 Vol. 25, ANL–98/18, pp. 42–75 (Sept. 1998).

105. W. E. Ruther, W. K. Soppet, T. F. Kassner, and W. J. Shack, *Environmentally Assisted Cracking of Alloys 600 and 690 in Simulated LWR Water*, in Environmentally Assisted Cracking in Light Water Reactors, Semiannual Report, January 1998–July 1998, NUREG/CR–4667 Vol. 26, ANL–98/18, pp. 25–32 (March 1999).

106. W. E. Ruther, W. K. Soppet, T. F. Kassner, and W. J. Shack, *Environmentally Assisted Cracking of Alloys 600 and 690 in Simulated LWR Water*, in Environmentally Assisted Cracking in Light Water Reactors, Semiannual Report, July 1998–December 1998, NUREG/CR–4667 Vol. 27, ANL–99/11, pp. 45-54 (Oct. 1999).

107. W. K. Soppet, O. K. Chopra, and W. J. Shack, *Environmentally Assisted Cracking of Alloys 600 and 690 in Simulated LWR Water*, in Environmentally Assisted Cracking in Light Water Reactors, Semiannual Report, July 1999–December 1999, NUREG/CR–4667 Vol. 29, ANL–00/23, pp. 39-45 (Nov. 2000).

108. L. A. James and D. P. Jones, *Fatigue Crack Growth Rates for Austenitic Stainless Steel in Air*, in Predictive Capabilities in Environmentally Assisted Cracking, PVP Vol. 99, The American Society of Mechanical Engineers, New York, pp. 363–414 (1985).

109. R. G. Ballinger, R. M. Latanision, W. C. Moshier, and R. M. Pelloux, *The Effects of Heat Treatment and Environment on Corrosion Fatigue, Volume 2: Alloy 600*, EPRI TR-102436 (May 1993).

110. C. Amzallag, G. Baudry, and J. L. Bernard, *Effects of PWR Environment on the Fatigue Crack Growth of Different Stainless Steels and Inconel Type Alloy*, Proc. IAEA-Specialists Meeting on Subcritical Crack Growth, NUREG/CP–0044, Vol. 1, pp. 263–294 (1983).

111. L. A. James and W. J. Mills, *Fatigue–Crack Propagation Behavior of Wrought Alloy 600 and Weld–Deposited EN82H in an Elevated Temperature Aqueous Environment*, in Service Experience, Structural Integrity, Severe Accident, and Erosion in Nuclear and Fossil Plants, PVP Vol. 303, The American Society of Mechanical Engineers, pp. 21–36 (1995).

112. C. K. Sheeks, W. C. Moshier, R. G. Ballinger, R. M. Latanision, and R. M. N. Pelloux, *Fatigue Crack Growth of Alloys X-750 and 600 In Simulated PWR and BWR Environments*, in Intl. Symp. on Environmental Degradation of Materials in Nuclear Power Systems-Water Reactors, NACE, pp. 701–726 (1984).

113. N. Konda, K. Toyama, K. Yamanaka, and K. Tokimasa, *Environmental Effects on the Crack Growth Properties of Alloy 600*, Sumitomo Metal Industries, Ltd. R & D Division, 1-3 Fusocho, Amagasaki 660, Japan (Oct. 1991).

114. H. Nagano, K. Tokimasa, K. Tanaka, and H. Tsuge, *Evaluation of SCC Resistance of Alloy 600 in High Temperature Pressurized Water Environments by the High Stress Ratio Cyclic Crack Growth Tests*, ISIJ Intl. (1988).

115. P. L. Andresen, *Fracture Mechanics Data and Monitoring of Environmental Cracking of Nickel–Base Alloys in High–Temperature Water*, Corrosion, **47**, pp. 917–938 (1991).

116. G. Nakao, H. Yamasaki, and S. Kimura, *Fatigue Crack Growth Behavior of Inconel 600 Alloys in Oxygenated High Temperature Pure Water*, cited in Ref. 28 (1985).

117. H. D. Solomon, *Summary of In 600 Metallurgical Studies*, Report SRD–81–034, GE CRD, Schenectady, NY (April 1981).

118. R. Magdowski, F. Vaillant, C. Amzallag, and M. O. Speidel, *Stress Corrosion Crack Growth Rates of Alloy 600 in Simulated PWR Coolant*, in Proc. of the 8th Intl. Symp. on Environmental Degradation of Materials in Nuclear Power Systems-Water Reactors, S. M. Bruemmer, ed., American Nuclear Society, La Grange Park, IL, pp. 333-338 (1997).

119. T. Cassagne, D. Caron, J. Daret, and Y. Lefevre, *Stress Corrosion Crack Growth Rate Measurements in Alloys 600 and 182 in Primary Loops Under Constant Load*, in Proc. of the Ninth Intl. Symp. on Environmental Degradation of Materials in Nuclear Power Systems-Water Reactors, F. P. Ford, S. M. Bruemmer, and G. S. Was, eds., The Minerals, Metals, and Materials Society, Warrendale, PA, pp. 217-224 (1999).

120. J. Lagerstrom, U. Ehrnsten, T. Saario, and H. Hanninen, *Model for Environmentally Asisted Cracking of Alloy 600 in PWR Primary Water*, in Proc. of the 8th Intl. Symp. on Environmental Degradation of Materials in Nuclear Power Systems-Water Reactors, S. M. Bruemmer, ed., American Nuclear Society, La Grange Park, IL, pp. 349–356 (1997).

121. F. P. Ford, *Quantitative Prediction of Environmentally Assisted Cracking*, Corrosion, **52**, pp. 375–395 (1997).

122. F. P. Ford, D. F. Taylor, P. L. Andresen, and R. Ballinger, *Corrosion-Assisted Cracking of Stainless and Low-alloy Steels*, EPRI NP-5064, Electric Power Research Institute, Palo Alto, CA (Feb. 1987).

123. T. Shoji, *Quantitative Prediction of Environmentally Assisted Cracking Based on Crack Tip Strain Rate*, Proc. Conf. on Predictive Capabilities in Environmentally-Assisted Cracking, R. Rungta, ed., PVP Vol. 99, American Society of Mechanical Engineers, New York, pp. 127-142 (1985).

Appendix:
Correlation for Calculating Stress Range, Stress Intensity Range, and Crack Growth Rates

Cyclic Stress Range

The cyclic stress–strain response of carbon and low–alloy steels varies with steel type, temperature, and strain rate. In general, these steels exhibit initial cyclic hardening, followed by cyclic softening or a saturation stage. The CSs, with a pearlite and ferrite structure and low yield stress, show significant initial hardening. The LASs, which consist of tempered ferrite and a bainite structure, exhibit a relatively high yield stress, and show little or no initial hardening, may exhibit cyclic softening at high strain ranges. At 200–370°C, these steels exhibit dynamic strain aging, which leads to enhanced cyclic hardening, a secondary hardening stage, and negative strain rate sensitivity. Under the conditions of dynamic strain aging, cyclic stress increases with decreases in strain rate.

The cyclic stress–range–vs.–strain–range relationship is expressed by the modified Ramberg–Osgood relationship given by

$$\Delta\varepsilon = (\Delta\sigma/E) + (\Delta\sigma/A_3)^{n_3}, \tag{A1}$$

where E is Young's modulus, constant A_3 and exponent n_3 are determined from the experimental data, and cyclic stress range corresponds to the value at half-life. At room temperature, the relationship of cyclic stress range $\Delta\sigma$ (MPa) to strain range $\Delta\varepsilon$ (%) for CSs may be represented by

$$\Delta\varepsilon = (\Delta\sigma/2010) + (\Delta\sigma/766.1)^{(1/0.207)}, \tag{A2}$$

and for LASs, by

$$\Delta\varepsilon = (\Delta\sigma/2010) + (\Delta\sigma/847.4)^{(1/0.173)}. \tag{A3}$$

The effect of strain rate on the cyclic stress–strain curve is not considered at room temperature. At 288°C, the cyclic stress–strain curves may be represented by the correlations developed by Chopra and Shack.[A1] For CSs, the curve is given by the relationship

$$\Delta\varepsilon = (\Delta\sigma/1965) + (\Delta\sigma/Asig)^{(1/0.129)}, \tag{A4a}$$

where Asig varies with the strain rate $\dot{\varepsilon}$ (%/s) expressed as

$$Asig = 1079.7 - 50.9 \log(\dot{\varepsilon}). \tag{A4b}$$

For LASs, the curve is given by the relationship

$$\Delta\varepsilon = (\Delta\sigma/1965) + (\Delta\sigma/Bsig)^{(1/0.110)}, \tag{A5a}$$

where Bsig is expressed as

$$Bsig = 961.8 - 30.3 \log(\dot{\varepsilon}). \tag{A5b}$$

Stress Intensity Factor Range

For cylindrical fatigue specimens, the range of stress intensity factor ΔK was determined from the value of the J–integral range ΔJ, which, for a small semicircular surface crack, is given by Dowling[A2] as

$$\Delta J = 3.2\ (\Delta\sigma^2/2E)\ a + 5\ [\Delta\sigma\ \Delta\varepsilon_p/(S + 1)]\ a, \qquad \text{(A6a)}$$

where $\Delta\varepsilon_p$ is plastic strain range (%) (second term in the Ramberg Osgood relationship) and S is the reciprocal of the strain hardening exponent n in Eq. A1. The stress intensity factor range ΔK is obtained from

$$\Delta K = (E\ \Delta J)^{1/2}, \qquad \text{(A6b)}$$

where E is the elastic modulus. Equation A6a incorporates a combined surface and flaw shape correction factor F_S of 0.714, which is derived from equivalent linear elastic solutions; Eq. A6a is valid as long as the crack size is very small when compared with the specimen diameter. For conventional fatigue tests, life is defined as the number of cycles for the tensile stress to decrease 25% from the peak or steady–state value, i.e., the crack–depth–to–specimen–diameter ratio can be as high as 0.4. Therefore, the geometrical correction factor F_s for a small semicircular surface crack was modified according to the correlation developed by O'Donnell and O'Donnell:[A3]

$$F_s = 0.6911 + 1.2685\ (a/D) - 5.6638\ (a/D)^2 + 21.511\ (a/D)^3, \qquad \text{(A7)}$$

where D is specimen diameter. For conventional fatigue tests on cylindrical specimens, F_s may increase up to 1.7.

The J–integral range ΔJ is calculated from the ranges of cyclic stress and plastic strain, determined from stable hysteresis loops, i.e., at fatigue half–life. In general, ΔJ is computed only for that portion of the loading cycle during which the crack is open. For fully reversed cyclic loading, the crack opening point can be identified as the point where the curvature of the load–vs.–displacement line changed before the peak compressive load. In the present study, evidence of a crack opening point was observed for cracks that had grown relatively large, i.e., near the end of fatigue life. Therefore, as recommended by Dowling,[A2] the entire hysteresis loop was used in estimating ΔJ.

Crack Growth Rate

The fatigue CGRs da/dN of structural materials are characterized in terms of the range of applied stress intensity factor ΔK and are given in Article A–4300 of Section XI of the ASME Boiler and Pressure Vessel Code. For a stress ratio R in the range of $-2 < R < 0$, the reference fatigue CGRs da/dN (mm/cycle) of carbon and low–alloys steels exposed to air environments are given by

$$da/dN = 3.78 \times 10^{-9}\ (\Delta K)^{3.07}, \qquad \text{(A8)}$$

where $\Delta K = K_{max}$, the maximum stress intensity factor ($MPa \cdot m^{1/2}$). However, the effect of temperature is not considered in Eq. A8; Logsdon and Liaw[A4] have shown that CGRs are

generally higher at 288°C than at room temperature. The results of Logsdon and Liaw indicate that for both CSs and LASs, CGRs are ≈22% higher at 288°C than at room temperature.

Section XI of the ASME Code also includes CGR curves for these steels exposed to LWR environments. The growth rates are represented by two curves for low and high values of ΔK. However, the curves do not consider the effects of loading rate. Recent experimental results have shown the importance of key variables of material, environment, and loading rate on CGRs in LWR environments. Fatigue CGR correlations have been developed to explicitly consider the effects of loading rate, stress ratio R, ΔK, and sulfur content in the steel.[A5] The new correlations, shown in Fig. A1, are divided into two categories: (a) for materials not susceptible to environmental effects, e.g., when sulfur content in the steel is low, CGRs are a factor of 2.8 higher than those in air; and (b) for materials susceptible to environmental effects, e.g., when sulfur content in the steel is high, CGRs are defined in terms of rise time θ, stress ratio R, and ΔK.

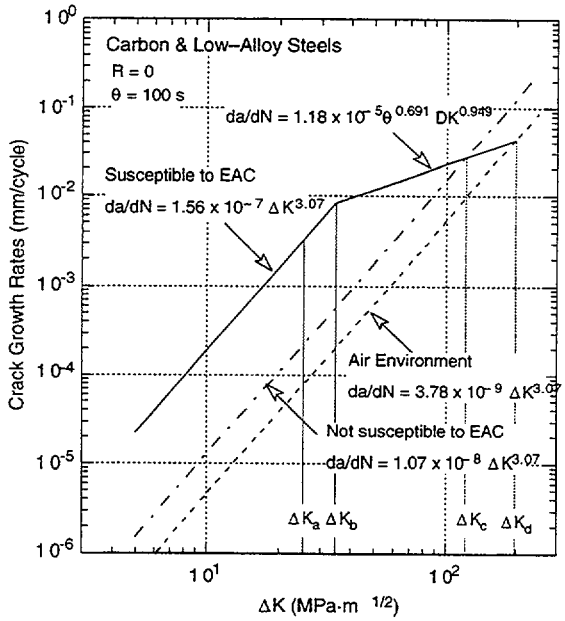

Figure A1.
Proposed reference fatigue crack growth rate curves for carbon and low–alloy steels in LWR environments for a rise time of 100 s and R = –1

The correlations in Fig. A1 correspond to a rise time of 100 s and K_{min} <0, e.g., fully reversed cyclic loading; R is set to zero. The various threshold values of ΔK (MPa·m$^{1/2}$) are given by

$$\Delta K_a = 14.156\ \theta^{0.125}, \quad \text{(A9a)}$$

$$\Delta K_b = 7.691\ \theta^{0.326}, \quad \text{(A9b)}$$

$$\Delta K_c = 27.186\ \theta^{0.326}, \quad \text{(A9c)}$$

$$\Delta K_d = 44.308\ \theta^{0.326}, \quad \text{(A9d)}$$

where rise time θ is in seconds.

References for Appendix

A1. O. K. Chopra and W. J. Shack, *Effects of LWR Coolant Environments on Fatigue Design Curves of Carbon and Low-Alloy Steels*, NUREG/CR-6583, ANL-97/18 (March 1998).

A2. N. E. Dowling, *Crack Growth During Low-Cycle Fatigue of Smooth Axial Specimens*, ASTM STP 637, American Society for Testing and Materials, Philadelphia, pp. 97-121 (1977).

A3. T. P. O'Donnell W. J. and O'Donnell, *Stress Intensity Values in Conventional S-N Fatigue Specimens*, in International Pressure Vessels and Piping Codes and Standards, PVP 313, ASME, New York, pp. 195-197 (1995).

A4 W. A. Logsdon and P. K. Liaw, *Fatigue Crack Growth Rate Properties of SA508 and SA533 Pressure Vessel Steels and Submerged Arc Weldments in Room and Elevated Temperature Air Environments*, Eng. Frac. Mech. **22**, pp. 509-526 (1985).

A5 E. D. Eason, E. E. Nelson, and J. D. Gilman, *Modeling of Fatigue Crack Growth Rate for Ferritic Steels in Light Water Reactor Environments*, Changing Priorities of Code and Standards, PVP 286, ASME, New York, pp. 131-142 (1994).

NRC FORM 335
(2–89)
NRCM 1102,
3201, 3202

U. S. NUCLEAR REGULATORY COMMISSION

BIBLIOGRAPHIC DATA SHEET

(See instructions on the reverse)

1. REPORT NUMBER
(Assigned by NRC. Add Vol., Supp., Rev., and Addendum Numbers, if any.)

NUREG/CR-4667, Vol. 30
ANL-01/08

2. TITLE AND SUBTITLE

Environmentally Assisted Cracking in Light Water Reactors.
Semiannual Report January 2000 – June 2000

3. DATE REPORT PUBLISHED

MONTH	YEAR
June	2001

4. FIN OR GRANT NUMBER

W6610

5. AUTHOR(S)

O. K. Chopra, H. M. Chung, E. E. Gruber, D. R. Perkins,
W. J. Shack, W. K. Soppet, and R. V. Strain

6. TYPE OF REPORT

Technical; Semiannual

7. PERIOD COVERED *(Inclusive Dates)*

January 2000—June 2000

8. PERFORMING ORGANIZATION – NAME AND ADDRESS *(If NRC, provide Division, Office or Region, U.S. Nuclear Regulatory Commission, and mailing address; if contractor, provide name and mailing address.)*

Argonne National Laboratory
9700 South Cass Avenue
Argonne, IL 60439

9. SPONSORING ORGANIZATION – NAME AND ADDRESS *(If NRC, type "Same as above": if contractor, provide NRC Division, Office or Region, U.S. Nuclear Regulatory Commission, and mailing address.)*

Division of Engineering Technology
Office of Nuclear Regulatory Research
U.S. Nuclear Regulatory Commission
Washington, DC 20555–0001

10. SUPPLEMENTARY NOTES

M. B. McNeil, NRC Project Manager

11. ABSTRACT (200 words or less)

This report summarizes work performed by Argonne National Laboratory on fatigue and environmentally assisted cracking (EAC) in light water reactors (LWRs) from January 2000 to June 2000. Topics that have been investigated include (a) environmental effects on fatigue S–N behavior of primary pressure boundary materials, (b) irradiation–assisted stress corrosion cracking (IASCC) of austenitic stainless steels (SSs), and (c) EAC of Alloys 600 and 690. Fatigue crack growth data and fracture mechanics analysis have been used to examine the fatigue S-N behavior of carbon and low-alloy steels in air and LWR environments. Fatigue life is considered to be composed of the growth of microstructurally small cracks and mechanically small cracks. The influence of reactor environments on the mechanism of fatigue crack initiation is discussed. Data from slow-strain-rate tensile tests and posttest fractographic analyses on several model SS alloys irradiated to $\approx 0.9 \times 10^{21}$ n·cm^{-2} (E > 1 MeV) in He at 289°C in the Halden reactor have been summarized. The results have been used to determine the influence of alloying and impurity elements on the susceptibility of these steels to IASCC. Field–cracked BWR core shroud welds have been analyzed by advance metallographic techniques to provide a better understanding of the cracking mechanism, failure behavior, and microstructural characteristics of the material. The list of test specimens shipped to the Halden Reactor for Phase–II irradiation experiments is presented. Fatigue crack growth tests were conducted on 1/4–T compact tension specimens of cast SSs in high–purity water at 289°C to establish the test procedure and conditions that will be used for performing crack growth tests on irradiated materials. The resistance of Alloys 600 and 690 to EAC in simulated LWR environments has been evaluated. The existing crack growth data for these alloys under cyclic loads have been analyzed to establish the effects of alloy chemistry, cold work, and water chemistry.

12. KEY WORDS/DESCRIPTORS *(List words or phrases that will assist researchers in locating this report.)*

Corrosion Fatigue
Crack Growth
Irradiation–Assisted Stress Corrosion Cracking
Radiation–Induced Segregation
Stress Corrosion Cracking
Carbon and Low–Alloy Steels
Types 304, 304L, 316, and 316NG Stainless Steel
Alloys 600 and 690

13. AVAILABILITY STATEMENT

Unlimited

14. SECURITY CLASSIFICATION

(This Page)
Unclassified

(This Report)
Unclassified

15. NUMBER OF PAGES

16. PRICE

NRC FORM 335 (2–89)

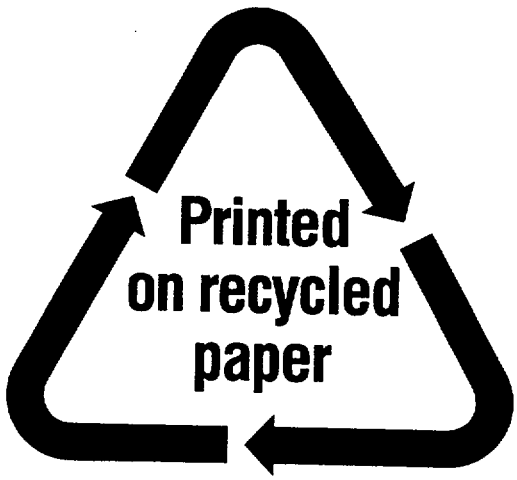

Federal Recycling Program

NUREG/CR-4667, Vol. 30 has been reproduced from the best available copy.

UNITED STATES
NUCLEAR REGULATORY COMMISSION
WASHINGTON, DC 20555-0001

OFFICIAL BUSINESS
PENALTY FOR PRIVATE USE, $300